DISSERTATIONES
TECHNOLOGIAE
UNIVERSITATIS
TARTUENSIS
**96**

YAUHENI SAROKIN

# Passive and active liquid mediation in natural and synthetic morphing systems

DISSERTATIONES TECHNOLOGIAE UNIVERSITATIS TARTUENSIS
**96**

DISSERTATIONES TECHNOLOGIAE UNIVERSITATIS TARTUENSIS
**96**

**YAUHENI SAROKIN**

# Passive and active liquid mediation in natural and synthetic morphing systems

UNIVERSITY OF TARTU
Press
1632

Institute of Technology, Faculty of Science and Technology, University of Tartu, Estonia

The dissertation was accepted for the commencement of the degree of Doctor of Philosophy in Engineering of Physical Engineering on 29.10.2025, by the Joint Council of the Doctoral Program of Engineering and Technology of the University of Tartu.

Supervisors: Indrek Must, PhD
Associate Professor of Soft Robotics
Institute of Technology, University of Tartu, Estonia

Alvo Aabloo, PhD
Professor of Polymeric Materials
Institute of Technology, University of Tartu, Estonia

Reviewer: Olev Märtens, PhD
Senior Research Fellow
Thomas Johann Seebeck Department of Electronics,
Tallinn University of Technology, Estonia

Opponent: Veikko Tapani Sariola, PhD
Professor, Bio-MEMS
Faculty of Medicine and Health Technology
Tampere University, Finland

Commencement: Auditorium 121, Nooruse 1, Tartu, Estonia,
at 13.15 on November 21th, 2025

Publication of this thesis is granted by the Institute of Technology, Faculty of Science and Technology, University of Tartu.

ISSN 2228-0855 (print)
ISBN 978-9908-57-054-9 (print)
ISSN 2806-2620 (pdf)
ISBN 978-9908-57-055-6 (pdf)



University of Tartu Press
www.tyk.ee

# CONTENTS

# ABSTRACT

Plants adapt with remarkable efficiency by shifting water inside their tissues: capillary uptake, turgor changes, and hygroscopic swelling let them stiffen, soften, bend, or coil without a central controller. Inspired by this ability, the present thesis asks how liquids can become active, information-bearing parts of an embodied-intelligence system and how the rules observed in biology can be transferred to synthetic liquid-mediated systems. Four complementary measurement techniques have been developed to track free liquid redistribution and gauge free-to-bound liquid conversion kinetics. These techniques include: fibre-optic reflectometry, which tracks free-water fronts in anisotropic capillaries with millisecond resolution, and micro-impedance spectroscopy, which converts local ionic conductance into pore-fill ratio inside porous matrices. Additionally, hygro-actuation extent detection and controlled bending-stiffness measurements serve as practical probes for tracking how swelling gradients evolve in real time. Together, they provide a kinetic picture of how free liquid becomes bound and vice versa in both natural and synthetic porous media. Third, two contrasting case studies reveal the key governing parameters. This thesis identifies the water transport conditions under which passive *Erodium* awn transitions from an almost-linear imbibition regime to the classic Lucas-Washburn behaviour. It then determines the optimum conditions for liquid displacement in a synthetic electro-kinetic laminate with a fixed liquid volume. Finally, these insights are applied to a plant-inspired variable-stiffness laminate. A mirror-symmetric three-electrode stack pumps electrolyte between core and skins, creating sub-millimetre swelling gradients that change bending stiffness. The synthetic liquid-mediated solution for variable stiffness demonstrated in this work provides a lightweight, low-pressure alternative to pneumatic or thermal variable-stiffness actuators. In short, the thesis shows that liquids can be considered as distributed, reversible “mechanical processors” that give soft robots adaptive stiffness, shape, and sensing—core traits of embodied intelligence. The study yields concrete design rules: anisotropic considerations for intended flow direction, optimum pore fill ratio ranges, fast and slow liquid pumping considerations, and architectural cues for multi-directional liquid redistribution for plant-inspired stiffness modulation.

# LIST OF PUBLICATIONS

## Publications included in the thesis

I. Sarokin, Y., Aabloo, A., & Must, I. (2025). Are liquids part of embodiment?. In *Conference on Biomimetic and Biohybrid Systems*, accepted, in press

II. Sarokin, Y., Aabloo, A., & Must, I. (2025). Reflectometry of free water transport in the oriented capillaries of *Erodium cicutarium* seed awns: insights for hygromorph design. *npj Robotics*, *3*(1), 19.

III. Sarokin, Y., Aabloo, A., & Must, I. (2023). Plant-inspired rearrangement of liquid in a porous structure for controlled swelling. *Bioinspiration & Biomimetics*, *18*(6), 066005.

IV. Sarokin, Y., Aabloo, A., & Must, I. (2023). Charge-controlled swelling gradients at 200-µm resolution in an open-porous polymeric structure for compliance modulation. *Frontiers in Materials*, *10*, 1220421.

## Author's contribution

In Publications I–IV, the author was responsible for most of the research, hardware and software development, data analysis, and manuscript writing in all phases. Co-authors contributed to the manuscript writing and revision. The author's contributions per publication were the following:

I. Conceptualisation—framed the role of liquids in embodied-intelligence systems; defined the two-axis quadrant (active vs. passive control; internal vs. external exchange) and selected the two case studies (electrokinetic laminate; *Erodium* awn). Methodology—designed the comparative framework and criteria for mapping behaviours to the quadrant. Investigation—executed case-study analyses using published and in-house data. Data curation—compiled the literature dataset used for exemplars. Visualisation—created the quadrant and summary schematics. Writing—original draft and editing.

II. Conceptualisation—formulated an optical reflectometry approach to quantify free water in *Erodium cicutarium* awns. Methodology—designed the optical setup and analysis protocol. Software—wrote code for signal processing, fitting, and time-constant estimation. Validation—performed internal checks and repeatability tests; compared kinetic readouts across modalities. Formal analysis—separated free-water motion from bound-water swelling kinetics. Investigation—conducted experiments and measurements. Data curation—organised raw/processed datasets and metadata. Visualisation—prepared time-series and kinetic-parameter plots. Writing—original draft and editing.

III. Conceptualisation—proposed a low-pressure, bidirectional pump to create active swelling gradients in porous polymers. Methodology—designed and fabricated a mirror-symmetric carbon-electrode/PVDF-HFP laminate; established in-situ impedance mapping of pore-fill ratio (PFR). Software—developed control code and PFR-inversion routines. Validation-calibrated impedance vs. electrolyte concentration and assessed repeatability. Formal analysis—identified the optimal PFR operating window. Investigation—performed electrohydrodynamic pumping experiments. Writing—original draft and editing.

IV. Conceptualisation—proposed a charge-controlled, variable-stiffness laminate in which ion-electrosorption shuttles a fixed electrolyte between carbon–polymer layers to modulate flexural stiffness. Methodology—designed the three-electrode architecture; developed in-situ impedance readout and a custom bending-stiffness tester. Software—implemented instrument control and analysis pipelines. Validation—mechanical/electrical calibration and benchmark tests. Formal analysis—linked stiffness modulation to charge/PFR redistribution. Writing—original draft and editing.

## Publications not included in the thesis

V. Sarokin, Y., Aabloo, A., & Must, I. (2025). Erodium Awn's Water Transport Insights for Controlled Swelling Agent Rearrangement in Anisotropic Structures. In *Conference on Biomimetic and Biohybrid Systems* (pp. 179–192). Springer, Cham.

VI. Sarokin, Y., Becquer, V., Cattan, E., Aabloo, A., & Must, I. (2023, July). Charge-Dependent Flexural Rigidity of a Conductive Polymer Laminate for Bioinspired Non-thermal Compliance Modulation. In *Conference on Biomimetic and Biohybrid Systems* (pp. 109–116). Cham: Springer Nature Switzerland.

# ACRONYMS AND SYMBOLS

| | |
|---|---|
| AI | Artificial Intelligence |
| ATP | Adenosine Triphosphate |
| CV | Cyclic Voltammetry |
| CT | Computed Tomography |
| dB | Decibel |
| ED | Electrodialysis |
| EHD | Electrohydrodynamic |
| EIS | Electrochemical Impedance Spectroscopy |
| EMIM Otf | 1-Ethyl-3-methyl-1H-imidazol-3-ium trifluoromethanesulfonate |
| FFT | Fast Fourier Transform |
| FO | Forward Osmosis |
| FWHM | Full Width at Half Maximum |
| $FWHM^S$ | FWHM for scattered light |
| $FWHM^T$ | FWHM for transmitted light |
| HASEL | Hydraulically Amplified Self-healing Electrostatic Actuator |
| $H^+$-ATPase | Proton Adenosine-Triphosphatase |
| MDSD | Most Different Systems Design |
| MP | 4-Methyl-2-Pentanone |
| MRI | Magnetic Resonance Imaging |
| NIR | Near-Infrared Spectroscopy |
| NHX | $Na^+/H^+$ Exchanger |
| NMR | Nuclear Magnetic Resonance |
| NDVI | Normalised Difference Vegetation Index |
| OCT | Optical Coherence Tomography |
| OM1 | Optical Multimode (class 1) |
| PC | Propylene Carbonate |
| PFR | Pore-Fill Ratio |
| PVdF-HFP | Poly(vinylidene fluoride-co-hexafluoropropylene) |
| PVC | Poly(vinyl chloride) |
| SEM | Scanning Electron Microscopy |
| $t_{coil}$ | Coiling onset time |
| $t_D$, $t_D^S$, $t_D^T$ | Depletion time, Depletion time for scattered and transmitted light |
| $t_H$ | Hydration time |
| UV | Ultraviolet |
| V-ATPase | Vacuolar-type $H^+$-ATPase |
| V-PPase | Vacuolar $H^+$-Pyrophosphatase |

# 1. INTRODUCTION

## 1.1 Liquid–Mediated Embodied Intelligence

As technology advances, embodied and artificial intelligence are becoming part of everyday life [1]. At its core, embodied intelligence is a framework for designing and studying intelligent behavior in agents that have physical bodies and operate within real environments [2]. It focuses on the ongoing interaction between an agent and its surroundings, shaped by the body's physical properties and constraints. Unlike traditional AI, which runs entirely in software, embodied systems sense and act through their physical form, so their "thinking" is deeply influenced by their shape and context [1]. Soft robotics is inspired by biological forms, exploiting morphological computation, where the body itself handles many computational tasks. This approach shifts processing load away from the controller and allows for safe, adaptive interactions with unpredictable environments.

Recent advances have sparked a wave of projects applying embodied intelligence in real-world settings. For example, Gemini Robotics, introduced in 2025, treats physical actions as an output channel in a multimodal model and uses advanced spatial understanding to support embodied reasoning and direct robot control [3]. Similarly, Sanctuary AI's Phoenix Humanoid Robot is promoted as the world's first humanoid with bio-inspired embodied intelligence [4]. Across the high-tech sector, efforts now span embodied reasoning, biomimetic design, operation in unstructured environments, and the seamless integration of AI with physical form. Taken together, these initiatives aim to fulfil a long-standing vision: robots that match biological organisms in flexibility and adaptability by unifying mind and body in both design and function.

Embodied intelligent systems promise broad versatility, setting them apart from single-purpose industrial robots and positioning them as transformative as personal computers or smartphones. Remarkably, intelligence does not reside in software alone: the mechanical body itself contributes sensing and morphological computation, serving not just as an interface to the outside world but as a physical processor whose intrinsic properties and real-time reactions retain part of the system's intelligence. Their general-purpose nature points to a substantial new market, with industry leaders predicting that embodied AI will succeed today's screen-based assistants by interacting physically with the world [5]. Dubbed the "Year of Embodied AI," 2024 reflects strong optimism that breakthroughs in generative AI and large language models will drive real-world embodiment solutions [6]. That confidence has fueled a surge in both private and public investment. Market research values the global embodied AI market at about $2.53 billion in 2024, projecting it to reach $4.07 billion by 2033—a compound annual growth rate of roughly 5.4 percent [7].

In parallel, soft robotics reframes the robot's body as the primary problem-solver, not merely a soft shell. Compliant skins, fibre-reinforced lattices, and

variable-stiffness joints let a robot negotiate cluttered or unpredictable terrain by passively changing shape, absorbing shocks, and re-directing forces before any controller intervenes [8]. Hardware innovations—such as variable-stiffness components [9] and bio-inspired structures [10]—extend capabilities of soft robotics without adding heavy computational demands. Longstanding ideas like morphological computation and adaptive behavior are now practical [11]. Morphological computation holds that a robot's body can perform tasks usually reserved for its controller. Modern soft robots often use multifunctional parts that serve as both structure and sensor or actuator, allowing them to react naturally to external forces. At the same time, Rodney Brooks' subsumption architecture—stacked layers of simple behaviors that respond directly to environmental cues without central planning—continues to influence designs, now augmented with feedback loops and reinforcement learning [12].

Despite these advances, significant challenges remain in realizing the full potential of embodied intelligence, a field that is still largely experimental and guided more by biological insight than by formal design tools [13]. Today's robotic hardware—especially in soft robotics—still falls short of biological systems: what is currently recognised as 'embodied AI' often relies on extensive, high-density sensorisation, and building such a durable, finely instrumented body remains a formidable challenge. Embodied intelligence seeks to solve part of those physics tasks through the body itself, shifting effort away from high-bandwidth sensing toward passive shape, compliance, and material properties that 'compute' in real time. Integrating sensors, actuators, control systems, and AI into a single, dependable engineering system adds further complexity. Even so, designers must still marry a deliberately 'intelligent' body with just enough sensing, actuation, and control to yield a dependable whole. Unlike natural organisms, which distribute control, most robots rely on centralised architectures, leading to issues like latency between sensing and action, mismatches between virtual models and actual hardware, and software fragility; reinforcement-learning methods that train policies directly on hardware mitigate these issues, but they too depend on bodies that tolerate delay and inexact modelling.

Embodied intelligence, first defined by Francisco Varela for living organisms [14], still informs the design of bioinspired cognitive systems. Efforts to recreate it in synthetic agents often stall because we lack a clear, system-level understanding of how embodied intelligence emerges in nature. Just as AI theory leans on neuroscience, building embodied intelligence in machines depends on understanding its origins in living beings. Amoebae—often perceived as simple, non-neural organisms—nevertheless exhibit embodiment by navigating complex environments and processing information without any nervous system [15]. Across diverse life forms, a common feature stands out: their bodies consist of fluid-filled cells containing organelles. Liquid, therefore, appears fundamental to embodied intelligence, prompting interest in the specific role it plays—a role whose precise mechanisms are still not fully understood.

To address these challenges, we look to living organisms—specifically plants—that use fluid-based mechanisms for adaptive behavior. Plants adjust their stiffness in response to environmental stresses (e.g., awns of *Erodium cicutarium*) and growth needs by displacing water. Swelling alters their material properties without any central control. Through osmosis and ion regulation, plants manage water flow within and between cells, using both internal storage and uptake from the environment to adapt to stimuli like light or gravity. In the context of liquid-mediated embodied intelligence, water redistribution enables a transition between compliant, sensing-optimised states and rigid, load-bearing states on demand, forming the conceptual and experimental foundation for the synthetic variable-stiffness systems presented in later chapters.

## 1.2 Problem statement

Despite substantial progress in exploring individual aspects of liquid transport, major barriers persist in clarifying how liquids contained within natural liquid-mediated systems contribute to embodied intelligence and understanding how to translate the underlying design principles into synthetic architectures capable of emulating plant-inspired stiffness modulation. First, conventional studies often overlook the transient interactions between free and bound liquid phases, and the role of the liquid's state interplay in embodied intelligence remains ambiguous. Second, while natural hygromorphic systems are able to distribute liquid rapidly due to their efficient anisotropic capillary structure (*Erodium cicutarium*), the details of this mechanism are not very clear [16]. Understanding this mechanism enables the translation of passive anisotropic capillary cues from natural hygromorphs into an actively controlled liquid-routing architecture with programmable swelling gradients and stiffness. Third, there is currently no synthetic architecture that simultaneously (i) achieves localised, reversible modulation of material properties via controlled host–liquid interactions and (ii) routes a fixed liquid volume multidirectionally within the body; resolving this integration challenge is a prerequisite for plant-inspired variable-stiffness design.

## 1.3 Aim

The following aims are addressed in this doctoral thesis:

- To elucidate the principles governing both controlled and environment-determined liquid displacement in swellable porous media
- To demonstrate how oriented liquid transport can be harnessed to process information through the structural and material properties of liquid-mediated systems.
- To develop methods for measuring free-liquid displacement and free-to-bound liquid conversion kinetics.

- To formulate and validate a liquid-mediated variable-stiffness principle for synthetic bodies, linking controlled liquid redistribution to programmable local material properties.

By addressing these interconnected challenges, the proposed research intends to:

- Explore the concept of liquid-mediated intelligence
- Bridge the gap between passive and active control of liquid transport mechanisms in isotropic and anisotropic swellable structures with transient and constant liquid content.
- Design a liquid-mediated variable-stiffness system.

The ability to control material properties through liquid redistribution represents a form of mechanical computation, where the material itself becomes an active participant in environmental adaptation, analogously to how plants use liquid movement to achieve complex movements and adaptability. The research primarily focuses on synthetic polymer systems and selected natural models, specifically examining interactions between porous matrices and specific states of embodied liquids, and non-unidirectional liquid displacement to achieve adaptive behaviour.

## 1.4 Objectives and Research Questions

Objective 1:

Understanding the role of liquid in the concept of embodied intelligence.

*1.1 What is the role of liquids in embodied intelligence, and how does this role differ based on whether the liquid is in a bound or free state? (Publication I)*

*1.2 What practical design guidelines follow from choosing (i) active versus passive control and (ii) internal liquid confinement versus environmental liquid exchange, when using liquids as functional elements in intelligent systems? (Publications II and III)*

Objective 2:

To develop methods for free and bound liquid real-time tracking and to analyze free liquid displacement and free-to-bound transition kinetics in porous morphing systems.

*2.1 How to access liquid content variation (separately free and bound) locally in porous structures? (Publications II and III)*

*2.2 What are the kinetic parameters associated with liquid redistribution in swellable porous structures and the interplay between free and bound states? (Publications II and III)*

Objective 3:

To design a synthetic adaptive laminate comprising controlled and interstitial internal swelling agent redistribution.

*3.1 How to actively pump an electrolytic solution multidirectionally within an open-porous isotropic polymeric laminate to modulate stiffness? (Publication IV)*

*3.2 How to experimentally characterise the stiffness modulation due to bound liquid redistribution? (Publication IV)*

## 1.5 Research Methodology

This thesis proposes the following roadmap, which will include the main stages of the development of a plant-inspired approach for liquid-mediated embodied intelligence, the associated challenges, and the search for their solutions.

*Overall strategy—How does the study progress from observation to design?*

Develop methods for liquid displacement and free-to-bound conversion kinetics assessment in porous swellable structures, such as plants (considering the evolutionary mechanisms nature has developed) and synthetic systems.

## 1.6 Contribution of the Thesis

Overall, this dissertation seeks to bridge the gap between the predominantly passive liquid control methods used in current synthetic hygromorphs and the diverse, active strategies observed in nature. Bridging this gap matters because active, plant-like liquid redistribution makes stiffness and shape programmable in space and time, reversible, and safe at low temperature—capabilities that passive hygromorphs lack and that conventional actuators struggle to deliver at submillimetre resolution. By treating liquids as active mediators of morphology and control, developing tools to resolve free vs. bound phases in real time, and deriving design rules instantiated in a multilayer electrokinetic laminate, the thesis provides the theoretical, methodological, and architectural elements needed for this transition. This dissertation is a cover document (comprises publications I, II, III, and IV). The descriptive chapters synthesise, contextualise, and extend the results from these publications [I–IV], which are included in the Appendices. The narrative provides an integrative framework, method unification, and cross-case discussion.

Theoretical Contribution:

This thesis advances the theory of embodied intelligence by explicitly incorporating liquids as control-relevant physical media: changes in their amount, spatial distribution, and state (free vs. bound) directly set when and where shape and stiffness change, thereby coupling environmental stimuli to mechanical response. We propose a new framework in which free and bound water phases serve not only as passive carriers or structural elements, but as mediators that couple environmental stimuli to mechanical response. We show, on natural (*Erodium*) and synthetic (electrokinetic system) exemplars, that controlling liquid redistribution influences where and when mechanical response occurs; this motivates treating liquids as contributors to embodied adaptation rather than as mere payload.

Methodological Contribution:

This thesis introduces an integrated toolkit that resolves free- and bound-water dynamics and their mechanical consequences in real time. Fibre-optic reflectometry in backscatter and ballistic-transmission modes tracks free-water fronts and yields kinetic parameters such as balistically transmitted and scattered *FWHM* (Full Width at Half Maximum) and capillary depletion times ($t_D$), together with coiling onset ($t_{coil}$), which together describe retention, depletion, and the free-to-bound transition rates. Simultaneous hygroactuation readout (rotation) quantifies the bound-water accumulation driving swelling, linking optical kinetics to mechanical response. For synthetic laminates, in-situ impedance provides a local proxy for pore-fill ratio (electrolytic conductance) during controlled liquid redistribution, while a voice-coil bending rig measures stiffness modulation under identical loading and timing. Taken together, these co-registered modalities provide a sufficient set of parameters required for design and control: (i) front velocity and retention (*FWHM*), (ii) depletion-limited free-to-bound conversion rates ($t_D$), (iii) local pore-fill ratio from impedance, and (iv) the stiffness modulation under active routing.

Applied Contribution:

From these insights, we derive concrete design guidelines for soft robots and adaptive materials with localised stiffness control. Key principles include: (1) engineering anisotropic porosity to accelerate free phase transport and direct swelling; (2) tuning pore-fill ratio to balance swelling magnitude against fluid connectivity for active control; and (3) integrating electrosorption elements into swellable matrices in a multilayered configuration to achieve on-demand stiffness variation.

As a result, this thesis covers a significant gap in our understanding of how the interplay between liquid states (free and bound), combined with active control of liquid displacement, contributes to the emergence of adaptive behaviour in synthetic systems.

## 1.7 Thesis Structure

This thesis builds upon four distinct yet complementary investigations:

The first publication introduces a two-axis classification of liquid-mediated systems by control (active vs. passive) and exchange (internal vs. external). To anchor the framework, it previews two model systems—a synthetic electrokinetic laminate (Quadrant II) and a natural Erodium awn (Quadrant IV)—which are analysed in the following chapters in this thesis; within this framework, bound liquids can be integral parts of the embodiment, whereas free liquids may act as mobile intermediaries or environmental agents.

The second publication focuses on passive capillary-driven water transport in natural anisotropic cellulose-based structures (e.g., *Erodium cicutarium* awns). Using optical reflectometry, it investigates the mechanisms of rapid water displacement associated with capillary action and hydrophilicity frontline propagation inside a natural hygromorph and its subsequent swelling.

The third publication demonstrates an active (electrosorptive) liquid transport within a synthetic isotropic porous polymeric matrix. It shows how the local volume of ions and solvent manipulation creates controllable swelling gradients.

The fourth publication demonstrates an interstitial liquid redistribution based on active liquid transport (presented in the previous publication) for structural compliance variation of a thin adaptive structure by multioriented liquid displacement: liquid transport between exterior and interior.

The thesis is structured into seven main chapters:

Chapter 2: State of the art in Plant-inspired Embodied Intelligence

Reviews the physiological foundations of liquid-mediated embodied intelligence in plants—covering liquid transport mechanisms, stiffness modulation via material and structural changes, and the roles of free versus bound water—and surveys bio-inspired approaches to replicate these functions in soft robotics.

Chapter 3: Original Approach. Liquid-mediated Systems for Embodied Intelligence

Derives design cues from plant liquid-mediated mechanisms and formalises them into a synthetic architecture for embodied intelligence, specifying the control variables and structural patterns later used to realise actively routed liquid redistribution and variable stiffness.

Chapter 4: Methods

Describes the model systems and natural sample preparation; the assembly of two- and three-electrode electrokinetic laminates; and a co-registered measurement workflow that quantifies free- and bound-water dynamics together with their

mechanical consequences. Specifically, it details fibre-optic reflectometry (backscatter and ballistic transmission) for free water, hygroactuation extent read-out to infer bound water, in-situ impedance as a proxy for pore-fill ratio, and a mechanical bending (combined with impedance measurements) setup for stiffness characterisation, along with synchronisation and kinetic parameters extraction.

Chapter 5: Results on Dynamic Interplay of Liquid States, Structure, and Materials

Presents two case studies. First, it analyses passive, transient liquid displacement and swelling kinetics in anisotropic plant structures. Second, it investigates active, constant-volume liquid redistribution and efficiency in a synthetic two-electrode laminate under electrokinetic control and analyses how active liquid control drives reversible stiffness modulation and shape change in the three-electrode laminate, quantifying adaptive performance.

Chapter 6: Discussion on Liquid-Mediated Systems

Brings together findings from Chapters 5 and 3 to compare measurement techniques, kinetic behaviors, control strategies, structural influences, and material effects, highlighting shared principles, design trade-offs, and implications for embodied intelligence systems. Next, it reflects on the broader implications of liquids as part of embodiment, intermediaries, and environmental media in embodied systems.

Chapter 7: Conclusions

Provides answers to research questions and outlines limitations and further work.

# 2. PLANT–INSPIRED EMBODIED INTELLIGENCE

## 2.1 Embodied Intelligence and Plant Physiology

Embodied intelligence is an emergent property that arises from the body's interaction with its environment [17–19]. It is defined as the capacity of a system, whether biological or artificial, to integrate sensory inputs, physical structure, and motor actions in order to generate goal-directed behaviour (or simply adaptation). This perspective challenges the traditional view that intelligence is solely the result of abstract, centralised computation, positing instead that the physical form and material properties of an organism are integral to its cognitive capabilities. In essence, embodied intelligence emphasises that cognition is deeply rooted in the dynamic interplay between an organism's morphology and its environment. Liquids, for example, play a fundamental role in the life processes of plants [20], not only sustaining physiological processes but also providing adaptability and facilitating complex interactions with the environment [21].

Water is indispensable to plants, serving as a universal solvent that facilitates the transport of nutrients and minerals from the soil [22], signalling molecules that coordinate various cellular processes [23], and being a critical reactant in photosynthesis [24]. Beyond these vital physiological roles, water underpins the expression of adaptive behaviours, as it maintains cell turgor, ensures structural stability, and enables cell expansion during growth [25], allowing plants to effectively respond to external stimuli and adjust their growth in complexly structured environments. In the realm of liquid-mediated embodied intelligence, plants offer an inspiring model for developing engineering solutions with adaptive behaviour through their sophisticated liquid redistribution strategies, involving passive (e.g., capillary action, transpiration pull, and root pressure) and active (e.g., interstitial water exchange between cells and extracellular matrix). In these natural systems, intelligence is not centralised but emerges from water exchange with the environment and within the body, the dynamic interplay of free and bound water, and solid-liquid interactions (i.e., swelling).

As this work is motivated to develop embodied intelligence systems expressing liquid-mediated adaptive behaviour through structural and material properties modulation inspired by plants, a systematic understanding of the relationship between transient liquid-solid interactions and the emergence of embodied intelligence is needed.

## 2.2 Liquid–mediated Mechanisms in Plants

In general, all processes of liquid transport in plants are associated not only with physiological processes but also with adaptive behaviour and can be divided into passive and active. Passive liquid transport in plants refers to the movement of water and solutes through physical processes that do not require metabolic energy (from photosynthesis and cellular respiration), a cornerstone of energy-efficient

adaptation in biological systems. On the contrary, active liquid transport in plants requires energy input to displace water against concentration gradients or induce such concentration gradients. An intricate interplay of these processes further complicates a clear understanding of the role of liquid in the expression of embodied intelligence in plants. For instance, transpiration pull is generated by water evaporating from the leaf surfaces, which creates a negative pressure in the xylem that pulls water upward from the roots [26]; while guard cells don't directly produce this pull, they control the opening of stomata and thus regulate the rate of transpiration, indirectly influencing the strength of the transpiration pull [27]. Notably, this plant's liquid-mediation processes involve the exchange of liquid with the environment (water uptake and transpiration) and internal redistribution. Moreover, these two processes involve both the exchange of liquid with the external environment (water uptake and transpiration) and its redistribution within the plant body (as active transport of potassium ions regulates turgor pressure for the stomatal aperture).

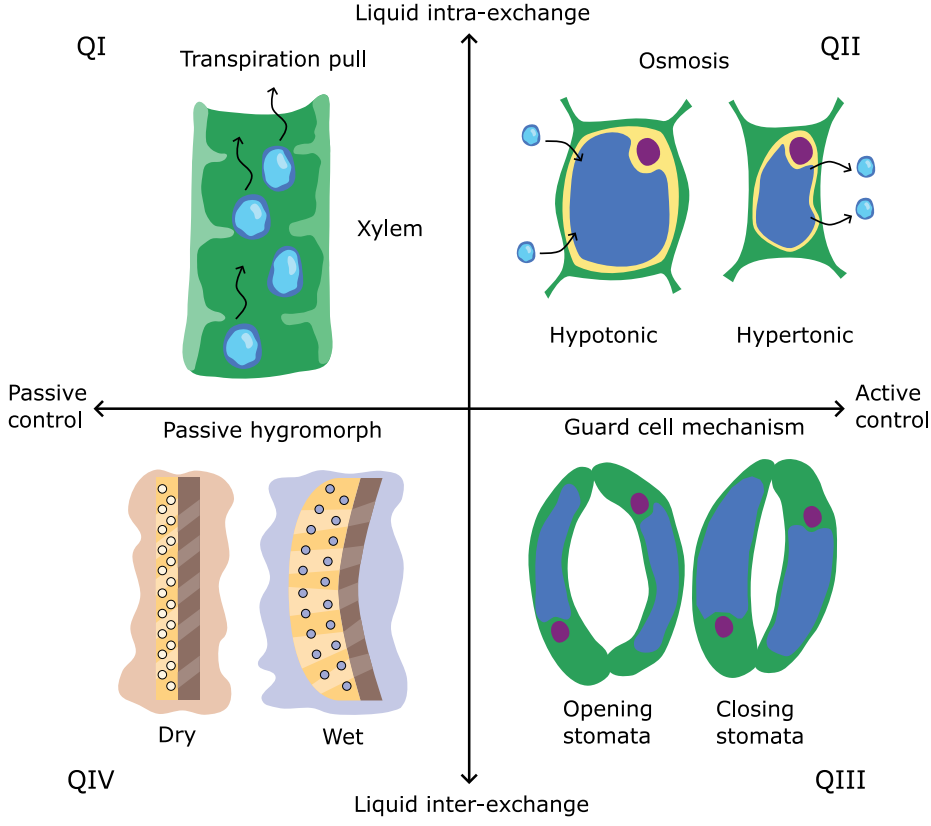


Figure 1. Quadrant model for plants. Categorisation of liquid manipulation strategies in plants.

With a focus on a deeper understanding of the role of the liquid in the expression of embodied intelligence in plants, where water mediates both passive and active responses through external exchange and internal redistribution, we can systematise these processes into four–quadrants. In this framework, the first axis distinguishes between passive control, where water moves in response to the environment, such as absorption and evaporation, and active control, which involves processes that require energy input from the plant, like phloem loading and stomatal regulation. The second axis differentiates between inter-exchange, where water is exchanged with the environment (as seen in water uptake and hygroscopic movements), and intra-exchange, which refers to the internal redistribution of water within the plant's tissues. This dual-axis model (Figure 1) yields four quadrants isolating the role of water in the emergence of embodied intelligence in specific liquid mediation strategies, which can be exemplified as follows.

A prominent example of Quadrant I (passive, intra-exchange) is how trees manage various forces to maintain structural integrity and functionality through the hydrostatic water redistribution within the xylem. Water acts not only as a medium for transport, elucidated by the Cohesion-Tension Theory [26], but also in providing mechanical support, counterbalancing these forces by redistributing pressure hydrostatically [28]. When a tree bends, the xylem on the tension side (the side that is being stretched) develops lower pressures, while the compression side may experience relatively higher pressures. This difference creates a pressure gradient that can drive water movement from regions of lower tension to areas of higher tension, helping to balance the hydraulic forces within the tree.

Quadrant II (active, intra-exchange) is exemplified by plants' active turgor pressure modulation, the internal pressure exerted by water against cell walls, through a sophisticated interplay of molecular mechanisms. This pressure is essential for cell rigidity, growth, and adaptation to environmental changes, particularly water availability. For instance, plants control turgor pressure by managing water flow through aquaporins [29–30], which are protein channels in cell membranes. These channels can open or close based on signals like calcium levels or temperature, helping plants adjust to water availability. For example, during drought, aquaporins might reduce water loss to maintain cell rigidity. Another critical mechanism for turgor pressure regulation is the transport of ions into or out of vacuoles, mediated by ion transporters and proton pumps. Proton pumps, such as V-ATPase and V-PPase, create a proton gradient across the vacuolar membrane [31], driving ions like sodium and potassium into the vacuole via transporters like NHX antiporters. This process helps balance internal pressure by adjusting the cell's osmotic potential. To regulate cellular osmotic potential and maintain turgor pressure, plants also use osmoregulation, a mechanism that involves the accumulation or depletion of osmolytes like sugars and proline [32]. Proline accumulation, for instance, lowers the osmotic potential, drawing water into cells to maintain turgor. This is vital during drought or salinity stress, ensuring cells stay firm and functional. Apart from turgor, liquid is displaced between different parts of the plant. A key example is the phloem system, which

transports sugars from photosynthetic leaves (sources) to non-photosynthetic tissues (sinks) like roots or fruits. This process, driven by the pressure-flow hypothesis, relies on ATP-powered transporters to actively load sucrose into phloem sieve tubes, generating turgor pressure to propel sap flow [33].

Active regulation of liquid exchange with the environment (Quadrant III) is exemplified by stomatal function. In this context, the effect—actively controlled gas and water-vapour exchange across the leaf surface—belongs to Quadrant III, whereas the actuator that produces this effect is the guard-cell pair, which itself belongs to Quadrant II (active, intra-exchange) system: guard cells modulate their turgor by ion transport (notably $K^+$) across the plasma membrane and aquaporin-mediated water flux, thereby opening or closing the pore. This facilitates gas exchange, including the uptake of carbon dioxide ($CO_2$) for photosynthesis and the release of oxygen ($O_2$), while also controlling water loss through transpiration. The turgor status of guard cells determines the degree of stomatal opening, with turgid guard cells leading to open stomata and flaccid guard cells resulting in closure [34]. Despite intrinsic similarities with active turgor pressure modulation presented above (which is primarily mediated by the movement of ions, particularly potassium ($K^+$), across the plasma membrane) [27] and association with the passive mechanism of transpiration in xylem, this mechanism exemplifies the actively regulated water exchange. This ion transport is tightly regulated by various signalling pathways (environmental and hormonal), further providing clues for liquid-mediated adaptive behaviour inspired by plants.

Passive adaptation to environmental conditions is presented in full by natural hygromorphic structures (Quadrant IV), such as the scales of pine cones and the awns of *Erodium cicutarium*, which have evolved to change shape in response to humidity, enabling them to adapt to their environment passively. These structures are particularly notable for their ability to absorb moisture, triggering structural changes like swelling and bending, which are critical for functions such as seed dispersal and self-burial. Pine cone scales reversibly open and close based on moisture levels [35]. This movement is driven by the differential expansion of two layers: sclereid cells and sclerenchyma [36]. When the scales absorb moisture, the sclereid layer expands more than the sclerenchyma layer due to differences in the orientation of cellulose microfibrils in their cell walls. The mechanism is driven by the anisotropic swelling and shrinking of the tissues, with the sclereid layer showing greater hygroscopic response due to its porous structure and differences in the orientation of cellulose microfibrils (anisotropy) [36]. Notably, despite efforts aimed at a more detailed understanding of water absorption processes in pine cones, the mechanical contribution of these tissues to movement, as well as their behaviour during water absorption and desorption, remains unclear [16].

## 2.3 Material and Structural Stiffness Modulation in Plants

Plants are not static structures; rather, they actively modulate their mechanical stiffness through a combination of material and structural adaptations, with liquids playing a key role in mediating these dynamic changes to meet functional needs. Unlike engineered structures that rely on fixed materials, plants can alter cell wall composition, water content, and growth patterns to stiffen or soften tissues as needed [37]. These adjustments occur across scales—from the nanoscale arrangement of cell wall polymers to the macroscale architecture of stems and leaves—enabling plants to remain upright, withstand wind or gravity, and even move their organs. In contrast to active stiffness modulation, natural hygromorphic systems like the Erodium awn have evolved sophisticated ways to modulate stiffness and shape without metabolic input through their material composition and structural design. The awn's performance—dry-state coiling and humidity-induced uncoiling—arises from differential swelling in its layered tissues and moisture-dependent material properties, converting humidity changes into reversible torsional deformation [38, 39]. In essence, the awn is a composite structure with heterogeneous material properties and geometry that together produce coiling behavior [40, 41].

To identify the most relevant approach to adaptive behaviour expression, this study examines how plants modulate their stiffness via material property changes (such as hydration) and geometric adaptations (structural reinforcements). In practice, these mechanisms often work together; for instance, a stem may both thicken (geometric change) and lignify (material change) to become stiffer.

### 2.3.1 Changes in Material Properties and Composition

An actively modulated plant's stiffness (represented by Quadrant II and III) arises from the composition and structure of its cell walls and the turgor (internal pressure) within its cells. The primary cell wall is a composite of four basic building blocks—cellulose, hemicellulose, pectin, and lignin [42]. By altering cell wall composition or thickness, plants can modulate stiffness during development and in response to stimuli. In this thesis, the following wall-remodelling mechanisms are treated as developmental, structural cues that set baseline stiffness and anisotropy rather than as Quadrant processes (QII–QIII): lignification, secondary wall deposition, cellulose microfibril orientation, and polymer cross-linking. Adding lignin (a rigid, hydrophobic polymer) and forming secondary walls substantially increases wall stiffness and strength [43]. In collenchyma—the extensible support tissue of young stems—cell walls thicken during growth; later, these cells may undergo sclerification (conversion to sclerenchyma) by lignifying the newly deposited material, becoming much stiffer. The microfibril angle and the extent of cross-linking determine the stiffness–extensibility trade-off: a low microfibril angle (fibres aligned closer to the load axis) yields high tensile stiffness, whereas a higher angle permits greater stretch [42]. Under sustained mechanical bias, reaction wood alters both composition and microfibril angles (tension wood in

hardwoods is richer in cellulose; compression wood in conifers is richer in lignin) to restore upright growth [44]. In our context, these growth-mediated changes provide a long-term material–structural baseline on which liquid-mediated modulation (turgor, hydration) and active control operate.

More interestingly, plants can actively alter the mechanical properties of walls through enzymes and structural proteins. For instance, expansin proteins induce wall loosening, increasing extensibility for growth. While expansins primarily facilitate expansion, their activity (lowering wall pH to untether polymer bonds) effectively reduces stiffness, allowing cells to extend [45]. Conversely, peroxidases and lysyl oxidases can create new cross-links between wall polymers (like between pectin and structural proteins or between lignin units), increasing wall rigidity. Water content plays a special role in plant mechanics. At the wall scale, interfacial (bound) water plasticises the polysaccharide matrix, so adding or removing bound water softens or stiffens the wall, respectively [46]. In the quadrant model, this mechanism operates across multiple quadrants: it underpins passive hygromorphic swelling in pine cones and *Erodium* awns (QIV), modulates effective wall compliance during turgor-driven, actively regulated processes such as guard-cell actuation and osmotic adjustment (QII–QIII), and accompanies passive hydrostatic redistribution within tissues (QI). Thus, bound-water dynamics are not confined to a single class of process; they couple with both active and passive liquid flows to tune stiffness *in situ*. The effect of water in detail will be discussed in a later section.

Through these material-level adjustments, plants achieve an impressive range of mechanical properties. For example, parenchyma (storage tissue) can have Young's modulus below 1 MPa (very soft), whereas dense wood from palm stems can reach 30 GPa (as stiff as some metals)—a span of five orders of magnitude in stiffness achieved by variations in water content, cell wall makeup, and cellular structure [42]. This versatility in material properties underlies many of the stiffness-modulating strategies that plants use in growth and in responding to their environment.

In passive natural systems (representing Quadrant IV), the stiffness modulation is attributed to highly hygroscopic properties of the materials. For instance, the key aspect of the *Erodium* awn's swelling affinity is the differentiation of material properties across its cross-section and along its length. The awn is not a uniform material; instead, it has distinct tissue layers with different compositions and hygromechanical responses, as discussed below.

### 2.3.2 Geometric and Structural Adaptations

Beyond the intrinsic material properties of cells, plants also change their stiffness by altering structural layout—the geometry of tissues, organs, and their arrangement. Even with the same material (same cell wall composition), a different geometric configuration can yield very different mechanical performance (analogous to how a hollow tube is stiffer in bending than a solid rod of the same mass).

Plants exploit geometric principles such as cross-sectional shape, tissue distribution, and organ curvature to modulate stiffness and stability.

Many plant stems and petioles have evolved optimal cross-sectional designs for stiffness. A common strategy is to concentrate strong tissues toward the periphery of the stem and have a lighter core—essentially forming a "tube" structure that maximises the second moment of area (and thus bending stiffness) for a given amount of material [47]. Plants often add or rearrange specific tissues as reinforcement in strategic locations. Vascular bundles in leaves and non-woody shoots usually include caps of fibres that act as strengthening ribs running along the organ [37]. In palm stems and other monocots, these vascular fibre caps are the main contributors to stiffness, essentially functioning like rebar in concrete. Plants sense mechanical stimuli like wind, touch, or vibration and often respond by altering their growth form—a phenomenon called thigmomorphogenesis. Repeated mechanical stress usually leads to stockier, stiffer plants: for example, trees in windy areas or those experimentally brushed or flexed regularly tend to grow shorter, with thicker stems and increased secondary growth (wood), compared to sheltered plants [44].

The main difference between many passive natural systems and those where metabolic processes occur is that their stiffness always decreases with an increase in the volume of free water, as the material swells and no pressure forms internally (as in the case of turgor). Beyond material composition, the geometry and microstructure of the awn are crucial in modulating its stiffness and directing its motion. *Erodium* awns have a distinct layered morphology and fiber architecture that produces coiling. These layers are bonded together and oriented such that when the inner layer changes length (with moisture), the whole awn uncoils. The cellulose microfibrils in the *Erodium* awn's inner and outer layers are arranged in a tilted helical pattern within the cell walls. This architecture—a tilted cellulose fiber helix—is what causes the awn to twist as it dries. When the cells of the inner layer lose water, the inner layer contracts mostly lengthwise (since the helical fibers constrain circumferential shrinkage, the cell shortens instead), whereas the outer layer does not contract as much. The result is a torsional stress that makes the awn coil into a spring-like helix. Upon re-wetting, the inner layer swells and lengthens, unwinding the helix. Researchers found that in *Geraniaceae* awns, the precise angle of cellulose microfibrils in the inner layer determines whether an awn will purely bend, purely coil, or exhibit a combination. Species of *Geranium* with smaller microfibril tilt show bending, whereas *Erodium* (with a large tilt angle helix) shows pronounced coiling [40].

Thus, geometric adaptations, such as tweaking the cross-sectional design, adding structural reinforcements, and altering growth patterns (including reaction wood and stress-induced form changes, allow plants to achieve the needed stiffness and strength with minimal material use. These strategies are often parallel engineering principles (e.g., hollow beams, buttresses, tapered poles), yet they arise from growth and evolutionary selection, underscoring the convergent solutions to mechanical challenges.

## 2.4 Roles of Free and Bound Water in Adaptive Behaviour

Water is a critical factor in plant biomechanics, affecting stiffness both at the cell level and the whole-plant level. Plant tissues are often described as hydrostatic materials because their rigidity is maintained by water-dependent turgor pressure and tissue hydration [48].

### 2.4.1 States of Water and Mechanical Properties

An analysis of the aforementioned mechanisms reveals that water does not act as a homogeneous medium but exists in states—free and bound—that are critical to the plant's adaptive behaviour. Free water is defined as water that can move freely within the plant, such as in the xylem vessels or cell vacuoles, and in porous structures, and is present in most liquid transport mechanisms mentioned above (Quadrants I–III). Quadrant IV is a special case since the free liquid transitions into bound liquid and, thus, is not a prerequisite for hygroactuation—vapour-phase liquid can also initiate hygroactuation. This water occupies pore spaces, available for flow or evaporation, and allows the generation of hydrostatic pressure gradients essential for the translocation of sugars and other nutrients [49–50]. In contrast, bound water—tightly associated with cell walls and macromolecules—plays a stabilizing role, contributing to the water-holding capacity and structural integrity of plant tissues [51] and is present in all the aforementioned mechanisms, although it plays the most significant role in Quadrant IV. This duality is not merely a passive characteristic; rather, the dynamic interplay between free and bound water underlies many of the plant's responses to environmental stimuli.

The mechanical properties of plant organs depend not only on their solid constituents but also on their water content. A well-hydrated plant is generally firm and stiff, whereas a dehydrated plant becomes limp or brittle. This is because water in plant tissues serves multiple mechanical roles: it generates internal pressure (turgor) [52], it plasticises cell walls [45], and it contributes to tissue volume [53], all of which affect stiffness. Interfacial (bound) water is water tightly associated with macromolecules (such as the hydration shells of cell wall polymers), while bulk (free) water fills cell vacuoles, cell wall pores, and xylem conduits [48].

### 2.4.2 Bound Water Implications for Plasticity

Bound water acts as a plasticiser in cell walls, akin to how adding a plasticiser to a polymer can make it more flexible [45]. This hydration lowers the elastic modulus of the wall (softer, more extensible) but increases its toughness (ability to deform without cracking). If water is removed, the wall polymers draw closer together and form more non-covalent bonds, making the wall stiffer but also more brittle. In biological materials, a decrease in bound water content is correlated with increased stiffness of the matrix. For instance, in woody tissue (and even in animal tissues like bone or collagen), removing bound water (by drying) raises stiffness and reduces elasticity [54]. At fibre saturation, the cell walls cease

swelling, and the strength or stiffness of the wood no longer changes with additional moisture content due to limited swelling capacity [55].

Furthermore, the interplay between free and bound water becomes even more significant when considering passive and environmentally mediated processes, such as the hygromorphic responses observed in pine cones [35] and *Erodium* awns [38]. In these systems, movement and morphological changes are due to high swelling capacity and fast kinetics of free-to-bound water conversion, exemplifying how the dynamic balance between water states can drive adaptive behaviour.

### 2.4.3 Turgor–Driven Free Water Stiffening

While bound water governs baseline wall flexibility [45], free water under pressure (turgor) provides the rigidity of growing and non-lignified tissues [52]. Turgor pressure exerted by cell fluids against the cell wall results from the osmotic influx of water into the vacuole, making cells and tissues turgid. This is a reversible stiffness modulation: a wilted celery stalk, for example, becomes crisp again after rehydration as water restores the turgor pressure in its cells. In fact, many plants perform osmotic adjustments under drought—actively increasing solute concentration in cells (e.g., sugars, amino acids, ions) to draw in more water and maintain turgor, thereby keeping tissues stiff enough to function [45].

This interplay is effectively demonstrated by turgor pressure modulation (Quadrants II and III). While free water allows for quick adjustments in cell volume necessary for growth and movement, bound water serves as a buffering agent, maintaining a baseline of structural stability under variable osmotic conditions. Studies on macromolecular condensation suggest that bound water, through interactions with proteins, can buffer intracellular water potential by sequestering or releasing free water, providing a rapid defence against acute osmotic fluctuations [56]. For instance, a stomatal function is predominantly governed by changes in free water content within guard cells, whereas bound water helps retain cellular integrity during these fluctuations [27, 34].

The mechanical significance of turgor is seen clearly in plant organs that move. The pulvinus (a joint-like swollen base of leaves or leaflets in certain plants) uses turgor changes to move organs [57]. A famous example is the sensitive plant (*Mimosa pudica*), whose leaves fold and stems droop rapidly when touched. In Mimosa, the pulvini have motor cells on opposite sides; upon stimulation, cells on the lower side of the pulvinus rapidly lose turgor (by pumping out ions and hence water), while cells on the opposite side maintain high turgor [58]. This nastic movement illustrates how plants can actively redistribute free water to modulate stiffness and achieve motion locally.

### 2.4.4 Hydraulics of Xylem and Phloem

Water does not remain static in plants—it is continuously transported through specialised systems. The movement of water (and solutes) in plants occurs via two main pathways: the xylem, which primarily carries water and minerals from roots to shoots (mainly driven by passive physical forces), and the phloem, which distributes sugars (and with them, significant amounts of water) throughout the plant (driven by active pressure generation). These transport processes not only deliver the water that maintains turgor and hydration; they also create internal mechanical conditions (like pressure gradients) and enable rapid adjustments in water distribution that can affect stiffness.

The xylem is often viewed as a passive conduit—water is pulled up through transpiration-driven tension (the cohesion-tension mechanism) or pushed up partly by root pressure. However, the xylem is also a structural tissue: its cells (tracheids and vessels, along with fibres) have thick, lignified walls that contribute to the plant's mechanical support. The xylem's passive water transport is intimately tied to plant stiffness. The need to transport water efficiently and to support the plant body leads to adaptive compromises: xylem anatomy (vessel size, wall thickness, fibre content) is adjusted to ensure both adequate hydration of tissues and sufficient mechanical stiffness [59].

In contrast to the xylem's largely passive mechanics, the phloem represents an active hydraulic network essential to adaptive redistribution of water. Apart from the phloem's long-distance distribution function of nutrients in plants, it also moves a substantial volume of water. This pressure flow, described by the Münch theory [60], is an active process because it requires energy to load and unload sugars, thereby creating osmotic gradients. From a stiffness perspective, the phloem's role is more indirect than the xylem's—phloem transport can redistribute water in the plant and can affect local turgor changes in living cells [48].

Essentially, the phloem acts as a dynamic hydrostatic system that can source or sink water in different regions: water can move from the xylem into the phloem at sources (as sugars are loaded and draw in water), travel with the sugars and then exit back to the xylem or into cells at sinks. Active phloem transport is closely tied to osmotic adjustment mechanisms. When a plant is under stress or developing new organs, it can actively allocate resources (including water) via the phloem.

## 2.5 Free Water Detection

The dynamic of free liquid distribution is governed by both the geometry of the pore structure and the hygroscopic properties of the material composing it. Since this work aims to develop synthetic bioinspired systems that utilise liquid transport mechanisms analogous to those found in nature, it is essential not only to replicate the structure and mechanism but also to understand the dynamics of liquid movement and its dynamic interplay between states. Consequently, selecting an appropriate method for localizing liquid within the pores and determining its state is the next logical step.

Detecting bound water is relatively straightforward, as its presence can be inferred from changes in volume or stiffness; in contrast, quantifying local free water poses significant technical challenges, as it does not yield such clear signals. For example, while NIR spectroscopy demonstrates high sensitivity to overall water content [61], its applicability is limited in regions dominated by free water due to insufficient penetration depth and sensitivity constraints imposed by the intrinsic heterogeneity of natural materials. This heterogeneity, characterised by anisotropic structural properties and non-uniform composition, complicates the accurate characterisation of free water transport. Moreover, the sorption process is acutely sensitive to environmental variables such as temperature, humidity, and pressure fluctuations, further challenging the precise assessment of water dynamics. Modelling approaches have provided valuable insights into water distribution within porous media by exploiting these intrinsic properties [62–64]; however, their reliance on predefined materials and controlled conditions limits their applicability for natural structures.

To overcome these limitations, noninvasive imaging techniques have been increasingly employed to differentiate and monitor free versus bound water in real time. Techniques such as MRI and NMR—capable of exploiting the distinct relaxation properties of free and bound water molecules—have shown promise in mapping moisture distribution within porous cellulose structures [65–67]. MRI, with its high spatial resolution, allows for non-destructive visualisation of water movement within the xylem, although its temporal resolution is often insufficient to capture the rapid water rearrangements in hygromorphic systems, and its reliance on specialised facilities restricts field deployment. In parallel, neutron radiography provides another avenue to probe free water transport in wood [68, 69], yet its relatively low spatial resolution and long exposure times present practical limitations. Micro-X-ray CT, a potent tool for generating detailed cross-sectional views based on density differences, excels in detecting free water while remaining largely insensitive to bound water [70–72]. Nonetheless, challenges associated with the simultaneous detection of bound water and setup constraints hinder its use for transient hydration monitoring.

A more compelling alternative to the aforementioned techniques is the concept of measuring the change in refractive index mismatch during the filling of a porous structure with liquid. Porous cellulosic materials (like paper, wood, and plant fibres) are usually opaque or translucent due to strong light scattering at interfaces between solid cellulose (refractive index $n \approx 1.5$) [73] and air in the pore spaces ($n \approx 1.0$). This refractive index mismatch causes each fiber-air interface to reflect and scatter light, making dry paper or wood appear white or opaque. When free water fills the pores, it replaces air with a liquid of higher refractive index ($n \approx 1.33$), reducing the index contrast with cellulose. Recent studies confirm that as the moisture content in paper increases (water occupying the pores), light transmission rises monotonically because water's refractive index partially matches cellulose, significantly reducing scattering [74]. As a result, scattering is diminished, and the material becomes more transparent to light.

The refractive-index mismatch effect is useful for distinguishing free water (which occupies voids or lumen spaces and creates liquid/solid interfaces) from merely bound water within cell walls. Bound water is absorbed in the cellulose structure at a molecular level and does not create large index discontinuities (the cell wall swells but remains a single phase), so it has a smaller effect on light scattering. Free water, on the other hand, introduces a new phase with a different index, markedly altering scattering and transmission. For instance, in plant xylem (wood vascular tissue), a water-filled conduit is relatively translucent, but when it empties and fills with air, the sudden index change makes that conduit appear bright or "white" under light, indicating cavitation (air entry) has occurred [75]. These phenomena underscore the general principle: optical methods can sense free water in porous structures by detecting changes in light scattering and transmission caused by refractive index changes at interfaces.

Multiple light-based techniques have been developed to detect and quantify free water in porous media. Key methods include Optical Coherence Tomography (OCT) and laser-based transmission or scattering measurements. Each leverages the refractive index mismatch effect in different ways. Optical Coherence Tomography is a non-destructive imaging technique that provides cross-sectional views (tomograms) of semi-transparent materials by measuring back-scattered light as a function of depth. In porous media like paper or biological tissue, dry regions with many index mismatches produce strong scattering, while wet regions scatter less and may appear differently in the OCT image. As demonstrated, OCT can dynamically monitor liquid penetration into paper: as water sorbs into a cellulose fibre tissue, the OCT signal reveals time-varying scattering properties and clearly identifies the moving wetting front inside the paper [76]. However, the penetration depth is limited (a few millimetres at most in opaque, fibrous media), and multiple scattering can reduce image clarity in very thick or highly scattering samples. Despite these limitations, OCT is a powerful research tool for *in situ* monitoring of water movement in porous matrices with high spatial resolution.

A simpler implementation of optical methods is based on laser light transmission or scattering intensity measurements to sense moisture. These techniques generally involve shining a light through (or on) a porous sample and measuring changes in intensity due to water-induced transparency changes. For instance, Karppinen *et al.* [77] developed a method to monitor paper wetting by measuring the transmission of a monochromatic laser through the paper sample. By recording the transmitted intensity over time, they could distinguish different wetting regimes: pure capillary uptake (rapid filling of large pores) versus diffusive spread (slower, uniform moisture diffusion), as each produced a characteristic transmission as a function of the hydration period. Another implementation of this method involves the measurement of total transmitted light.

As mentioned earlier, the correlation between optical clarity and moisture content in paper is very strong, enabling useful applications, while wood is more challenging for optical moisture detection because of its thickness and heterogeneity. Nevertheless, optical methods find use in surface or near-surface moisture

detection. Despite NIR spectroscopy's limited penetration depth, it has been particularly successful in estimating the bulk moisture content of wood by sampling reflectance from the surface [78], suggesting potential application for methods based on laser light scattering intensity variation. Beyond wood, other plant tissues (such as leaves) are also susceptible to optical techniques for liquid detection. Optical methods like NDVI (Normalised Difference Vegetation Index) [79] in remote sensing correlate leaf water content with reflectance at certain wavelengths (often involving NIR), further supporting optical methods as a promising candidate for liquid detection in porous natural structures. Since this study aims to determine the kinetics of water movement in the capillary structures of natural hygromorphs—and with temporal resolution being the primary limitation—the optical method, particularly laser light transmission and scattering intensity variation, remains the preferred approach for reliably determining free water (isolated from bound water) with minimal temporal delay.

## 2.6 Liquid–mediated Synthetic Systems

Despite the ubiquitous use of liquids in intelligent systems, their role remains difficult to classify and, by and large, is situational from one study to another. Thus, the use of liquids in computing systems [80] implies processing information, where liquid can not be equated with the fundamental building block of digital electronics (i.e., transistors) but rather with the electric current powering the computation. Using a liquid that inherently exhibits intelligent behaviour through complex chemical and physical interactions with external input, rather than through interaction with embodiment, further complicates this paradigm: liquid metals [81] and liquid crystalline polymers in soft robotic applications [82], smart self-regulating fluid-based systems [83], electrorheological fluids [84], etc.

### 2.6.1 Plant–Inspired Liquid–Mediated Embodied Intelligence Systems

Drawing from the observation that plants simultaneously engage in both spontaneous and induced processes related to internal and external water exchange, liquid-mediated soft robotics systems can be represented within an analogous quadrant framework for systematic analysis of plant-inspired embodied intelligence: passive and active liquid transport systems in confined systems and in systems conceptualising exchange with the environment. (Figure 2), for exploration into the role of water in the emergence of embodied intelligence and the subsequent development of strategies for modulating structural properties.

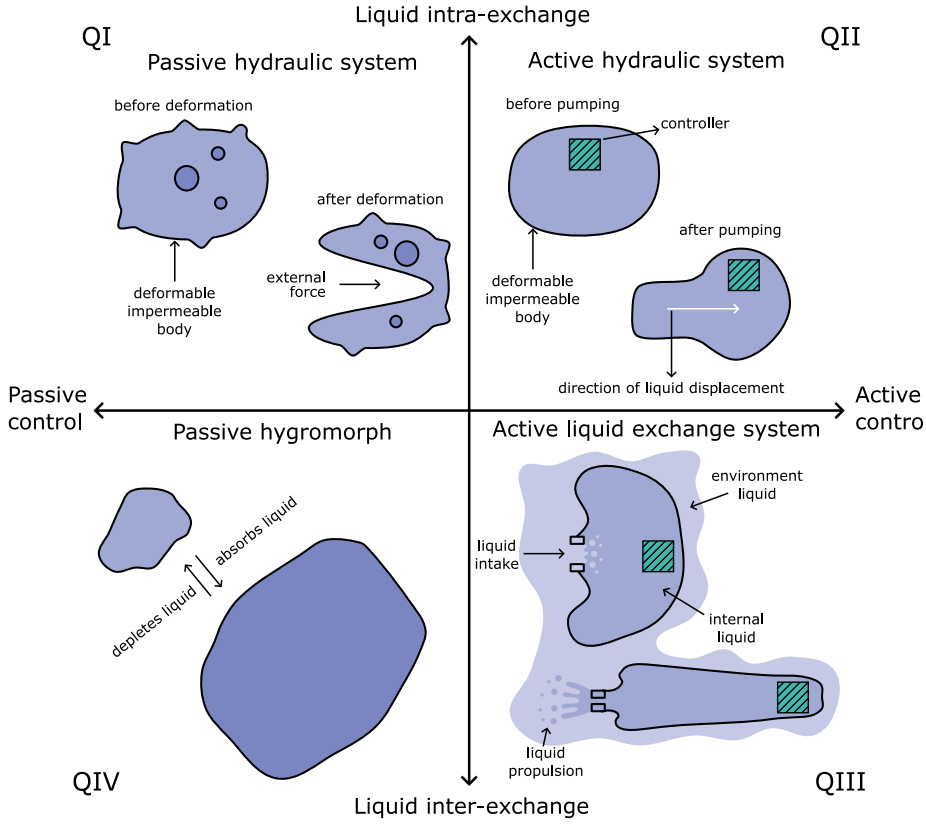


Figure 2. Quadrant model for synthetic systems. Categorisation of liquid-based synthetic systems based on control mechanisms and liquid exchange with the environment.

Quadrant I encompasses systems where a liquid circulates or redistributes within a closed network without any direct fluid exchange with the external environment and without active pumping. An example of passive confined liquid transport is a plant-inspired gravitropic soft robot [85]. They designed a soft actuator that autonomously bends in response to gravity by using a fluidic liquid metal circuit as a self-regulating weight and heater. This elegant design shows how passive physical phenomena (gravity-driven fluid flow) can be harnessed for self-regulating actuation, achieving an electronics-free feedback loop. Beyond locomotion, passive confined fluidics have been explored for sensing and morphing. For example, passive hydraulic damping and timing networks have been used to make soft actuators that respond to stimuli without electronics—e.g., a fluid-filled chamber that expands when heated, or viscoelastic fluid restrictors that delay motion to create sequential movement [86]. Overall, the Quadrant I approaches prioritises simplicity and autonomy: by entrusting control to physics (gravity, capillarity, expansion) rather than motors or circuits, they achieve extremely low power operation.

Quadrant II covers systems where a liquid is actively driven (pumped, pressurised, or otherwise forced) within a closed, self-contained circuit. A substantial portion of this quadrant comprises systems whose operating principle is based on osmosis, directly inspired by phloem and plant cell turgor. In 2014, Sinibaldi *et al*. reported a forward osmosis-based actuator, essentially an artificial plant cell, a device with two chambers separated by a semipermeable membrane; one chamber initially contained a high-concentration salt solution, the other pure water [87]. Since no pump was used, the first-generation osmotic actuator was non-reversible. Building on that, Must *et al.* achieved a breakthrough in 2019 by adding an active control mechanism to osmotic actuation [88]. They developed a reversible osmotic pump for a tendril-like soft robot using electrochemical modulation of ion concentrations. By turning the voltage on or off, the researchers mimicked the intracellular turgor control plants use, achieving movement and rigidity changes in a single device.

Aside from osmotic systems, hydraulic soft actuators form a large part of Quadrant II. Soft robotics has used fluids (typically pressurised air or liquid) to drive motion in devices like inflatable gloves and soft grippers. The typical approach is the use of miniature pumps or syringes embedded in a robot to circulate fluid into pneumatic/hydraulic chambers. Marchese *et al.* demonstrated a fully soft autonomous fish robot with its own pump and battery inside—the air-inflated and deflated tail fin actuator to propel it [89]. This work has been further extended to design a fish-like soft body to deform under hydraulic instead of pneumatic power [90]. A challenge is that conventional pumps and valves are rigid and bulky; thus, researchers explore alternatives like electrohydraulic actuators. A notable innovation here is the HASEL actuator (Hydraulically Amplified Self-healing Electrostatic Actuator) [91]. HASELs use a sealed pouch of liquid dielectric and flexible electrodes; when a high voltage is applied, the electric field forces the liquid to deform the pouch (e.g., pulling the fluid and causing the pouch to contract or bend). Essentially, HASEL actuators convert electrical energy into hydraulic pressure inside a soft container, achieving muscle-like contractions.

Quadrant III comprises systems that actively move liquids into or out of themselves, interacting with the environment in the process. This means the robot or device has some form of powered intake or expulsion of liquid. Plants, however, less frequently ingest or expel fluids rapidly on demand (animals do, e.g., squids jet water). In the plant world, there are fewer practical analogues, such as stomatal function and guttation. Thus, Quadrant III in robotics often finds inspiration in non-plant biology (like cephalopods, etc.) or simply uses engineering solutions to achieve functionality that plants don't need (such as propulsion). Even so, there is relevance to plant principles: managing moisture content and exchange is crucial in plant life (they just do it slower). Synthetic systems in this quadrant tend to pursue functions like locomotion (jetting water), environmental moisture control, or fluid-based adhesion, all requiring active flow across the boundary between the robot and the environment.

A striking example of active external liquid transport is the "squid-like" soft robot [92]. This robot actively draws water in and ejects it in pulses to propel itself, essentially performing aquatic jet propulsion analogous to a squid or octopus. The robot is mostly soft and carries its own pump and power source internally (untethered). Many other underwater soft robots are exploring similar ideas, for example, soft jellyfish robots that use diaphragms to intake and expel water in pulses [93].

Quadrant IV includes systems where liquids move into or out of the device due to environmental conditions or inherent material properties without active pumping or control input. This is perhaps the most obviously "plant-like" category since the passive fluid exchange is exactly how plants get much of their work done: xylem transpiration is a textbook example (water is drawn up and evaporated out through leaves by the passive forces of capillarity and evaporation), and many seed dispersal or actuation mechanisms in plants are powered by humidity changes in the environment (hygroscopic movements) [94]. In these systems, the environment provides the driving force—for instance, dry air provides a vapour pressure deficit that pulls water out of a plant, or conversely, moisture in the air gets absorbed by a dry seed, causing it to swell. No cellular energy is spent, yet substantial movements or fluid flows occur. Engineers are very interested in this quadrant for creating self-powered, climate-adaptive structures. The appeal is that one can harness ubiquitous sources of energy (ambient humidity, temperature gradients, etc.) to drive fluid motion, enabling functions like autonomous water uptake, evaporation-based cooling, or humidity-driven shape change.

One of the purest demonstrations of passive plant-like fluid transport is the concept of a synthetic tree for water pumping via transpiration. In 2021, Eyegheleme *et al.* created a synthetic transpiration system to aid solar-driven water purification [95]. Their setup consisted of an array of vertical tubes (analogous to xylem vessels) connected to a reservoir at the bottom and topped with a nanoporous ceramic disk that acted as a "leaf." When placed in sunlight, water would continuously wick up the tubes and evaporate from the ceramic leaf. No mechanical pump was used—the system is entirely powered by the passive energy of solar heat and the humidity gradient (dry air pulling moisture). Another rich vein of research is in hygromorphic (humidity-responsive) materials and structures directly inspired by plant organs like pine cones, wheat awns, and seed pods that change shape with moisture. For instance, Wei and Ghosh (2024) recently demonstrated *moisture-driven cellulose actuators* with programmable directional motion [96]. Another study by Choi *et al.* developed what they call "Hygromachines": humidity-powered wheels, seesaws, and even small vehicles that move autonomously in response to moisture gradients [97]. Although hygroscopic actuators are generally slow, Choi *et al.* addressed some of these limits with nanofibrous materials that have a high surface area (for fast water uptake) and directional layering (for greater force and complex motion).

In terms of integrating these passive exchanges into robotics, one challenge is that passive systems often lack an off-switch—they will respond to the environment whether you want them to or not. One solution is to combine a passive swelling mechanism with an active liquid redistribution, eventually creating an active morphing system. In summary, Quadrant IV systems exemplify *minimalist elegance*: they harness ambient gradients (humidity, temperature) to drive fluid motion and actuation without a central energy-management system, because routing is encoded locally in the structure—for example, oriented capillaries bias which regions hydrate first and by how much.

### 2.6.2 Liquid–Mediated Approaches

Plants transport fluids using a combination of passive and active mechanisms. Soft robots benefit greatly from the ability to modulate their stiffness, being compliant when gentle interaction is needed yet stiff when exerting force or maintaining shape [98]. Nature provides inspiration for such adaptability, especially from plants that achieve complex movements without muscles. Plants can reversibly tune their stiffness by adjusting internal water pressure and structural properties [25]. This plant strategy of stiffness control (e.g., turgor pressure in cells) allows branches, tendrils, and leaves to stiffen or relax on demand. Translating these plant-inspired mechanisms into synthetic materials and designs is becoming a promising route for variable stiffness soft robotic systems.

Drawing direct inspiration from plant cells, which use osmotic pressure (turgor) to achieve rigidity, synthetic systems mimic this by confining a swellable material in a flexible yet inextensible skin or compartments. By creating a concentration gradient (e.g., a salt or solute difference) between the inside and outside, water is driven into the material, increasing internal pressure and stiffness. For instance, [88] developed a "synthetic plant tissue" with encapsulated saline water content. The salt inside each pouch draws in liquid osmotically; thus, the ultimate firmness is tunable by the salt concentration and membrane permeability, balancing osmotic inflow with turgor-like pressure. Another example is the "turgor-inspired" hydrogel actuator [99–100], implemented by wrapping a hydrogel in a flexible semipermeable membrane that confines its swelling. Active stiffness modulation is achieved by using electroosmotic control (applying a low voltage to move ions), allowing water influx acceleration. This work shows how concentration gradient modulation (via osmosis or electroosmosis) in a soft material can be harnessed to switch a component from compliant to extremely rigid, echoing the plant strategy of hydraulically stiffening tissues.

Modern artificial pumps take cues from how plant cells and tissues manage fluids. For example, ion-selective membranes in plants (e.g., the root endodermis) allow water to enter while blocking most salts, akin to a reverse-osmosis filter [101]. Similarly, synthetic membranes with selective nanopores or embedded ion channels can mimic this by permitting water or specific ions to pass

and excluding others. Researchers have classified artificial ion pumps into categories based on their driving mechanism, including pumps driven by asymmetric structures, by pH gradients, by light, or by applied electric fields [102].

In plants, xylem transports water via transpiration-driven tension, while phloem moves sap through osmotic pressure differences. Inspired by these mechanisms, synthetic systems mimic plant fluid transport using similar principles or external energy inputs. Recent work has focused on biomimetic pumping methods such as electrokinetic flow [103], ion-selective membrane transport [104], electrodialysis [105], and light-driven pumps [106], each conceptually mirroring aspects of plant hydraulics. These approaches aim to replicate the efficient, self-contained pumping seen in plants, often without traditional mechanical parts, and are being applied in soft robotics, smart materials, and water filtration.

To realise plant-like, actively routed liquid redistribution in soft, porous architectures, one needs on-board mechanisms that move or reposition liquid without rigid moving parts. Field-driven pumps—electrokinetic, ion-selective/electrochemical, or photoactive—are compatible with sub-millimetre porous matrices. Accordingly, we survey representative pumping strategies relevant to variable-stiffness soft systems.

### A. Electrokinetic Pumping

Electrokinetic pumping refers to moving fluids via electric fields, typically through electroosmotic flow or electrohydrodynamic (EHD) effects. Electroosmotic pumps (EOPs) use an applied electric field to drive the liquid through capillaries or porous media by dragging the electrical double-layer of ions at solid surfaces [107]. Although both EOPs and plant xylem involve flow in narrow, surface-dominated conduits, the underlying physics are distinct: EOPs rely on field-driven interfacial slip, whereas xylem transport is generated by transpiration-induced tension and capillarity, with wettability and pit-membrane nanoporosity controlling hydraulic resistance. Unlike transpiration-driven xylem flow, electroosmotic pumps require an internal electric power source. Electrokinetic pumps provide smooth, continuous flow and scale well to microfluidic systems and can be integrated into chips for portable devices [107].

### B. Semipermeable Membranes

Plants actively transport ions across cell membranes to drive osmotic water flows—for instance, loading sugars and potassium into phloem creates an osmotic influx of water that builds pressure. Synthetic systems leverage ion-selective membranes to achieve similar fluid movement by controlling ion distribution. A prime example is forward osmosis (FO) pumping, where a semi-permeable membrane separates two solutions of different concentrations; water is drawn toward the higher concentration side, causing volume expansion [108]. This exemplifies a plant-like hydraulic actuator: high force output and energy

efficiency, but relatively slow, similar to how many plant movements (like slow tendril coiling) trade speed for power.

A challenge with purely osmotic pumps is reversibility: once the solute concentration equilibrates, the driving force dissipates. Recent innovations address this by coupling ion-selective systems with electrical control to reset gradients. Must *et al.* achieved reversible osmotic actuation in a tendril-like soft robot using electrosorption of ions on flexible electrodes [88]. Such a system directly mirrors the way plant cells modulate internal osmotic pressure (via ion pumps) to achieve reversible swelling. Although ion-selective and osmotic approaches can generate pressures and forces by leveraging chemical energy or gradients, much like plants do, purely osmotic systems tend to be slow, governed by diffusion rates through membranes; rapid motion requires additional strategies (as seen with electrosorption for speeding up response).

### C. Electrodialysis and Electrochemical Ion Pumps

Electrodialysis (ED) is a technique that uses a series of alternating cation and anion exchange membranes under an applied electric field. In essence, it is an artificial analogue of the salt-exclusion processes occurring in plant roots. Mangrove trees, for instance, achieve up to 99% salt exclusion at their roots by forcing water to pass through cell membranes and actively pumping ions out of their xylem stream [101]. The cell membranes and ion pumps in the plant root act like an electrodialysis stack at a microscale, allowing water to enter while transporting sodium and chloride ions back into the soil. Inspired by this, researchers have developed bioinspired desalination membranes and electrodialysis systems that mimic these natural ion-separation strategies [109]. In a plant-inspired context, ion exchange processes are highly selective, which is beneficial for creating filtration devices that mimic plant selectivity (such as filters that remove salt but let water through). Electrodialysis setups typically require multiple membranes and electrodes, which can increase system complexity and cost. Another limitation is clogging or degradation of the membrane if the water is not pre-filtered, much like how plant roots can be stressed by fouling or toxins in the soil. ED also requires a significant electric current flow through water, which can lead to issues like unwanted electrochemical reactions (scaling, pH changes) that must be managed.

### D. Light–Driven Ion Pumps and Photoactive Transport

Plants ultimately run on sunlight, converting light energy into chemical potential that drives many processes (including pumping ions—e.g., the $H^+$–ATPase in guard cells is activated by light to open stomata). Inspired by this, researchers have developed light-driven pumps that harness photons to move fluids or ions. Biological light-driven ion pumps (like bacteriorhodopsin or proton pumps in chloroplasts) move ions against gradients using energy from absorbed light. Analogously, artificial systems use photo-responsive materials to achieve pumping

without electrical wires. A notable advancement is the creation of membranes that generate an electric potential when illuminated, effectively acting as solar-powered pumps [110], where light alone drives ions across the membrane, much like how a plant uses sunlight to create a proton gradient in photosynthesis.

The efficiency of converting light to mechanical energy in artificial systems is currently limited. Membrane materials (carbon nitride nanotube), while effective, may not capture a large fraction of light energy compared to, say, photovoltaic devices, so the absolute flow rates or pressures achievable might be modest without strong illumination. Also, continuous operation requires continuous light input; if a shadow or darkness falls, the pumping stops (unless environmental control is preferred.

# 3. ORIGINAL APPROACH

## 3.1 Inspiration from Plant Liquid–Mediated Mechanisms

Plants harness liquid dynamics—notably the controlled distribution of free and bound water—to achieve rapid and reversible changes in stiffness and shape. In our work, we take cues from two plant mechanisms: (i) hygromorphs such as Erodium awns, where humidity-driven swelling of tilted-helical fibre architectures generates coiling, and (ii) xylem-like, anisotropic capillary networks that route liquid along preferred paths. By understanding how plants use capillary forces and osmotic gradients to adapt their mechanical properties, we can design systems that actively redistribute liquid within a porous matrix to induce controlled swelling and stiffness modulation.

Central to both plant physiology and our synthetic design is the concept of a collective porous network. In plants, an extensive vascular system enables efficient liquid transport over multiple scales. Similarly, our approach is designed to emulate this natural vascular architecture. Instead of relying on individually defined channels, the distributed porous network allows for spontaneous and collective liquid rearrangement. This collective behavior is expected to underpin the high-resolution swelling gradients, thereby offering a biomimetic route to localised compliance modulation.

At the heart of adaptive behaviour is the ability to modulate stiffness at the material level. Biological counterpart and rationale. We first analyse *Erodium cicutarium* awns: their tilted-helical cellulose architecture and anisotropic capillary network couple humidity uptake to coiling/uncoiling. In the awn, free water is routed rapidly along oriented lumens and then transitions to bound water in the wall to produce swelling; this division of roles—fast transport by free water, force generation by bound water—provides the cues for our synthetic design.

The integration of complex adaptive functions within a single system is achievable through minimal assembly, enabled by additive manufacturing techniques. To implement active liquid routing in a thin sheet, we use a laminated architecture composed of two functional layer types: an ion-permeable separator (membrane) and high-surface-area carbon films that serve as electroactive reservoirs. Using sequential spray-coating, these membrane and electrode layers are deposited to form a laminate with high integration density. This minimalistic assembly not only simplifies fabrication but also enhances the scalability and robustness of the adaptive system, qualities essential for translating bioinspired designs into practical soft robotic components.

The synthetic laminate exploits the reversible swelling of a porous polymeric matrix as a means to adjust its elastic modulus. Liquid redistribution—induced by electrokinetic processes—creates localised swelling gradients that, in turn, lead to spatial variations in compliance. This material-level modulation is critical for realizing systems that can adapt their mechanical properties on demand, mirroring the dynamic stiffness adjustments found in natural tissues.

A key innovation in our system is the employment of a non-thermal, electroactive control strategy. By utilizing low-voltage electrosorption on high-specific-surface-area carbon electrodes, the system actively pumps an electrolytic solution within the laminate. This electrohydrodynamic (EHD) process triggers precise, charge-driven liquid displacement.

The convergence of these principles—bioinspired liquid transport, collective porous architecture, additive manufacturing, and electroactive control—provides a robust platform for embodied intelligence in soft robotics. By mimicking the adaptive responses of plants, the developed synthetic systems offer enhanced compliance matching, distributed actuation, and real-time adaptability. These capabilities are especially relevant for wearable and body-interfaced applications, where safe and dynamic mechanical compliance is crucial. In essence, our work not only elucidates fundamental liquid-mediated adaptive behaviours but also bridges the gap between biological inspiration and practical robotic functionality.

## 3.2 Liquid–Mediated Systems Comparative Analysis

Expanding upon the presented state of the art, the further development of the liquid-mediated embodied intelligence concept entails not only analyzing existing mechanisms but also synthesizing systems capable of integrating key aspects of liquid transport defined earlier for both natural and synthetic systems:

- Active and passive liquid mediation distinguish flows set by environmental gradients (energy is applied externally—e.g., humidity, temperature, etc.) from flows produced from internal energy sources (e.g., electric fields, pressure, solute pumping). This maps to the passive vs active control axis.
- Liquid volume modality: By examining both transient and constant liquid volumes, one can assess the impact of temporal dynamic changes on the system's properties.

Our approach includes comparative analysis of passive liquid displacement in natural structures and actively controlled liquid displacement in synthetic systems, encompassing the following aspects:

- The dynamic interplay between free and bound liquid: Understanding how free liquid interacts with liquid bound to the material is critical for accurately describing adaptive processes.
- Impact of anisotropy: Structural features, whether uniform (isotropic) or directional (anisotropic), significantly determine the characteristics of liquid transport and, consequently, the manifestation of embodied intelligence.

Based on the duality of these aspects, structures being either isotropic or anisotropic, liquid volume being either transient or constant, etc., it is logical to consider two systems expressing embodied intelligence using opposite approaches. This

method not only allows for the isolated study of liquid transport kinetics, considering all the mentioned parameters, but also effectively negotiates the role of the liquid by accounting for the complexity of its behaviour.

In accordance with the most different systems design (MDSD) approach, selecting only two systems is a deliberate strategy to analyse the broadest spectrum of contrasting properties within minimal case studies. By deliberately choosing systems that represent the extreme ends of the studied property spectrum—one embodying active internal liquid control and constant volume (Figure 3A) and the other characterised by passive external liquid exchange and transient volume (Figure 3B)—we ensure that the fundamental differences in liquid transport dynamics are maximised. This minimalistic yet contrasting pairing simplifies the comparative analysis, enabling us to isolate and highlight the impact of each individual parameter. Furthermore, it provides a clear framework for understanding how variations in active versus passive mediation, structural anisotropy, and liquid volume modality influence the overall manifestation of liquid-mediated embodied intelligence.

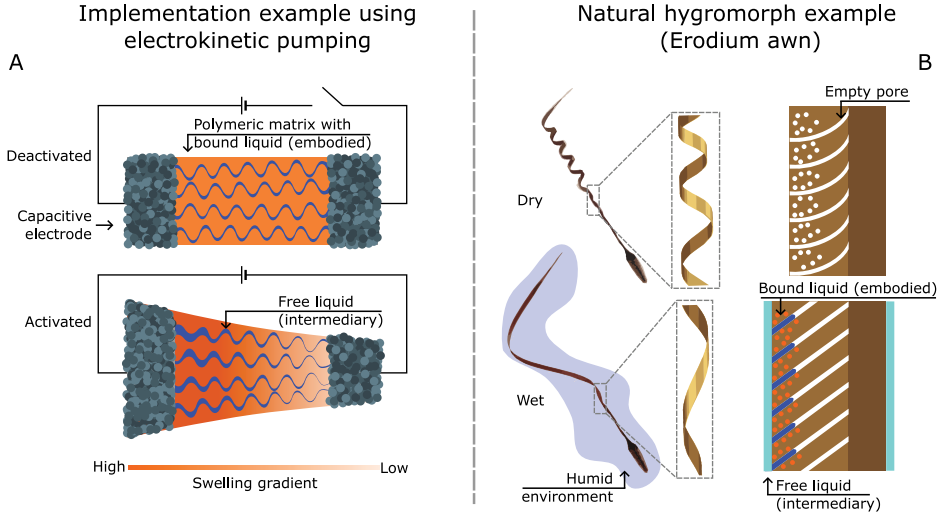


Figure 3. Case study objects. (A) a synthetic semi-swollen structure with internal swelling agent rearrangement. (B) Natural hygromorph (*Erodium* awn).

Within the framework of this work, two case studies will be presented, the comparison between which illustrates the opposite extremes of the dual-axis categorisation. The first case study, situated in Quadrant II, exemplifies active internal liquid control within a synthetic system (Figure 3A). It features a porous polymer matrix, which swells upon interaction with an electrolyte solution. An electrohydrodynamic (EHD) pumping mechanism, driven by capacitive electrodes, actively redistributes the liquid within the matrix, inducing localised swelling without exchanging liquid with the environment. This internal control parallels active liquid transport in plants. Conversely, the second case study, located in

Quadrant IV, showcases passive external liquid exchange in a natural system—the *Erodium* awn (Figure 3B). This hygromorphic structure passively absorbs moisture from the environment via capillary action, with water binding to cellulose fibres to cause swelling. Unlike the first case study system, its liquid content is transient, fluctuating with environmental humidity.

### 3.2.1 Natural Hygromorph

A natural system with passive liquid displacement and transient liquid volume that represents Quadrant IV, analysed further in this work, is the awn of *Erodium cicutarium*. This biological model is used to investigate capillary-driven water transport and the free-to-bound state transition kinetics.

In the fully dry state, the awn remains tightly coiled (Fig. 4A). Upon exposure to ambient humidity, water vapour or aerosol-phase moisture is drawn into the awn's anisotropic porous network via capillary action. Free water is initially absorbed into the capillary system and intercellular spaces, subsequently transitioning into a bound state as it is absorbed by hygroscopic tissues. This transition initiates localised swelling, which drives the uncoiling and extension of the awn (Fig. 4B).

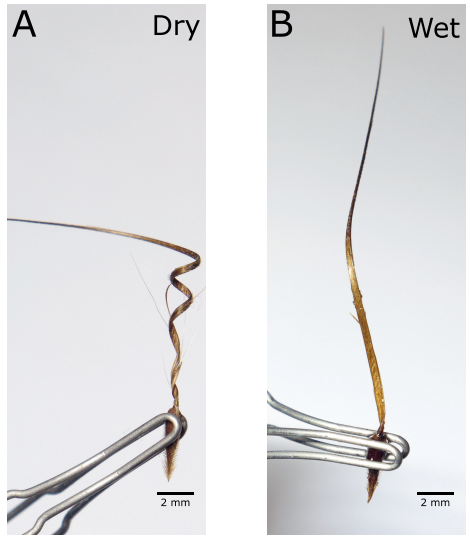


Figure 4. Hygroactuation and microstructure of *Erodium cicutarium* awns. (A) and (B) Macroscopic views of an *Erodium cicutarium* awn in dry (A) and wet (B) conditions, demonstrating the hygroscopic coiling and uncoiling behaviour.

As mentioned earlier, the efficient actuation of the *Erodium cicutarium* awn (and other similar species) relies on the high conductivity of free water within its capillary system and the pronounced hygroscopic properties of its tissues. During hydration (Fig. 5B), ambient water in the form of aerosol is absorbed by the awn's surface and enters the structure as free water via capillary action. This free water

enables rapid redistribution throughout the capillary network while gradually transitioning into bound water as it is absorbed by hygroscopic tissues, thereby inducing local swelling and modulating tissue stiffness. In the presence of water vapour alone, hydration can bypass the free water phase entirely and directly result in bound water formation, swelling the cellulose-based structure. Consequently, the total water content, comprising both free and bound fractions, increases steadily throughout the hydration process. Notably, the transition from free to bound states continues even after external hydration ceases (Fig. 5C), leading to delayed actuation driven by internal water redistribution and gradual bound water accumulation. While the total water content begins to decrease via evaporation, residual free water continues to convert into bound water, prolonging the swelling process. Eventually, once free water is fully depleted, only the bound water remains and gradually evaporates (Fig. 5D). This dynamic interplay between free and bound water provides valuable insights into the temporal aspects of swelling and liquid transport both in natural and synthetic systems.

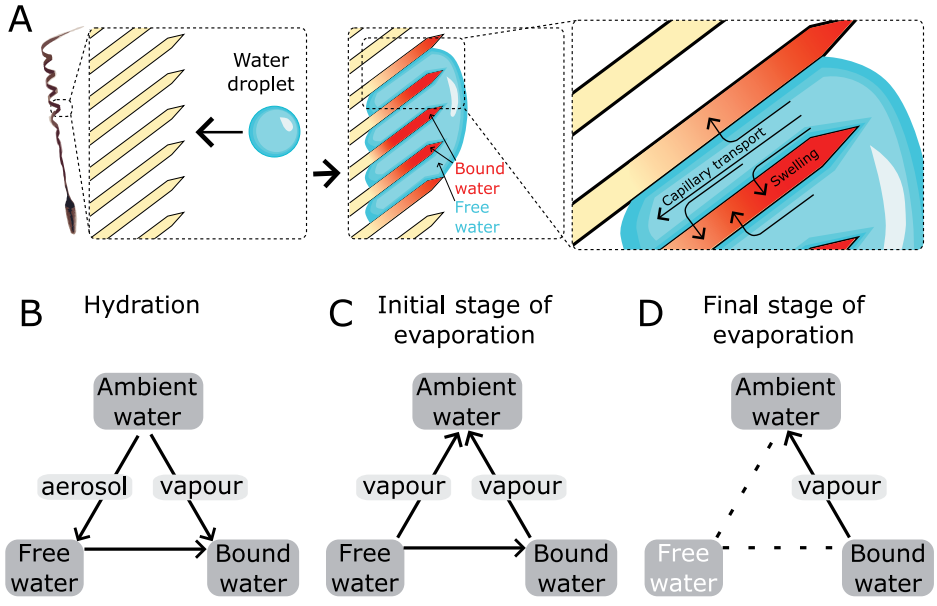


Figure 5. Schematic representation of the water absorption process (A) and dynamic interplay between free and bound water in the *Erodium* cicutarium awn during hydration (B) and initial (C) and final (D) stages of evaporation.

Such structural and functional complexity of *Erodium cicutarium* makes it a universal study model for engineered systems inspired by passive liquid-mediated actuation. Unlike synthetic structures with isotropic pore networks, this natural system demonstrates how anisotropy and hierarchical organisation optimise water transport and mechanical efficiency.

Moreover, the *Erodium cicutarium* awn allows for direct analysis of free water transport through *in situ* optical methods, such as reflectometry. As hydration

progresses, the refractive index mismatch between cellulose and the internal medium changes, altering the scattering behaviour of light. Since bound water contributes minimally to refractive index changes, the reflectometry data predominantly reflect the presence and movement of free water. When paired with mechanical measurements of swelling (indicative of bound water uptake), this dual approach enables quantification of both water states, offering a powerful methodology for studying dynamic water behaviour in porous bioinspired materials.

### 3.2.2 Synthetic System with Active Liquid Control

In contrast to passive, humidity-responsive systems found in nature, the synthetic system presented here exemplifies an actively controlled, plant-inspired strategy for internal liquid redistribution within porous structures. This study frames the device as an internally controlled hygromorph: a two-stage architecture in which an electrohydrodynamic pump first redistributes liquid and a separate swellable layer converts that redistribution into local swelling. Key design features:

- Finite liquid inventory.
- Finite pore volume—all liquid is confined to an open yet bounded porous network.
- Non-volatile working fluid—the ionic-liquid–based electrolyte remains in the pores under operating conditions.
- Reversible swelling—liquid–polymer interactions are strong enough to induce expansion, yet weak enough to deswell once the liquid is withdrawn.
- Active internal rearrangement—electrohydrodynamic (EHD) pumping shifts liquid between pores without adding or removing fluid from the system.
- Pumping only in cycling regime—liquid is displaced alternately back and forth.

Coupling spatially pumping and swelling mechanisms gives a level of reliability and tunability that passive, humidity-only hygromorphs cannot achieve, while still leaving open the possibility of dual control—combining internal pumping with external humidity cues—in future designs.

Liquid redistribution is actively controlled via an electrosorption-based EHD mechanism. Two capacitive electrodes, made from high specific surface area activated carbon, are arranged in a cross-plane configuration and separated by an insulating membrane. Upon electrical polarisation, the asymmetric interactions between cations and anions with the porous polymer matrix lead to net liquid displacement, generating a swelling gradient. This mechanism allows for low-pressure internal pumping, reducing the need for large-scale pressurisation systems typical of conventional fluidic actuators.

Pore-fill ratio (PFR), defined as the fraction of pore volume occupied by the electrolyte, emerges as a critical metric for evaluating system performance. Local increases in PFR enhance the liquid–polymer interaction, leading to site-specific volumetric expansion. In this study, the kinetics of PFR redistribution are

investigated as a function of electrical input and initial liquid content, providing insight into the responsiveness and efficiency of the system.

The electrosorption mechanism used here offers several advantages for miniaturised systems. Unlike traditional electroosmotic pumps, which may suffer from unintended Faradaic reactions (e.g., electrolysis or dendritic growth), this design uses porous, high-capacitance carbon electrodes that store charge purely in the electrical double layer [111, 112]. This ensures long-term cycling stability, essential for applications requiring repeated actuation.

The biological relevance of this electrohydrodynamic strategy is analogous rather than identical to plant-cell turgor control. In plants, ions are actively pumped across semipermeable membranes, water follows osmotically, and the resulting hydrostatic pressure changes cell stiffness. Here, electrohydrodynamically driven ion migration relocates electrolyte within an open porous laminate; the local shift in free-to-bound liquid fraction modulates swelling and compliance without producing true hydrostatic turgor. Thus, active liquid redistribution coupled to a swellable matrix can give artificial structures an adaptivity that echoes—while still differing from—the turgor-based mechanisms of living tissues. The aspect we borrow from plant turgor is the principle that controlled redistribution of liquid sets the mechanical state (stiff/soft) in space and time; the implementation—charge-driven, low-pressure liquid routing in a porous laminate—differs fundamentally from turgor.

## 3.3 Approach for Liquid–Mediated Variable Stiffness

Achieving adaptive mechanical behaviour through decentralised physical processesis a core ambition in the development of physically intelligent systems. Building on the synthetic system with active liquid control presented in the previous section, our approach leverages a multilayer laminate structure to dynamically modulate mechanical compliance through controlled liquid redistribution. This plant-inspired strategy mimics natural vascular networks, where the liquid is actively transferred between central and peripheral layers to induce local swelling gradients that adjust stiffness. Typical example provided by *Mimosa pudica,* where inner (adaxial) motor cells actively export $K^+/Cl^-$, lose water, and shrink, while the outer (abaxial) layer simultaneously imports ions, swells, and stiffens, forcing the leaf to fold or droop [113].

This approach implies a three-electrode laminate (Figure 6), where the internal (central) electrode and the two outer (surface) electrodes are arranged in a mirror-symmetric configuration. transfer of a constant volume of electrolytic solution between the central layer and the outer layers. When liquid is pumped from the centre to the outer electrodes, the polymeric matrix in the external layers swells, and its elastic modulus decreases. Conversely, liquid pumped from the outer layers back to the central electrode leads to reduced swelling in the outer layers and a relative stiffening of the composite.

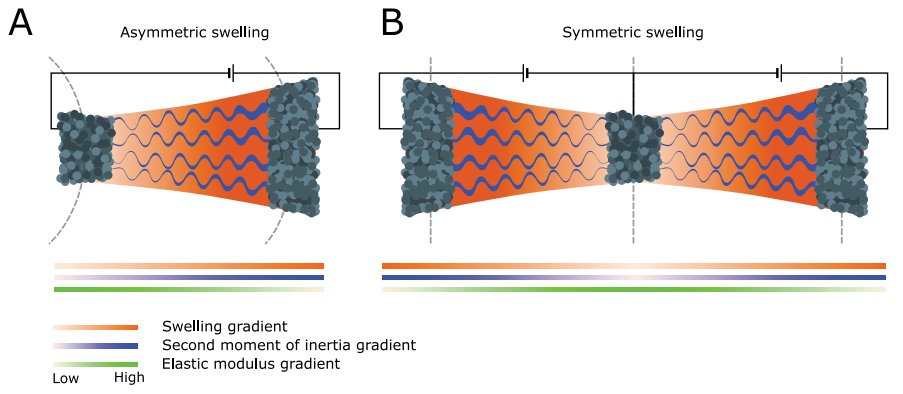


Figure 6. Unidirectional (A) and bidirectional (B) Interstitial liquid displacement modes.

This controlled liquid movement is critical because the outer electrodes, being farther from the neutral plane, contribute more significantly to the overall bending stiffness of the laminate [114]. Hence, the direction of liquid transfer directly influences the second moment of inertia and the flexural rigidity of the system. The resulting charge-driven, reciprocal liquid exchange establishes a swelling gradient across the laminate thickness, thereby enabling localised compliance modulation.

However, by varying the charge magnitude accumulated asymmetrically in external electrodes, making one surface layer thinner, we can selectively tune whether that swelling gradient produces bending actuation, geometric amplification of stiffness, or a blend of both.

- Actuation mode: Differential surface areas or offset neutral planes convert a swelling gradient into measurable curvature (Figure 6A).
- Stiffness-modulation mode: Symmetric swelling or geometric constraints suppress net bending yet alter the second moment of inertia, changing flexural rigidity without visible motion (Figure 6B).
- Hybrid mode: Intermediate configurations yield simultaneous, partial curvature and stiffness shifts.

This behaviour stems directly from our structure-defined liquid displacement approach. Unlike systems with unidirectional liquid displacement pathways (e.g., hygromorph), our three-layer open-cellular matrix constitutes a proof-of-concept multi-directional capillary system, where the system can either actuate or stiffen.

The liquid channels within the open-porous swellable matrix are not individually defined but rather behave collectively, similar to natural capillary networks in plant tissues. This collective behaviour permits spontaneous yet actively guided liquid redistribution via capillary action and electrosorption-driven pumping [115–116]. Furthermore, the spatial decoupling of the rigid pumping components (carbon electrodes) from the softer, swellable polymeric regions not only enhances the precision of liquid manipulation but also minimises mechanical compliance issues that can obscure the swelling effect [117–118].

This design is inherently plant-inspired: much like plants that modulate tissue rigidity via dynamic turgor changes, our approach exploits the reversible swelling of a polymer matrix, controlled by an internal, charge-driven liquid flow.

# 4. METHODS

## 4.1 Model Systems

### 4.1.1 Passive Natural System

**Sample Selection**

Achenes of *Erodium cicutarium* were collected near Tartu, Estonia, air-dried, and stored for several years under stable room conditions with minimal humidity cycling, without further pretreatment. Two representative awn samples were selected: one for combined hygroactuation–reflectometry measurements and the other for simultaneous light-transmission–reflectometry measurements. Each awn underwent a single complete experimental run, during which both the observation point and the applied contact force remained unchanged.

### 4.1.2 Active Synthetic System

**Two–electrode system**

The assembly of the capacitive laminate began with the preparation of two distinct formulations. First, a membrane solution was formulated by dissolving 2 g of poly(vinylidene fluoride-co-hexafluoropropylene) (PVdF-HFP) together with 2 g of [EMIM][Otf] in a solvent mixture comprising 4 ml of propylene carbonate (PC) and 40 ml of 4-methyl-2-pentanone (MP). The solution was sealed with stretch film and stirred magnetically at 70 °C for 24 hours to ensure complete homogenisation. In parallel, an electrode suspension was prepared in two steps. In the first step, solution A was made by mixing 2 g of PVdF-HFP with 24 ml of MP, while solution B was prepared by combining 1.75 g of amorphous carbon black with 2 g of [EMIM][Otf] and 10 ml of MP. Both solutions were sealed and stirred at 70 °C for 24 hours, after which solution A was added to solution B. The resulting mixture was then stirred for an additional 24 hours to achieve a uniform electrode suspension.

For the laminate assembly, a sequential spray-coating process was employed (Figure 7A–E). Initially, five layers of the membrane solution were deposited onto a plain glass substrate (Figure 7A). This was followed by the deposition of five layers of the electrode suspension over the previously applied membrane layers (Figure 7B). The resulting electrode–membrane laminate was gently detached from the glass substrate and cut into strips approximately 1 cm wide. The strips were then reattached to the glass with the membrane side facing upward (Figure 7C), and a further five layers of the electrode suspension were deposited on top (Figure 7D). Both membrane and electrode layers were applied using an airbrush held at a distance of 15 cm, with each layer sprayed for 10 seconds. After the deposition of each layer, the sample was left under direct infrared light for one minute to allow solvent evaporation and to prevent the dissolution of the underlying layers. Finally, the assembled laminate was removed from the glass substrate, and a rectangular sample was cut out for subsequent use (Figure 7E).

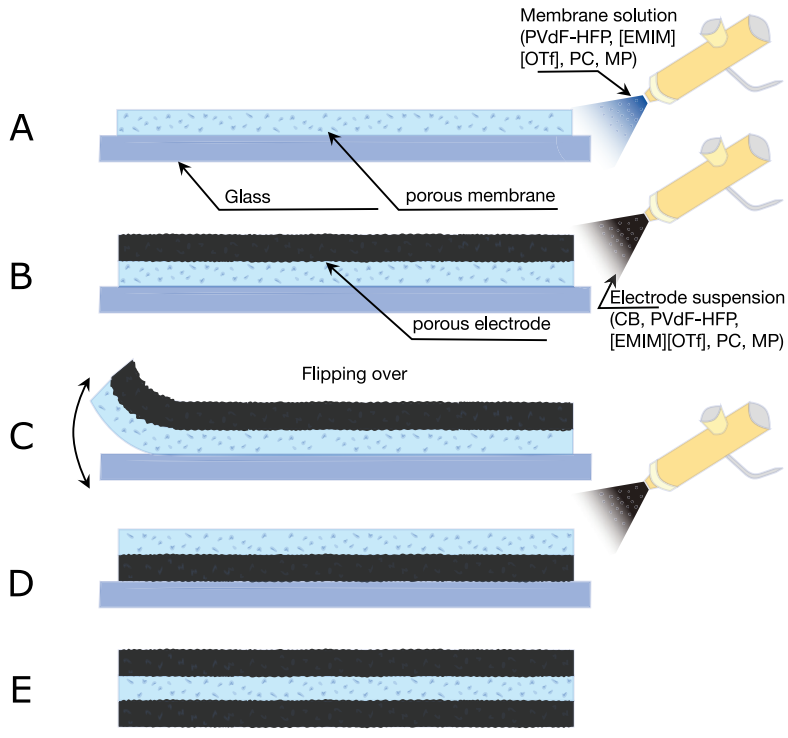


Figure 7. Two-electrode swellable liquid-mediated system assembly: deposition of membrane layer by spraying on a plain glass surface (A); deposition of the electrode layers (B); flipping over the electrode-membrane laminate (C); deposition of the electrode layers on the opposite side (D); The resulting free-standing electrode-membrane-electrode laminate (E).

### Three–electrode system

Using the prepared membrane solution and electrode suspension, a mirror-symmetric three-electrode laminate was constructed as follows. First, a thin gold current collector (approximately 100 nm thick) was cut into 4 mm wide rectangular strips and affixed—gold side up—to a glass substrate. Over this current collector, three consecutive layers of electrode suspension were spray-deposited (using an airbrush held 15 cm away for 5 s per layer) with rapid infrared-assisted drying between layers to prevent deformation. Next, six layers of membrane solution were applied over the internal electrode, forming a continuous film. Once dried, three layers of electrode suspension were deposited on top to form the first outer electrode, and the laminate was then flipped. The same sequence—membrane layer followed by three electrode layers—was repeated on the opposite side to complete the symmetric structure. Finally, outer current collectors were attached to both faces by applying a thin adhesive layer of membrane solution and affixing additional gold strips. The assembled laminate was consolidated under uniform pressure (using a rolled metal tube and a glass plate as a weight) and left to dry for at least 12 hours before being cut into 4 mm wide samples. The final laminate exhibited an overall thickness of approximately 420 µm.

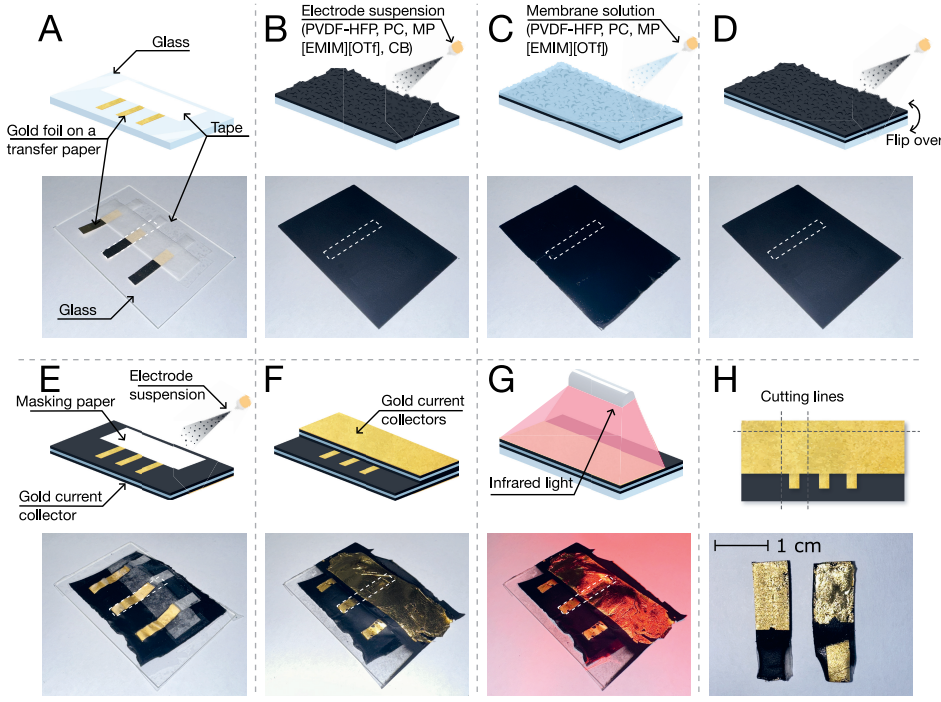


Figure 8. Three-electrode liquid-mediated variable-stiffness system assembly and corresponding photographs depicting each step of fabrication. (A) Attachment of the gold current collectors to the glass substrate. (B) Spray-deposition of electrode suspension on the gold current collector strips. (C) Spray-deposition of membrane solution on the previously deposited electrode. (D) Spray-deposition of the electrode (external) and flipping over of the electrode-membrane-electrode laminate. (E) Masking of the contact area for the internal electrode; repetition of steps C–D; spray-deposition of the second external electrode. (F) Attachment of outer current collectors to both sides of the laminate. (G) Drying under infrared light. (H) Definition of samples by cutting. White dashed rectangles indicate the location of a single sample (out of three depicted).

## 4.2 Free and bound liquid detection

To determine the kinetics of free liquid transport and the free-to-bound transition, our work employs the following methods. The transient free and bound liquid volume variations in the natural system were simultaneously assessed using optical and visual observation (hygroactuation quantisation), respectively. For synthetic systems, the local pore filling during fixed-volume liquid displacement was quantified using electrical impedance measurements, and the stiffness variation (due to corresponding swelling gradient formation) was measured via mechanical testing. The mapping of the methods used in this work to the corresponding systems is presented in Table 1.

Table 1. Mapping of methods for liquid detection

| | | Natural | Synthetic |
|---|---|---|---|
| Free liquid | Optical | ✓ | |
| | Electrical resistance | | ✓ |
| Bound liquid | Visual coiling | ✓ | |
| | Stiffness measurement | | ✓ |

### 4.2.1 Bound Water Detection

Bound water was detected indirectly by monitoring the hygroscopic actuation (Figure 9), specifically, the uncoiling of the awn, which is driven by the volumetric expansion associated with water binding in the cell walls.

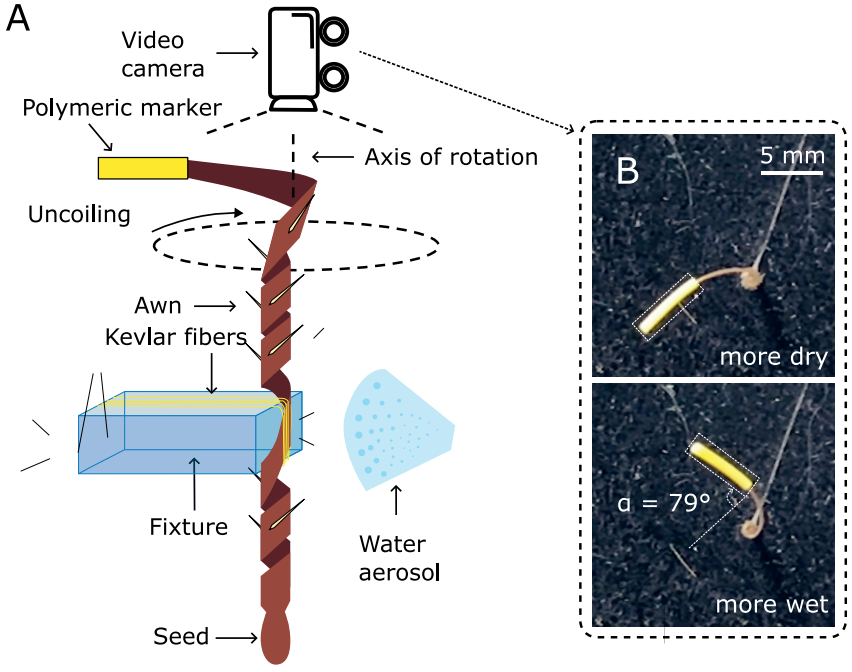


Figure 9. Schematic showing the fixation of the awn using Kevlar fibres (A). The awn is exposed to water aerosol from an ultrasonic nebuliser and a polymeric marker at the tip. A video camera tracks the marker. Representative video frames at two stages of hydration (B).

To initiate water uptake, an ultrasonic nebuliser was positioned approximately five centimetres from the awn to deliver a controlled aerosol of deionised water. An Arduino UNO controlled the nebuliser, allowing hydration cycles ranging from 10 to 45 seconds (in 5-second increments) under ambient conditions of about 45% relative humidity and 23 °C (Figure 9A).

The awn was secured using Kevlar fibre bundles to prevent any displacement during the experiment. A PVC tube (0.75 mm in diameter, 6.1 mm in length) was attached to the tip of the awn, serving as an optical marker. A video camera, positioned orthogonally to the plane of the awn's movement, recorded the uncoiling process (Figure 9B). The angular displacement of the marker was extracted from the video frames using an image recognition module implemented in National Instruments LabVIEW 21.

Since the transition of free water to bound water results in local swelling of the awn's hygroscopic tissues, the extent of uncoiling, quantified by the rotation angle, serves as a direct measure of bound water accumulation. Thus, the kinetics of the uncoiling response (including parameters such as the coiling onset time and maximum rotation angle) provided a quantitative means to infer the bound water content within the awn during hydration and subsequent drying cycles.

### 4.2.2 Free Water Detection

To monitor free water dynamics in the porous structure of *Erodium* cicutarium awns, two complementary optical approaches were developed (Figure 10A). For the reflectometry setup, two OM1 fibre-optic cables (with a core diameter of 62.5 μm) were first prepared by stripping approximately 1 cm of their cladding. The stripped ends were then aligned in parallel with a narrow gap of about 40 μm between them and fixed in place using UV-curable resin (Figure 10B). After cutting the assembly perpendicular to the fibres, the exposed surface was polished with fine-grit sandpaper to ensure a smooth, planar interface (Figure 10C). One fibre served as the emitter and was connected to a 660 nm laser source (Thorlabs S1FC660), with the power adjusted either to 0.1 mW or, when attenuated by 25 dB using a fixed optical attenuator, to 0.8 mW. The receiving fibre was linked to a spectrometer (Thorlabs CCS200), with integration times set to 2 seconds under non-attenuated conditions or 0.5 seconds when using the attenuator. The intensity of the scattered light was determined by integrating the spectral data over the 649–669 nm range. For measurements, the concave surface of the awn (located near its midsection) was brought into direct contact with the polished fibre assembly after the awn was fully uncoiled via water saturation (Figure 10D). To prevent movement during hygroscopic actuation, the awn was secured using Kevlar fibre bundles.

In the light transmission configuration, an optical fibre was similarly fixed in UV-curable resin to create a planar emitter surface. The convex side of the awn was prepared by carefully removing trichomes with a sharp blade, then pressed against the polished emitter surface and stabilised with Kevlar fibre bundles, leaving a small gap to allow transmitted light to exit unimpeded. An optical fibre ferrule was positioned roughly 4 mm from the awn, aligned parallel to the direction of light emission, to collect the transmitted signal. In this setup, the laser power was set to 1 mW and similarly attenuated by 25 dB, while the spectrometer's integration time was maintained at 0.5 seconds. The transmitted light intensity was likewise calculated by integrating over the 649–669 nm spectral range.

This dual optical approach provides real-time, noninvasive monitoring of free water uptake in the awn by exploiting changes in light scattering and transmission that occur as the refractive index contrast between the water-filled capillaries and the surrounding cellulose varies during hydration.

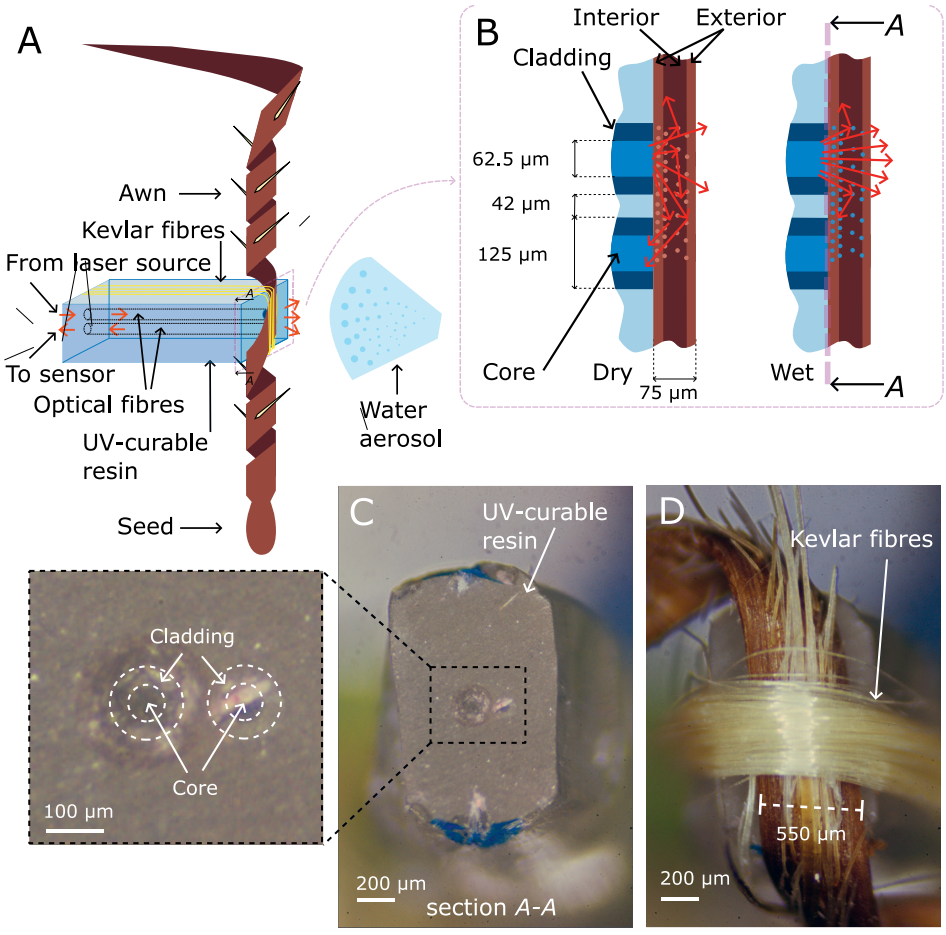


Figure 10. *Erodium* awn is fixed in place with Kevlar fibres, and the sensor registers backscattered light while the awn is exposed to water aerosol (A). Diagram comparing light scattering within the awn during dry and wet conditions (B). The surface of the optical fibre assembly (section A–A) with the cladding and core regions (C). UV adhesive fixes aligned optical fibres. The arrangement of Kevlar fibers for fixing the awn (D).

### 4.2.3 Pore Fill Ratio Quantisation

Figure 11 illustrates the test rig used to measure the kinetics of electrolytic-solution displacement. The setup employs two glass plates. The first carries a plain gold working electrode that supplies the cyclic-voltammetry (CV) excitation (Figures 11A–C). The second bears a 30 µm, gold-plated tungsten wire that serves

as the electrical resistance-sensing electrode, flanked by a plain rectangular gold electrode that delivers both the CV and impedance drive signals (Figures 11D–2F). Assembly begins by taping the gold-plated tungsten wire longitudinally onto one glass plate (Figure 11D). The wire is then spray-coated with five layers of the same membrane solution used for the capacitive-laminate fabrication. While the surface remains tacky, two thin (~100 nm) rectangular gold current collectors (Giusto Manetti Battiloro, 24 K transfer leaf) are placed parallel to the sensor wire, as schematically shown in Figure 11E. The opposing glass plate receives only a matching rectangular gold collector. The completed capacitive laminate is sandwiched between the two glass plates so that each gold collector contacts its respective carbon electrode (Figure 11G). A light, uniform load of roughly 1 N is applied to the glass plates to secure intimate contact between the gold collectors and the carbon layers.

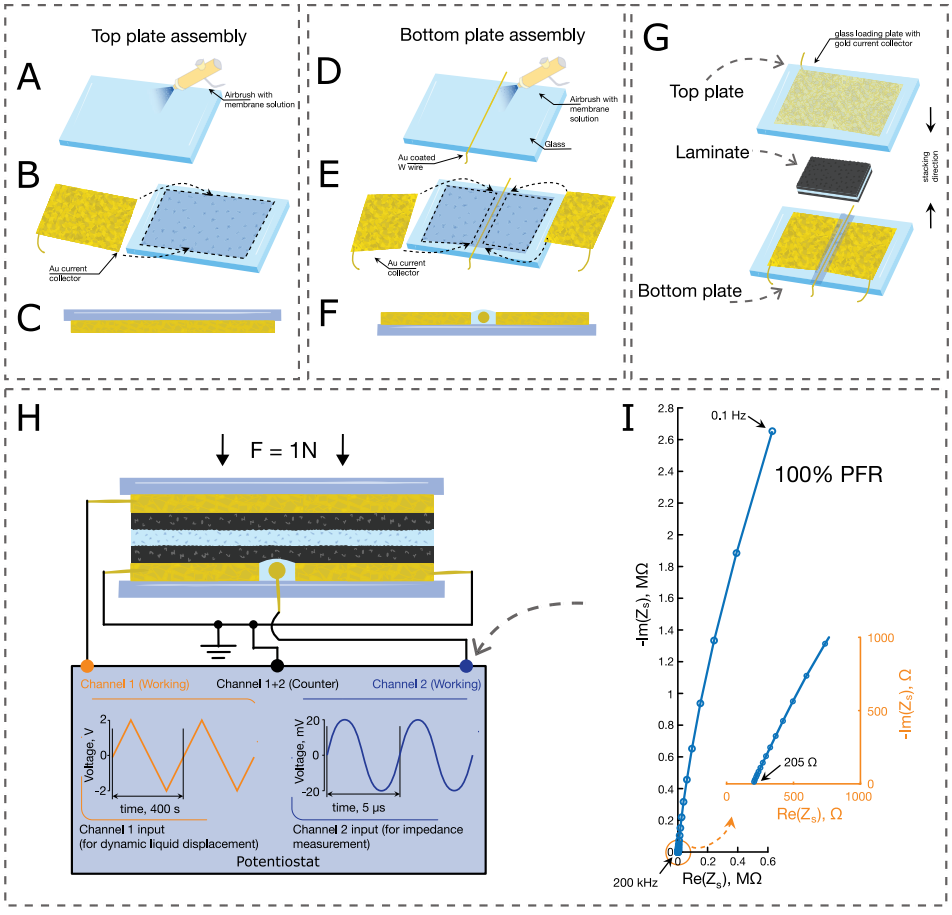


Figure 11. Experimental setup for free-liquid displacement detection. Assembly of the top plate: plain glass surface sprayed with membrane solution (A); transfer of a gold current collector (B); cross-section of a completed top plate assembly (C). Assembly of the bottom plate: a gold-plated tungsten wire attached to a glass surface and covered with

a membrane layer by spraying with membrane solution (spraying repeated 4 times) (D); transfer of gold foil current collectors onto the membrane, except 100–300 μm margin around the wire (E); cross-section of a completed bottom plate assembly (F). Assembly of the complete measurement system by stacking the laminate (G) between the top (C) and bottom (F) plates. Bipotentiostatic measurement system for simultaneous internal liquid rearrangement (by triangular input voltage) and in-situ electrolytic conductance measurement (by electrical resistance monitoring) (H). A typical spectrum of impedance (channel 2) for electrolytic conductance measurement (I).

Liquid detection was achieved by monitoring locally the conductance of the porous membrane (Figure 11H–I). A dedicated sensing region was established by integrating a small metallic (gold) electrode on one side of the laminate, separated from the adjacent carbon composite electrode by a thin membrane (11 μm). This configuration creates an electrical path where the impedance is predominantly governed by the ionic resistance of the membrane, which is directly proportional to the pore fill ratio (PFR)—that is, the volume fraction of electrolyte present in the porous structure.

During experiments, a triangular voltage waveform (e.g., ±2 V) was applied across the electrodes at various scan rates (from 5 to 50 $mVs^{-1}$). The system's response was captured (using an embedded gold-plated wire electrode and an adjacent amorphous carbon electrode) over a broad frequency range (from 200 kHz down to 0.1 Hz), with the highest frequency data used for real-time conductance monitoring. The measured conductance was normalised against the initial state to quantify dynamic variations in the liquid content.

Data processing involved using MATLAB's detrend function to separate the slowly evolving baseline, primarily due to gradual evaporation, from the rapid impedance changes induced by the applied electrical excitation. The resulting impedance fluctuations were then correlated with the dynamic displacement of the electrolytic solution, providing a highly localised and sensitive measure of liquid distribution within the porous network.

### 4.2.4 Stiffness Modulation Characterisation

Changes in bending stiffness were characterised in response to cyclic electrical stimuli (Figure 12A–B). A sample laminate was mounted in a cantilever configuration, with one end rigidly clamped and the free end subjected to controlled bending via a voice coil actuator. The actuator imposed a sinusoidal displacement, with an amplitude of approximately 0.36 mm at a distance of 9 mm from the clamped end, at a frequency of 10 Hz. A laser distance sensor continuously monitored the displacement to ensure that the actuator's performance was not compromised by the sample's stiffness.

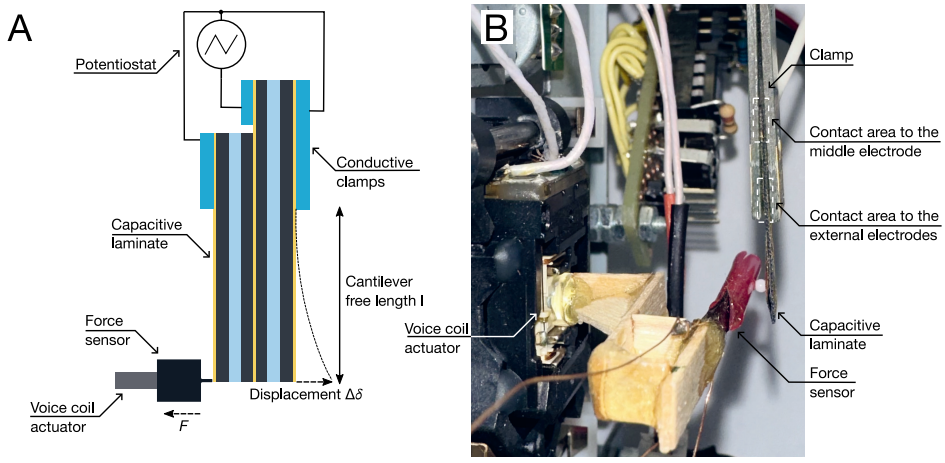


Figure 12. Schematic of the measurement setup for bending stiffness variation (A) and photograph of the experimental setup (B). A voice coil actuator deforms the free end of the laminate to a displacement $\Delta\delta$. The resulting force F is measured with a force sensor attached between the actuator and the laminate.

To accurately measure the forces generated during bending, a custom force sensor built from two 350 Ω strain gauges was positioned between the actuator and the sample. This sensor captured the dynamic load with a high signal-to-noise ratio (approximately 40), and the force data were digitised at 10 kHz using a National Instruments USB-6218 data acquisition system. The force signal was then processed in LabVIEW using a fast Fourier transform (FFT) to extract the amplitude of the periodic load.

Bending stiffness (EI) was calculated using the Euler–Bernoulli beam theory according to equation (1):

$$EI = \frac{Fl}{3\delta} \tag{1}$$

where $F$ is the measured force at the free end, $l$ is the effective beam length, and $\delta$ is the maximum deflection observed.

The observed stiffness modulation directly correlated with the internal rearrangement of the liquid medium.

# 5. RESULTS ON DYNAMIC INTERPLAY OF LIQUID STATES, STRUCTURE, AND MATERIALS

This section aims to present the results from two complementary study cases (Publications II, III and IV) exploring liquid dynamics in two contrasting systems and emphasizing how the interplay of free and bound liquid phases underpins embodied intelligence, particularly:

- 5.1 Natural, passive hygromorphic system (*Erodium* awn): morphology and anisotropy were quantified by SEM; free water in oriented capillaries was tracked via fibre-optic reflectometry (transmission/backscatter); bound-water swelling was read out from hygroactuation; kinetic and mechanical metrics—*FWHM* of optical peaks, capillary depletion times $t_D$, coiling onset $t_{coil}$, and rotation extent $\Delta\alpha_R$—were extracted, and their dependence on hydration time and structure was mapped (Publication II).
- 5.2 Synthetic, active hygromorphic system (electrokinetic laminate): microstructure was characterised; liquid-redistribution efficiency under electrosorption-based pumping was measured; local pore-fill ratio via in-situ impedance was mapped; stiffness modulation with a standardised bending test was quantified, while responses were related to electrical input and initial PFR (Publications III and IV).

## 5.1 Passive Transient Liquid Volume Displacement in Natural Anisotropic Structures

### 5.1.1 Morphological and Structural Characterisation

Scanning electron microscopy (SEM) investigations of the *Erodium* cicutarium awn reveal a highly anisotropic and multilayered architecture (Figure 13). The awn displays a rectangular cross-section with a high length-to-width ratio (approximately 7:1) and an overall thickness on the order of 75 μm. The external surface of the awn is patterned by numerous longitudinal ridges that run parallel to the internal capillaries. These ridges form distinct, evenly spaced lines that coincide with the direction of the underlying channels, effectively guiding water along the awn's axis. The surface of the awn is covered with trichomes (Figure 13A–B). Each trichome exhibits a similar surface pattern—parallel micro-ridges with a smaller spacing than those on the awn's epidermis, further amplifying the effective surface roughness. Cross-sections through individual trichomes reveal a honeycomb-like internal structure, indicating that capillary pathways extend not only along the awn but also into these protruding trichomes (Figure 13C). Within this thin structure, aligned capillary channels run longitudinally, providing pathways for water to be quickly drawn in by capillary action.

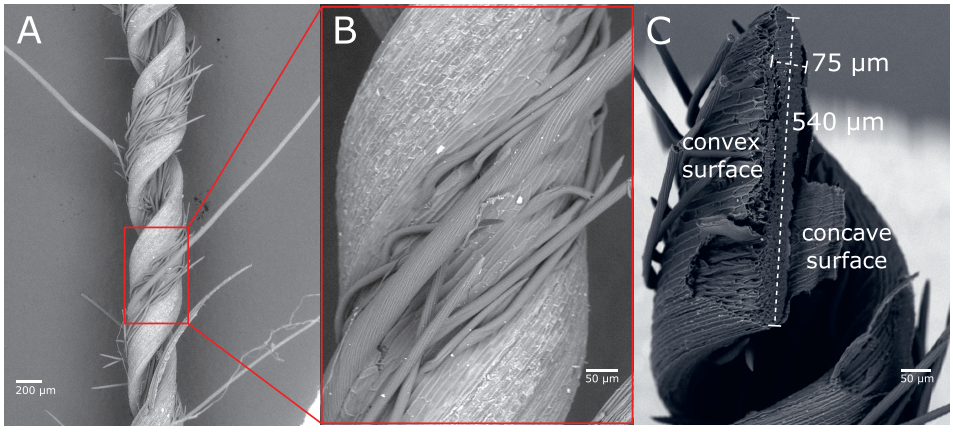


Figure 13. Scanning electron microscope (SEM) images of the helical arrangement of cellulose fibres in the dry *Eridium* awn, also showing trichomes (A, B). Cross-sectional SEM image reveals the internal capillary network of the awn, highlighting the concave and convex surfaces with measurements of the thickness and structure (C).

### 5.1.2 Optical analysis

Reflectometry was used to assess the intensity of light scattered by the awn's internal capillary network, therefore tracking free water displacement kinetics. The temporal evolution of the uncoiling angle, recorded alongside the optical signals, provides a kinetic measure of the free-to-bound water transition. By tracking changes in light scattering and transmission, in conjunction with the uncoiling kinetics of the awn, we obtain real-time insights into free water uptake and its subsequent redistribution and transition into a bound state (Figure 14). The synchronous decrease in reflectometry signals and the corresponding increase in transmission (as illustrated in the key transient courses in Figures 14B and 14C) validate the reliability of these methods for tracking free water dynamics. Key response curves (Figure 14) are used further to quantify parameters associated with bound and free water interplay and are critical for understanding the rapid water uptake during hydration and the slower evaporation during drying.

### 5.1.3 Parametrisation of Water Dynamics

A central aspect of this analysis is the extraction of quantitative parameters from the optical and hygroactuation data (Figure 14A–C). These parameters allow us to characterise in detail the water dynamics within the *Erodium* awn, providing insights into the transition from free to bound water and its direct influence on the swelling behaviour of the structure.

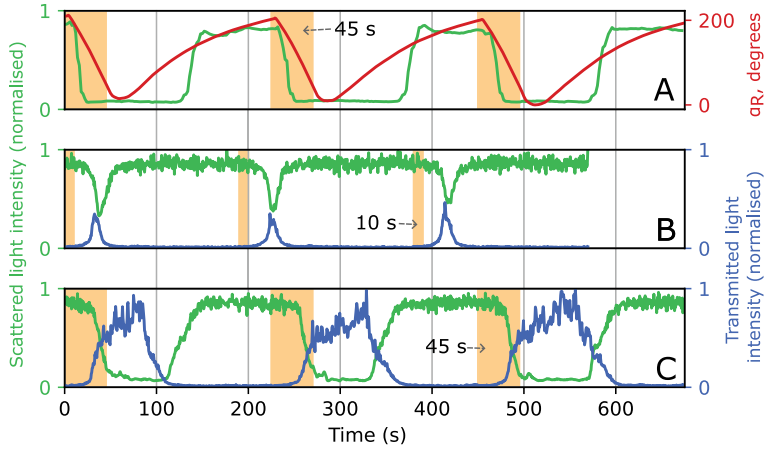


Figure 14. Normalised backscattered light intensity (green) and angular rotation ($\alpha_R$, red) of the awn over time for hydration periods of 45 s (A). Simultaneous measurement of backscattered (green) and ballistically transmitted (blue) light intensities for 10 s (B) and 45 s (C) hydration periods (B, C). The hydration period is depicted as an orange area.

One key parameter is the Full Width at Half Maximum (*FWHM*), which is measured for both scattered ($FWHM^S$) and transmitted light ($FWHM^T$) peaks during hydration (Figures 15A–B and 16C). The *FWHM* quantifies the time span over which the local free-water signal remains above half of its maximum and thus is a kinetic measure: it is the interval between the half-maximum crossings on the rising and falling limbs of the peak. The leading half-maximum crossing reports the uptake rate (capillary front propagation), whereas the trailing half-maximum crossing reports the depletion rate (evaporation plus free-to-bound conversion) at the observation site.

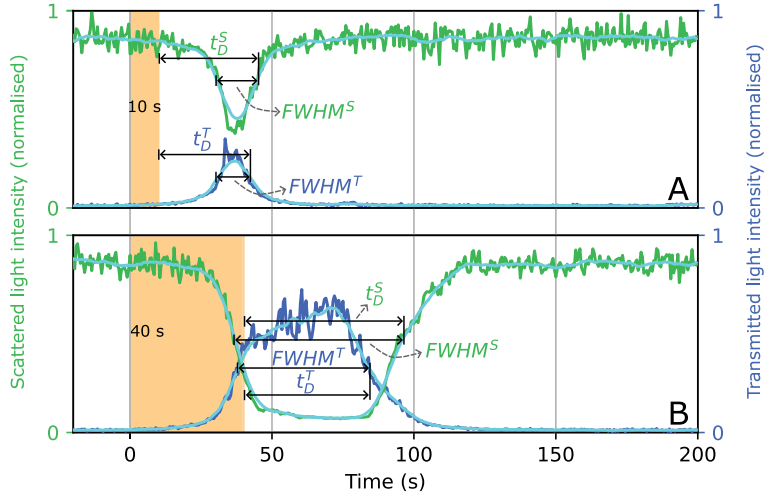


Figure 15. Definitions for kinetic parameters related to free water content. Definition of capillary depletion period ($t_D{}^T$ and $t_D{}^S$) and full width at half maximum ($FWHM^T$ and $FWHM^S$) for ballistically transmitted and backscattered light intensities, respectively, for hydration periods of 10 (A) and 45 (B) seconds. The cyan line represents the simple moving average (SMA), calculated using a 20-point moving average window.

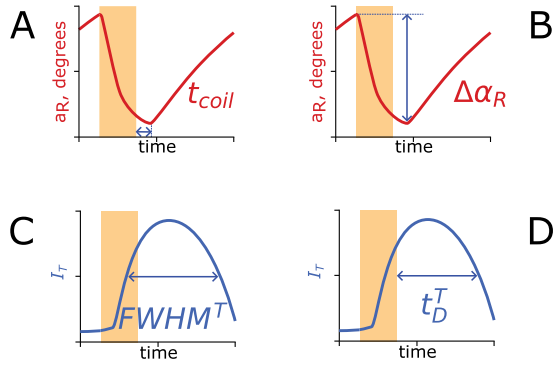


Figure 16. Kinetic parameters definition. Coiling onset time $t_{coil}$ (A), extent of uncoiling $\Delta\alpha_R$ (B), Full Width Half Maximum $FWHM$ (C), capillary depletion time $t_D{}^T$ (D).

Another parameter is the capillary depletion time, denoted as $t_D{}^T$ for transmitted light and $t_D{}^S$ for scattered light (Figure 15A–B and 16D). This is defined as the time elapsed from the end of hydration until the light intensity falls below 50% of its peak value. These depletion times quantify how quickly free water is either evaporated or transitions into the bound state. A larger $t_D$ indicates slower local depletion (greater persistence of free water after hydration stops), whereas a smaller $t_D$ indicates faster depletion. Consistent with the presented data, $t_D$ increases with hydration duration $t_H$ because a longer exposure leaves more free water to be depleted.

The coiling onset time ($t_{coil}$) represents the delay between the initiation of hydration and the observable onset of the uncoiling (or swelling) response (Figure 16A). This time marks a period in which the bound and free water evaporation starts to dominate over the free-to-bound water transition.

The extent of bound water accumulation is gauged as the difference between the awn's maximum rotational angle before and minimum rotational angle after hydration, $\Delta\alpha_R$ (Figure 16B).

Together, these parameters collectively characterise the dynamic interplay between free and bound water. During hydration, free water rapidly enters the capillary network. $FWHM$ ($FWHM^S$, $FWHM^T$) is used as the residence-time of local free water—the interval between the half-maximum crossings of the optical peak; the rising crossing reflects uptake (capillary front arrival), and the trailing crossing reflects depletion (evaporation and free-to-bound conversion). Capillary depletion time ($t_D{}^T$, $t_D{}^S$) is the post-hydration depletion time from hydration stop to 50% signal, i.e., how long free water persists locally after inflow ceases (larger $t_D$ indicates slower capillary depletion). Coiling onset time ($t_{coil}$) is the time to the global maximum of $\alpha_R$ (onset of recoiling), marking when evaporation-dominated kinetics overtake free-to-bound conversion. Together with $\Delta\alpha_R$ (uncoiling extent, a proxy for bound-water accumulation), these metrics separate uptake, persistence, and the evaporation-driven reversal of swelling.

### 5.1.4 Kinetic Analysis and Swelling Behavior

Immediately following hydration, the awn continues to uncoil as three simultaneous processes, each governed by distinct kinetics, proceed: (i) the conversion of free water to a bound state, (ii) the direct evaporation of free water, and (iii) the evaporation of bound water (Figure 17). At $t_{coil,}$ the volumes of free and total water attain their maxima, overall swelling begins to diminish, and the awn reverts toward its dry, coiled configuration. Figure 17A shows that $t_{coil}$ depends only weakly on hydration duration, spanning roughly 5–12 s for hydration periods of 10–60 s. In the presented data, $t_{coil}$ varies weakly with hydration duration, consistent with a finite capillary volume and rapid post-hydration depletion of free water.

When liquid water is supplied to the awn surface—e.g., by aerosol deposition—it infiltrates the capillary network via capillary forces while concurrently being absorbed by the hygroscopic capillary walls. The minimum observed $t_{coil}$ of approximately 5 s characterises the system-specific minimal time interval over which the kinetics of the free-to-bound conversion become equal to the kinetics of free-water evaporation, thereby setting the minimum duration of a single hygroactuation cycle. With greater hydration, free water penetrates deeper, wetting previously dry regions; because the interaction volume expands linearly, the resulting increase in $t_{coil}$ is sub-proportional. The reproducible uncoiling interval, therefore, reflects an intrinsic design constraint for natural and engineered systems that exploit free water as an actuation medium: the hygro-actuation cycle cannot be faster than the time required to convert free water into its bound form.

Owing to the high-flux aerosol delivered during the hydration interval $t_H$ and constant rate propagation of the hydrophilic frontline (as the unhydrated cellulose is initially hydrophobic and increases its hydrophilicity upon wetting [16]), the mass of free water taken up by the awn scales linearly with $t_H$. In contrast, the dependence of the rotation angle $\Delta\alpha_R$ on $t_H$ (Figure 17B) is non-linear, implying that the quantity of bound water increases exponentially with time, even though the overall water input remains proportional. Upon contacting the awn surface, aerosol water first accumulates as free water and simultaneously binds to hygroscopic walls; after hydration stops, uncoiling persists only while free-to-bound conversion outpaces evaporation. With longer $t_H$, the wetted region penetrates deeper along the anisotropic capillaries, so the interaction volume grows, whereas the local free-water content at a given site is lower; consequently, the reservoir that must be converted/evaporated after $t_H$ grows less than proportionally. This produces a sublinear increase of $t_{coil}$ with $t_H$ (e.g., 6–7 s at $t_H$=10 s vs. 11–12 s at $t_H$=60 s) and makes each additional second of hydration contribute progressively less to $\Delta\alpha_R$. Two additional factors reinforce this concavity: (i) progressive occupation of binding sites as the front advances (hydrophobic to hydrophilic transition of vessels), and (ii) water-induced plasticisation of tissues that reduces stiffness, giving outer layers (with greater mechanical leverage) a disproportionate early contribution to bending; both lead to rapid early uncoiling followed by slowing as capacity is approached.

Figure 17C reveals that both $FWHM^T$ and $FWHM^S$ grow exponentially with the hydration time ($t_H$). The observed exponential increases in $FWHM^T$ and $FWHM^S$ also imply that the duration of the capillary depletion phase, which follows hydration, increases correspondingly. After the hydration stop, free water does not vanish immediately; it redistributes along the anisotropic capillary network and is then removed by evaporation or by conversion to the bound state. As $t_H$ increases, the wetted length of the capillary system increases, so the path filled with free water is longer; consequently, backflow becomes transport-limited and persists longer, which broadens both $FWHM$ ($FWHM^T$ and $FWHM^S$). Because pore hydrophilicity increases during hydration [16], the moving interface between dry and wetted pores governs hygro-actuation. This hydration front advances more slowly than water motion within already-filled pores, and evaporation is at a lower rate than both the aerosol-driven uptake during hydration and the intra-capillary redistribution, so an exponential increase of $t_D$ with respect to $t_H$ is expected.

Figure 17D reveals a characteristic latency between hydration stop and the detection of free water depletion, dictated by water transport through the capillary network. In Figure 17D, both $t_D{}^T$ and $t_D{}^S$ exhibit the same exponential dependence observed for $FWHM^T$ and $FWHM^S$; however, $t_D{}^T$ and $t_D{}^S$ are shifted by an offset of approximately 30 s. This temporal offset represents the time required for liquid to traverse the capillaries and is expected to vary with capillary length, geometry, and anisotropy. Consequently, the hygroactuation cycle cannot proceed more rapidly than this transport interval, a limitation also reflected in the coiling onset time ($t_{coil}$). Because the measurement site was partially occluded—thereby suppressing local evaporation—free water is anticipated to retain longer there until it is displaced, evaporates, or converts progressively into bound water.

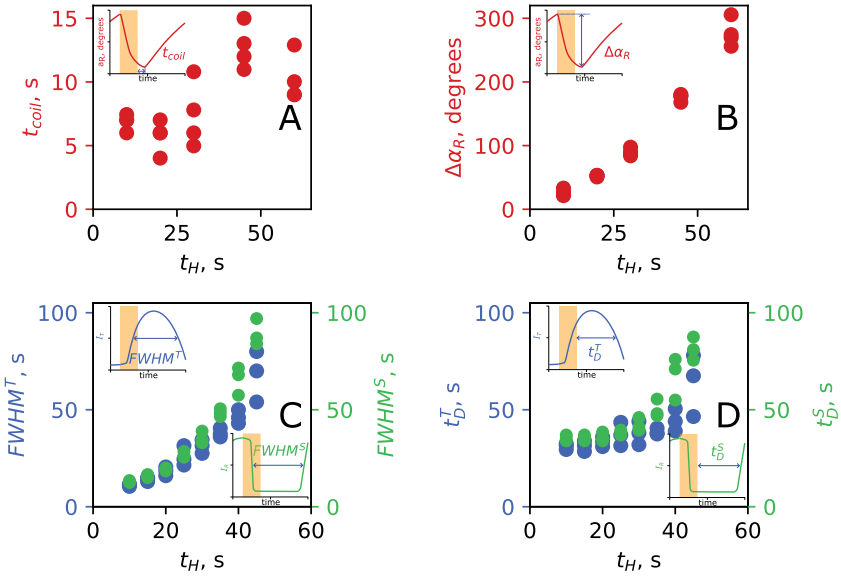


Figure 17. Coiling onset time $t_{coil}$ (A). Rotation angle $\Delta\alpha R$ (B). $FWHM$ of light intensity peaks in scattering and transmission modes (C). Capillary depletion time $t_D$ in scattering and transmission modes (D).

## 5.2 Active Constant Liquid Volume Displacement in Synthetic Isotropic Structures

### 5.2.1 Morphological and Structural Characterisation

In a two-electrode system, scanning electron microscopy (SEM) revealed several key features of the polymeric membrane and the electrode composite. The SEM images showed that the membrane, which separates the metal wire electrode from the carbon composite electrode, has an overall thickness of about 20 micrometers (Figure 18A); however, the thickness of the membrane at the critical spot, dividing the metal wire and the composite electrode, was further reduced to 11 µm. This very thin membrane is essential for ensuring that the impedance measurement is highly localised.

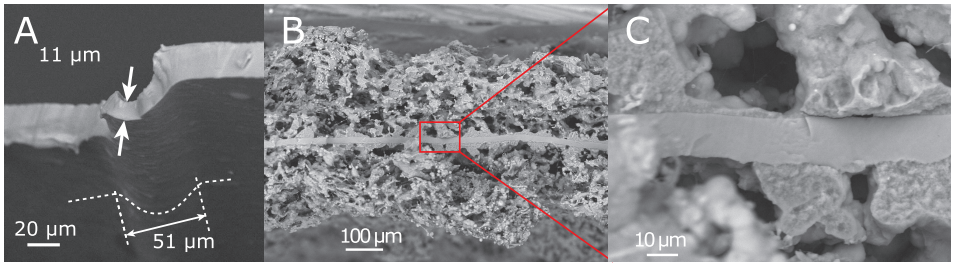


Figure 18. SEM micrographs of the PFR assessment membrane cross-section with a negative impression of the wire electrode (A), composite electrode (B); cross-section of the laminate (C); zoom-in to the membrane cross-section (F).

In addition to the membrane, the carbon composite electrode exhibits a hierarchical porosity. The largest pores in the electrode reach up to 50 micrometres in diameter, and the composite electrode itself is roughly 200 micrometres thick (Figure 18B). The membrane separating the two electrodes is much thinner, around 20 micrometres, and appears smooth and continuous, with no macropores present (Figure 18C). This absence of macropores is particularly important because it allows a pressure gradient to develop across the laminate, which is crucial for effective liquid transport and the formation of a swelling gradient.

These structural features have a significant impact on liquid transport and swelling behaviour. The thin polymeric membrane confines the electrolyte within a very localised region, which improves the sensitivity of the impedance-based measurements used to determine the pore fill ratio. Furthermore, the hierarchical porosity of the electrode provides an optimal balance between swelling magnitude and the rate of liquid displacement. The presence of larger pores facilitates rapid electrolyte movement, while the overall porous structure ensures that capillary forces can drive effective liquid redistribution.

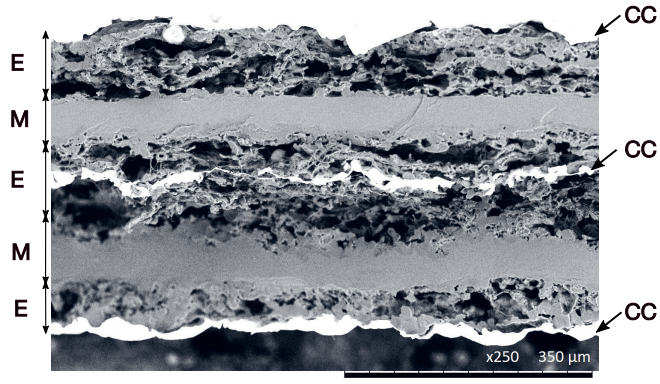


Figure 19. Scanning electron microscopy image of the cross-section of a three-electrode liquid-mediated system. E—electrode, M—membrane, CC—current collector.

The three-electrode synthetic laminate is designed with a mirror-symmetric architecture for achieving high-resolution, charge-driven stiffness modulation (Figure 19). A carbon-free membrane layer, approximately 70 micrometers thick, is alternated with electrode layers. The central electrode is about 120 micrometers thick, while the two outer electrodes together measure around 135 micrometers in thickness. This mirror-symmetric assembly not only ensures balanced charge distribution and structural stability but also enables reversible swelling gradients at a resolution of roughly 200 micrometers. Such control is essential for modulating stiffness without causing significant geometric deformation.

Scanning electron microscopy (SEM) was used to examine the microstructural characteristics of the laminate. The SEM images clearly show a distinct contrast between the membrane and electrode layers. The membrane layer exhibits a smooth, almost featureless surface, which indicates a uniform spray-deposition process that is critical for maintaining consistent liquid transport properties. On the other hand, the electrode layers display a rougher hierarchical porous structure. This results in a broad pore size distribution, with the largest pores reaching up to ~50 µm in diameter (Figure 18B). The presence of these pores is vital, as it facilitates efficient electrohydrodynamic pumping by allowing rapid liquid equilibration and capillary-driven redistribution of the electrolyte.

Overall, the combination of the mirror-symmetric structural design and the optimised microstructure supports localised and reversible swelling. This enables modulation of stiffness, which is promising for applications in wearable technology and bioinspired soft robotics.

### 5.2.2 Liquid Redistribution Efficiency

Impedance is highly sensitive to changes in the electrolyte content within the probed pores because the ionic conductance through the membrane scales with the local electrolyte volume fraction and the short current path (approximately 11–20 µm in our geometry). The thin membrane, therefore, enhances spatial

localisation, while its near-uniform porosity ensures a consistent conductance–PFR mapping across the probed area (Figure 18). In this configuration, the carbon composite adds only a minor series contribution relative to the ionic term, so the measured impedance primarily reflects the local pore-fill ratio (PFR). The contribution of the carbon composite electrode to the overall impedance is minor compared to the effect of the electrolyte filling the polymer network, so the measured impedance primarily reflects the local pore fill ratio. Variations in the membrane's electrolytic conductance are therefore adopted as a proxy for the transient PFR level, with the explicit recognition that simultaneous changes in electrolyte concentration also modulate the measured conductance.

Theoretical studies of ionic-liquid solutions have shown that ions acquire solvation shells and possess unequal mobilities [119]. Because cations typically migrate more rapidly, solution transport is more pronounced toward the electrode under negative polarisation than under positive polarisation. Concurrently, solvent molecules diffuse to mitigate ionic concentration gradients and restore uniformity.

Electrohydrodynamic (EHD) pumping in the device arises from capacitive charging of the two-electrode laminate: an imposed current drives ions to the electrodes, compensating the electronic charge. Cyclic-voltammetry traces of the charging transient (Figures 20A and 20B) confirm high electrochemical stability and reversibility. The voltammograms exhibit negligible faradaic currents, indicating an absence of unintended redox processes apart from a minor contribution from the electrolysis of trace water absorbed by hygroscopic constituents.

By calibrating the resistance values against known electrolyte concentrations, we can determine the degree of pore filling. In other words, as the electrolyte fills or empties the pores, the resistance changes in a predictable way, allowing us to directly relate these changes to the pore fill ratio. This approach ensures that the PFR is assessed in a very localised region, thanks to the thinness of the polymeric membrane, making the method both sensitive and accurate for evaluating internal liquid redistribution in the system.

The dynamic behavior of the porous membrane is monitored via resistance measurements during cyclic excitation using a triangular voltage waveform (the scan rate was from 5 $mVs^{-1}$ to 50 $mVs^{-1}$ and over a voltage sweep range from ±1 V to ±2 V, as indicated in Figures 20A and 20B, respectively). The results indicate that two interdependent mechanisms drive the observed conductance variations (and thus PFR locally): a rapid electrokinetic transfer, predominantly governed by the field-driven migration of ions, and a slower diffusive solvent redistribution that smooths out concentration gradients over time.

The kinetics of PFR variation were analysed in a (nearly) constant total amount of working fluid (i.e., the electrolyte solution) at different ranges of applied voltages and scanning rates. A small (approximately 4.5% per hour) linear trend $Z_0(Zs)$ was separated for analysis.

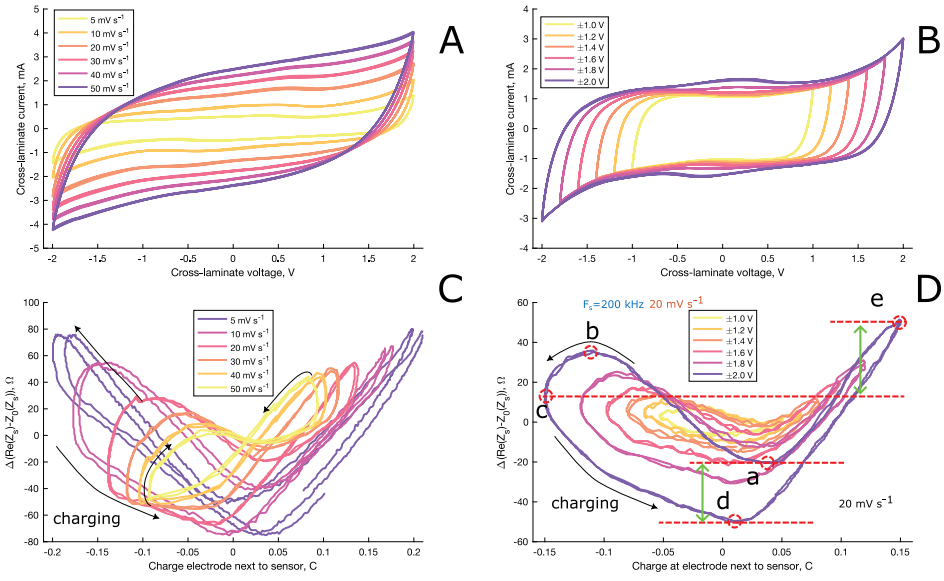


Figure 20. Cross-laminate cyclic voltammetry of the capacitive laminate at scan rates from 5 mV $s^{-1}$ to 50 mV $s^{-1}$ (A). Cross-laminate cyclic voltammetry of capacitive laminate at voltage ranges from ±1 V to ±2 V (B). Dynamic variation of $Re(Z_s)$ with respect to cross-laminate charge at 5 $mVs^{-1}$–50 $mVs^{-1}$ scan rate (C) and ±1 V to ±2 V voltage range (D).

Figures 20C and 20D present the cyclic variation of membrane resistance, expressed as $\Delta Re(Z_S)—Z_0(Z_S)$, as a function of the accumulated charge for different potential-scan rates and voltage windows, respectively. In line with our model of bulk electrolyte displacement, pore filling is not spatially uniform; rather, liquid advances preferentially along the direction of motion while trailing regions empty, thereby establishing a PFR gradient across the membrane. At the higher scan rate of 50 $mVs^{-1}$ (Figure 20C), the conductance response is markedly asymmetric: it rises under negative polarisation, reflecting an influx of electrolyte that increases PFR, and falls under positive polarisation. The extent of this asymmetry is captured by the broad hysteresis loop in the conductance–charge plot. When the laminate is cycled at a lower scan rate of 5 $mVs^{-1}$, the charge–discharge trajectory exhibits nearly identical slopes for positive and negative polarisation, and the hysteresis width contracts to about 10–20 Ω. Under these conditions, diffusive solvent redistribution outruns electrokinetically driven bulk displacement. Accordingly, the magnitude of conductance change observed at varying scan rates arises from two coupled processes—electrokinetic ion transfer and diffusive solvent relocation—whose relative contributions depend on the scan rate. This dual-mechanism behaviour offers an instructive analogue for the hypothesised solvent-redistribution dynamics in tree stems.

Figure 20D illustrates the dependence of membrane conductance on the applied voltage window (1–2 V) at a fixed scan rate of 20 $mVs^{-1}$—a regime in which both electrokinetic pumping (bulk electrolyte displacement) and diffusive

solvent redistribution act simultaneously. This intermediate scan rate was deliberately chosen to prevent either mechanism from dominating and thus to isolate the influence of voltage amplitude. As the voltage window is widened, the charge stored on the electrode interfaces increases proportionally, and with it, the volume of electrolyte displaced, a relationship clearly reflected in the conductance trends of Figure 20D.

Characteristic points ‘a’–‘e’ in Figure 20D, obtained under a ±2 V window, display a pronounced polarity dependence. In the first half-cycle, the impedance measured at positive bias is approximately 30 Ω higher than at the corresponding negative-bias point (‘a’ vs ‘d’), signifying a lower PFR and thus confirming that negative polarisation fills pores with electrolyte, whereas positive polarisation empties them. The same trend is observed at the extrema of accumulated charge: at points ‘c’ (maximum negative charge) and ‘e’ (maximum positive charge), the impedance at positive bias exceeds that at negative bias by 38 Ω. Even so, at the chosen scan rate of 20 $mVs^{-1}$, the total impedance excursion remains moderate—2.1% of $Z_0(Z_S)$ for the ‘a’–‘d’ segment and 2.5% for the ‘c’–‘e’ segment.

### 5.2.3 Accessing local PFR value

In the next experiment, we evaluated the pumping efficiency—i.e., the capacity for bulk electrolyte displacement—as a function of the absolute pore-filling ratio (PFR). To generate a controllable reduction in the total volume of electrohydrodynamic (EHD) working fluid, we relied on the evaporation of the volatile co-solvent methyl propionate (MP; vapour pressure is 2.1 kPa). Only the laminate edges were exposed to ambient air, while glass plates sealed the major faces, so solvent loss occurred exclusively through the edges. This restricted geometry slowed evaporation enough to permit continuous, *in situ* tracking of the dynamic PFR as the inventory of mobile liquid gradually diminished. Freshly prepared specimens are defined as having a PFR of 100%; thereafter, evaporation of MP decreases the PFR monotonically toward its minimum, at which point only the non-volatile solvent and the dissolved electrolyte remain.

A linear relationship was assumed between the pore-filling ratio (PFR) and the membrane’s electrolytic conductance. The lower bound of PFR was established by interpolating between the conductance of a fully saturated membrane (defined as 100% PFR) and that of a completely dry scaffold (0% PFR). To verify the 0% condition, a separate specimen was exhaustively leached with neat methyl propionate (MP) to remove all electrolyte. This treated sample exhibited a resistance exceeding 50 kΩ, substantially higher than the values recorded during the dynamic PFR measurements, confirming that the working fluid remains mobile and that ions show little affinity for the polymer matrix.

When the porous network is fully saturated (PFR = 100%), electrolyte displacement is kinetically favourable, yet it fails to generate a meaningful swelling gradient: although PFR diminishes near the source (positively biased) electrode, no vacant pores exist at the sink (negatively biased) electrode to be filled. At the opposite extreme, excessive drying raises the membrane’s resistance, hindering

electrolyte transport and lowering both energy efficiency and transfer rate. Accordingly, the pumping effect—quantified by the dynamic variation in PFR—is expected to reach a maximum at an intermediate, optimal level of mobile liquid within the porous structure.

Figure 21A displays the time-resolved evolution of electrolytic conductance, $G_S$ (the real component of the susceptance), and electrolytic resistance, $Re(Z_S)$ (the real component of the impedance), measured in the sensing region while the laminate was driven for 65 hours with a ± 2 V triangular waveform at 20 $mVs^{-1}$ (2.5 mHz). The curves labelled "max," "min," and "mean" denote the cycle-wise maximum, minimum, and average values, respectively. A magnified view of the first hour is provided in Figure 21B. During the initial two cycles (approximately 800 s), the baseline conductance, $G_S^0$, remained essentially constant, indicating that evaporation of methyl propionate (MP) from the exposed edges had not yet influenced the pore-filling ratio (PFR) at the measurement site, or that a slight surface excess of solvent was present owing to the preload applied during assembly. This initial value, $G_S^0 = 3.0$ mS, was taken to correspond to PFR = 100%. As the experiment progressed and MP evaporated, $G_S$ decreased monotonically, eventually reaching an asymptotic value of $G_s^{final} = 0.6$ mS, which corresponds to an estimated PFR of approximately 20%.

Figure 21C presents the cycle-averaged PFR as a function of time for the entire experiment. For each cycle, PFR was computed as $G_S$ divided by $G_S^0$ and multiplied by 100%. The plot also includes the peak-to-peak conductance amplitude $G_S^{p-p}$, which tracks the PFR evolution: cycles exhibiting lower PFR invariably show smaller $G_S^{p-p}$. A non-smooth $G_S^{p-p}$ trace highlights the system's high sensitivity to minute conductance changes. Such irregularity is expected because redistribution of the mobile electrolyte within an open-porosity matrix is fundamentally stochastic—an attribute shared with many natural systems that leverage probabilistic fluid rearrangement to cope with uncertain, dynamic environments.

Figure 21D charts the temporal evolution of the dynamic pore-filling ratio, obtained by normalising the peak-to-peak conductance amplitude $G_S^{p-p}$ to the corresponding cycle-mean conductance $G_S$. Pumping efficiency was subsequently assessed in Figure 21E by plotting this dynamic PFR against the cycle-averaged (quasi-static) PFR, thereby expressing the fraction of liquid displaced relative to the total mobile liquid present. As anticipated, conditions in which the pores were either almost completely filled or nearly empty proved energetically inefficient; maximum performance was achieved at intermediate saturation levels. The data delineate a broad optimum window of roughly 30—75% PFR, over which the laminate exhibits its most pronounced dynamic swelling response. To elucidate the mechanisms governing the dynamic pore-filling ratio (PFR), the experimental record was partitioned into four successive intervals, labelled (a)–(d) in Figure 21E.

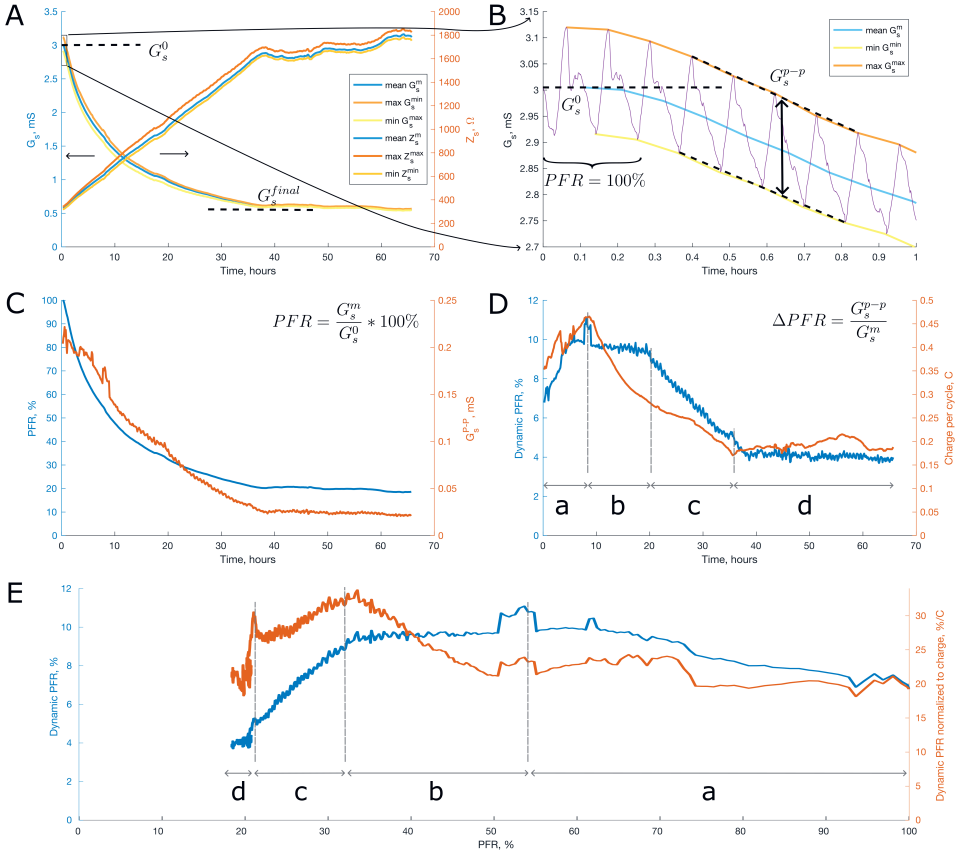


Figure 21. Maximum, minimum and mean values of electrolytic conductance $G_s$ (and resistance Re($Z_s$)) in consecutive cycles during natural evaporation of the volatile solvent (A). Transient course of $G_s$ during the first hour of the experiment, showing initial plateau of $G_s^0$, corresponding to 100% PFR (B). Transient cycle-averaged PFR estimation and dynamic peak-to-peak conductance $G_s^{p-p}$ variation (C). Transient dynamic PFR variation and variation of the charge introduced to the capacitive laminate per cycle (D). Dynamic PFR variation (in blue) with respect to the absolute PFR estimate (E). Charge-normalised dynamic PFR variation (in orange).

**Segment (a): PFR 100%—55%.**

The charge delivered per cycle rose by 28%, from 0.36 C to 0.46 C, reflecting the higher conductance G_s that accompanies solvent loss. The dynamic PFR amplitude increased from an initial 7% to a peak of 11%. Nevertheless, the PFR change per unit charge—and per absolute PFR—remained moderate, because pores already near saturation could accept little additional electrolyte.

**Segment (b): PFR 55%—32%.**

The dynamic PFR reached its maximal, nearly constant value of 9.5%, indicating efficient polarity-dependent filling and emptying of the pores. Meanwhile, the charge per cycle fell by 41% (from 0.46 C to 0.27 C), consistent with the declining number of liquid-filled pores available for ion storage as evaporation progressed.

**Segment (c): PFR 32%—21%.**

Both the dynamic PFR amplitude and the charge per cycle dropped sharply, by 47% and 37%, respectively. These reductions are attributed to breaks in liquid continuity between the sensing membrane and the driver electrodes, which restrict fluid transport, and to the diminished electrode surface area accessible for ion immobilisation.

**Segment (d): PFR < 21%.**

After complete evaporation of the volatile solvent, the absolute PFR could no longer vary appreciably, and the dynamic PFR stabilised at 4.1%. In contrast, the charge per cycle exhibited pronounced scatter (0.19 C, an 11% variation), highlighting the discrete, gap-dominated conduction pathways that emerge in an open-porosity matrix once air replaces the liquid phase.

### 5.2.4 Stiffness Modulation

Synthetic three-electrode laminate is characterised by its ability to actively modulate stiffness through charge-controlled liquid redistribution. In this system, a reversible reorganisation of an electrohydrodynamic medium within an open-porous polymeric matrix leads to localised swelling gradients, which in turn alter the mechanical compliance of the laminate.

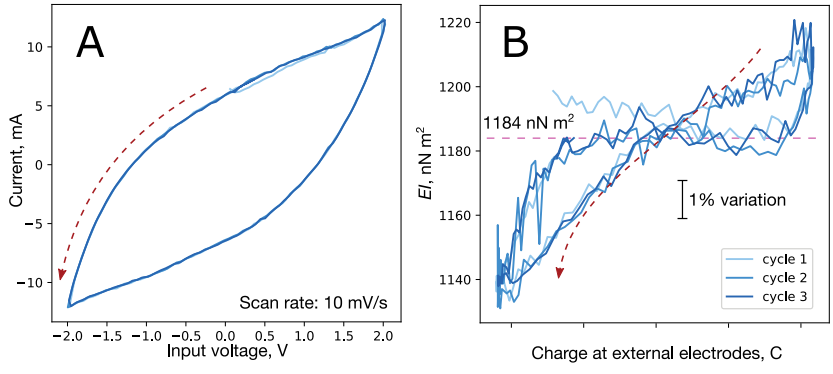


Figure 22. Cyclic variation of EI of a three-electrode capacitive laminate in response to a triangular input voltage. Cyclic voltammetry curve (at 10 mV $s^{-1}$ scan rate) (A). Variation of EI with respect to applied charge (B). The red dashed line indicates the direction of bending stiffness variation (B) and the corresponding charge direction in the cyclic voltammetry curve (A), respectively. The purple dashed horizontal line indicates the reference level of the uncharged capacitor.

Figure 22A depicts a cyclic-voltammetric response that is highly reproducible and approaches a rectangular shape, signifying primarily capacitive behaviour and the apparent absence of Faradaic peaks. Bending-stiffness measurements were carried out at a test frequency of 10 Hz. This setting represents a compromise between the increased loss tangent encountered at higher frequencies, stemming from the material's viscoelastic behaviour, and the improved signal resolution achievable at lower frequencies. Under cyclic electrical stimulation using a triangular voltage input, the laminate exhibits a distinctive 8-shaped hysteresis loop in its stiffness response (Figure 22B). Displacing the electrolytic solution from the external electrode to the central resulted in increased bending stiffness (evidencing liquid outflux and deswelling) and confirming non-thermal nature (on-dominated liquid displacement (liquid influx at positive applied potential) and non-thermal nature (in Joule heating, a symmetric response would be expected). Across each cycle, EI spanned 1220 nNmm$^2$ to 1131 nNmm$^2$, corresponding to deviations of +3.04% and −4.47% from the uncharged state. The sharper stiffening observed near the voltage extrema (±2 V) is ascribed to the higher ionic current, which enhances solvent flux. Notably, diffusive back-flow continually competes with ion-driven displacement, reflecting the highly dynamic nature of the system.

A similar 8-shaped hysteresis loop has been observed in electrosorption-driven osmotic actuators [88]. Whereas osmotic actuation typically relies on concentration gradients to generate osmotic pressure, such gradients are expected to contribute only marginally in the present three-electrode laminate. The open-porosity architecture enables electrolyte displacement with minimal pressure build-up. Due to the relatively high ratio between the total amount of ions in the system and the total area of electrode active surface area (carbon black surface area is approximately 1500 m$^2$ g$^{-1}$) [120], the concentration of [EMIM][Otf] in the plasticiser is predicted to decrease substantially during charging. Cyclic-voltammetry data indeed indicated a concentration change of about 55%, although a considerable amount of electrolyte remained within the laminate. In the absence of a semipermeable membrane, sizeable osmotic-pressure gradients are unlikely; thus, the bending-stiffness modulation is attributed mainly to bulk transport of the liquid electrolyte between laminate layers. Similar electro-osmotic effects have been reported in human skin, where surface charge drives directional fluid flow through a porous polymer matrix, producing swelling and elastic-modulus gradients detectable via impedance increases [121].

Owing to the geometric and functional symmetry of the three-electrode laminate, no bending actuation was exhibited. Nonetheless, a pronounced change in bending rigidity *EI* was detected, arising from complementary variations in the elastic modulus *E* and the area moment of inertia *I* during electrohydrodynamic fluid transfer. Because the outer electrodes are farther from the neutral axis than the inner electrode, their moments of inertia, and thus their contributions to the composite *EI*, are larger, making them more susceptible to modulation. Application of a charge produced an overall stiffness change of roughly 7%, thereby validating the underlying concept.

# 6. DISCUSSION ON LIQUID–MEDIATED SYSTEMS

## 6.1 Comparison of Bound and Free Liquid Measurement Techniques

In this section, we compare methods (Table 1) for free and bound content detection for analysis of their kinetic parameters.

### 6.1.1 Selectivity

In this study, methods were selected to distinguish between free and bound liquid. However, all methods are influenced by liquid in both states. Reflectometry and electrolytic conductance were used to detect free liquid content. In reflectometry, the refractive index of swollen cellulose at 589 nm decreases by only about 1% compared to dry cellulose, whereas the refractive index of an empty pore is approximately 25% lower compared to a water-filled pore [122]. The experimental data confirmed this selectivity, as the reflectometry signal returned to the baseline as the free-water phase was depleted, while bound water was still remaining (because of ongoing recoiling, Fig. 14A). Electrolytic conductance reflects the conductance of a continuously percolated free liquid occupying the porous structure; the contribution from bound liquid within the polymer matrix is much smaller, since ionic conduction predominantly occurs through the free liquid phase. Ion mobility in tightly bound water is several orders of magnitude lower [123], resulting in a minimal—but nonzero—contribution to overall conductivity. Polymers swollen with a conductive medium can still support limited charge transport via surface hopping along a monolayer of bound water [123].

Changes in flexural rigidity of a sample predominantly reflect bound-liquid effects—i.e., the softening and expansion of the material as it absorbs liquid, still to some extent reflecting the effect of poroelastic pressurisation, resulting from the coupling between solid deformation and free liquid flow within the porous architecture. During deformation, local changes in pore volume induce liquid redistribution, leading to transient pressure build-up within the porous network. This internal fluid pressure resists deformation and effectively increases the apparent stiffness of the material. The extent of this effect depends on the strain rate, liquid viscosity, and porous structure permeability—fast deformation and low permeability amplify the contribution of poroelastic pressurisation. In the present study, bending-stiffness measurements were conducted at 10 Hz—a frequency that provides adequate temporal resolution yet remains an order of magnitude below the 100 Hz onset of the glassy transition of polymer (PVDF-HFP in this case) [124], where the loss modulus departs from its low-frequency plateau; plasticiser-loaded polymers show their loss tangent maximum shifted toward higher frequencies [125]. Operating in this sub-transition regime limits the intrinsic rise of viscoelastic damping and, at the same time, minimises poroelastic pressurisation, whose viscous contribution to the loss modulus grows progressively with strain rate.

Swelling-induced volumetric expansion in passive hygromorphic structures produces deformation that is driven by internally generated swelling gradients; as liquid uptake proceeds, the convoluted architecture develops strain. Free liquid persists transiently within the capillary network after hydration ceases, as evidenced by the continued increase in the awn's rotation angle for 6–12 seconds, until global depletion is reached. The swelling imposed is mechanically analogous to the externally forced case described above: the spontaneously forming strains can create transient free liquid pressure gradients. As a hypothesis, a secondary, pressure-driven flow may arise, influencing both the kinetics of the hygromorphic actuation. However, once free water becomes depleted, poroelastic pressurisation effects vanish, and the change in hygroactuation extent reflects bound-water content. Volume expansion tracking is, therefore, a selective proxy for bound liquid.

### 6.1.2 Liquid Volume Resolution

The electrolytic conductance measurement is the most sensitive to changes in free liquid volume within pores; for instance, experiments have shown that less than one percent of PFR variation across 11 μm-thick porous media (interaction volume was 0.0033 $mm^3$) is resolvable in real time via conductance monitoring, with an instrumental noise level of approximately less than one percent of the full-scale conductance change. When using the electrolytic conductivity method, it is important to account for cross-sensitivity, as conductivity is influenced not only by the pore fill ratio but also by the variable ionic concentration of the conductive solution (as in the case of electrohydrodynamic medium). In the context of this work, liquid displacement was achieved via electroosmotic flow, leading to local variations in both the pore fill ratio (PFR) and the local fluid composition; the ion concentration changes are expected for the following reasons. A fraction of the ions is reversibly immobilised at the electrodes' surface due to the formation of a double electrical layer, leading to a decrease in the bulk average ion concentration and, thus, conductivity. Additionally, diffusive redistribution plays a role. In the context of electrokinetic displacement, both solvent and solute are transported concurrently, which induces the formation of a concentration gradient. The solvent undergoes diffusive redistribution in response to this gradient, progressively diminishing its magnitude. Since a significant portion of the ions is immobilised, the system evolves toward a final state characterised by a uniform concentration profile, albeit at a lower concentration level than initially present, which results in a corresponding decrease in the electrolyte's bulk conductivity. Consequently, this process detects free liquid volume variation locally and, in case of electrokinetic liquid displacement, is expected to systematically lead to an underestimation of the free liquid volume. Therefore, the sensitivity of this method to actual liquid volume displacement is most reliable when concentration changes in the electrohydrodynamic medium are minimal, namely, under high sweep voltage rates.

The swelling extent detection method reflects the absolute volume of bound water in the case of uniform swelling (without gradient formation), as the increase in bound liquid directly results in volume expansion (Figure 17B) due to swelling (the relationship is quasi-linear, with minor deviations at low bound liquid content) [126–127]. However, faster liquid redistribution leads to more pronounced swelling gradients; as a result, volumetric expansion is governed by differential rather than uniform swelling (as in the case of natural hygromorph). As the water front advances, the outermost fibre layers soak first, swell the most, and—because they sit furthest from the neutral axis—generate a larger bending moment for a smaller mass of bound water. Once these layers approach saturation, the through-thickness swelling gradient flattens: inner layers keep taking up water, but their shorter moment arm and the progressive rise in overall moment of inertia mean each extra unit of bound water adds proportionally less torque. Simultaneously, water plasticises the cell walls, lowering the local Young's modulus; early softening amplifies the initial rotation, reducing the composite flexural rigidity $EI$, so a given swelling produces a larger curvature. Thus, the emergence of a thin, highly swollen exterior layer functions as a mechanical amplifier: its large moment arm transforms small additions of bound water into large angular displacements. The combined effects of (i) diminishing mechanical leverage as hydration penetrates inward and (ii) modulus-dependent stress redistribution produce the observed, to some extent, non-linear relation between bound water content and uncoiling angle [128–129].

Owing to the tilted helix configuration, the awn can undergo up to eight full rotations upon water uptake (with sample-to-sample variability). Even when using a video camera with moderate resolution (assuming it can resolve a 0.1% change in rotational angle), the corresponding accuracy in detecting changes in bound water volume reaches 0.003%. Thus, the high resolution is achieved owing to the hygromorph's ability to translate volumetric expansion into rotation, combined with the high swelling capacity of the structure.

Hygroscopic polymers soften (*i.e.*, their Young's modulus decreases) and swell as their moisture content rises. Thus, the formation of a swelling gradient profile determines the overall variation in structural stiffness. In the present synthetic system case study, the swelling ratio was varied only modestly because the polymer's sorptivity is low, and the internal liquid volume was held constant. Under these constraints, the change in modulus—and thus the variation in flexural rigidity—remained moderate, about 7%. By contrast, the same bending-based read-out could produce a far stronger signal in systems where liquid uptake is unconstrained, such as the hygromorphic *Erodium* awns.

### 6.1.3 Spatial resolution

Given that the typical capillary diameter of natural hygromorphs (such as *Erodium* awn) is approximately 1 μm [41], a water-transport velocity of about 2 mm per second can be predicted only for surfaces whose wettability remains constant (i.e., glass), the contact angle does not vary and the Washburn equation is fully

applicable [130]. It also implies that meaningful dynamic information on hydration kinetics can be captured even at a 2 kHz sampling rate and a spatial resolution of 1 μm. In cellulose-based or other moisture-responsive substrates, however, the advancing liquid front progressively converts free water into bound water, thereby shifting the pore walls from initially less-wettable to more-wettable. During this transient, the imbibition rate is governed by the propagation of the hydrophilic–hydrophobic transition zone rather than by classical Washburn dynamics, and the initial velocity in a dry sample is therefore appreciably lower. Once the pores have become saturated with bound water and the contact angle stabilises, the Washburn relation is recovered.

High spatial resolution achievable with reflectometry (potentially down to single-capillary thickness) is attributed to shallow penetration depth; typically, a few hundred micrometers (samples exceeding 5 mm in thickness must be rendered translucent or subjected to serial sectioning) [131], owing to the extinction coefficient. Thus, this method is probing only the upper layers of the sample of thin samples (samples should be no more than 5 mm in thickness); in this study, the detectable volume was constrained to a 75 μm-thick region. When the sample is analysed in transmission mode, decreasing light intensity (through thickness) increases photon shot noise, while structural heterogeneity amplifies scattering-induced fluctuations, imposing an upper limit on sample thickness. Non-uniform pore filling and minor structural changes resulting from volume expansion can affect light scattering, thereby increasing the scattering-induced signal fluctuation (Figs. 14 and 15) and decreasing the minimally detectable PFR variation locally. In anisotropic structures, uneven free liquid distribution along the optical path leads to directional intensity differences; thus, to reliably quantify absolute changes in the free water content, reflectometry should be calibrated against gravimetric measurements.

Flexural rigidity measurement and detection of swelling extent are not intended for detailed mapping of liquid distribution. However, they provide valuable complementary information to more selective techniques, offering additional insights into liquid transport kinetics and the free-to-bound water conversion process. Stiffness measurement yields a single metric (i.e., effect of modulus gradient and geometrical variations due to swelling gradient); in this study, owing to a mirror-symmetric three-electrode laminate design, half-thickness resolution (200 μm) is achieved. Similarly, the swelling extent detection method provides limited spatial information: similarly to flexural rigidity measurement, the output is a single measure (e.g., strain) that corresponds to the cumulative effect of bound liquid over the whole sample.

### 6.1.4 Temporal resolution

All methods, except for the mechanical bending test, offer excellent temporal resolution—theoretically available in the MHz range or even higher—while the rate at which liquid moves through the porous structure is relatively low (typically less than 2 mm per second in the case of the wetted *Erodium* awn). Thus, these

techniques meet the requirements for capturing liquid volume changes in the time domain. Because the specimen is a porous polymeric matrix filled with liquid, mechanical testing simultaneously probes two coupled phenomena—swelling driven by bound liquid and pore pressure generated by free liquid during deformation. This cross sensitivity gives rise to the viscoelastic response of the material and offers an opportunity to quantify the kinetics of liquid redistribution, which will be addressed in future studies. When the goal is to approximate the quasi-static elastic modulus, the imposed strain rate (or, equivalently, the bending frequency) must be reduced, which unavoidably lengthens each measurement cycle. Thus, frequency-dependency can be exploited to separate the individual contributions of bound-liquid swelling and free-liquid pressure, providing complementary information that is not accessible with optical methods alone.

## 6.2 Liquid Dynamics at System Level

### 6.2.1 Structure Influence

Hygromorphic actuators' performance relies on their internal porous architecture to govern how liquid water is absorbed, distributed, and retained. Since the internal architecture of the hygromorph directs moisture uptake along preferred pathways, this same anisotropy of liquid transport gives rise to anisotropic swelling, which in turn determines the deformation mode during hygromorphic actuation. In nature, many hygromorphs exploit anisotropy to convert the uniform stimulus of humidity into a specific mechanical response; the stiff cellulose fibrils constrain the longitudinal axis upon swelling [41]. Synthetic analogues confirm the role of fiber architecture: by embedding tilted helical fibers in an elastic cylinder, researchers reproduced the coiling motion, with the helix angle governing coil tightness (moderate tilt yielding many tight coils, large tilt giving fewer, larger coils) [132]. Thus, an anisotropic structure can translate the isotropic expansion of a material (e.g., a swelling polymer) into a directional output via biased geometry. The anisotropic capillary bundle held mobile free water for approximately 30 seconds after humidification, setting the fastest possible actuation cycle. Drawing inspiration from natural hygromorphs, several design features influencing liquid transport and actuation in hygromorphs can be derived:

**Capillary anisotropy and length**

In an anisotropic porous architecture, pores oriented preferentially along one axis facilitate unidirectional capillary action. This directed liquid transport is important for establishing controlled swelling gradients, enabling complex, anisotropic actuation responses. Under finite-reservoir hydration, the liquid available is rapidly depleted by the outermost capillaries (analogous to the case where the capillary length is short); after hydration stop the onset of free-water depletion is delayed by approximately 30 s, which quantifies a finite traversal time along the capillary

bundle; the delay reflects axial draining through the anisotropic conduits. Because these surface fibres lie farthest from the neutral plane, their early swelling produces the dominant mechanical response, but it also lowers the local capillary pressure that drives further imbibition; the coiling-onset time $t_{coil}$ grows less than proportionally with $t_H$ (from 5 to 12 s as $t_H$ increases from 10 to 60 s), indicating that short near-surface capillaries dominate early swelling while contributions from deeper, longer paths add less to the torque. Once the near-surface liquid is exhausted, the capillaries become empty (due to evaporation and free-to-bound transition). As a result, deformation is higher at a lower volume of absorbed liquid at the early stage, when expansion of the outer layers is mechanically favored and viscous resistance to liquid redistribution is still negligible, favourable for use cases where lower but faster deformation is required.

**Helical Fiber Patterns**

In *Erodium* awns, cellulose microfibrils are oriented at a tilted angle, forming a helix. This tilted-helix geometry converts radial swelling into torque [41], providing a biological example of metamaterials; the larger the microfibril angle, the stronger the twisting moment. In the awn this coupling is rate-dependent: higher microfibril angles delay $t_{coil}$ and extend the free-water retention window (due to longer capillaries), evidencing a direct link between helix geometry and transport kinetics

**Surface Trichomes**

Trichomes increase the surface area and can draw liquid along by surface tension, effectively imbibing water toward the active tissue and accelerating hygroactuation[133].

### 6.2.2 Material Influence

The hygroscopic properties of the material directly influence both the kinetics of free liquid displacement and the free-to-bound transition rate, through their effects on contact angle and sorptivity, respectively. Upon hydration, free water enters the capillary network non-uniformly, establishing a gradient that drives rapid local swelling and a subsequent transition into a bound state. Because wetting converts the initially hydrophobic capillary walls to hydrophilic [16], liquid advances at an almost constant rate until viscous drag balances the capillary pressure; thereafter, flow slows; in case of source-unlimited hydration, this feature leads to an increase in the amount of free liquid proportional to the hydration time, provided that the pore geometry along the flow path remains unchanged (i.e., the Laplace pressure is invariant). Although the hydration front propagates approximately linearly with time along the capillaries, every newly wetted cross-section immediately contains a surplus of free water; the bound-water fraction in each section grows exponentially toward saturation. Summing over the steadily lengthening wetted zone

therefore yields an overall exponential increase in total swelling even while the spatial advance of the front itself remains linear (Figure 17D). This proportionality becomes important when evaluating the actuation rate of a hygromorph under dynamic hydration. When hydration pulses arrive at short intervals, a residual population of bound water is retained within the structure, so the advance of free liquid is not rate-limited by the hydrophilic–hydrophobic front propagation. Capillary flow therefore proceeds at the high velocity characteristic of a fully wetted substrate. This rate dependence matches the exponential rise of capillary-depletion time $t_D$ with hydration duration reported for the awn and the charge-rate-dependent crossover from symmetric to asymmetric PFR found in the electrohydrodynamic liquid-mediated system. In contrast, if the interval between hydration events is long enough for the bound water to evaporate, the capillary walls become less hydrophilic before the next pulse; the wetting front must then be re-established, imposing an additional kinetic barrier and markedly reducing the propagation rate of free liquid. Hence, more frequent hydration cycles yield a faster hygromorphic response by maintaining a permanently hydrophilic pathway for liquid transport.

The swelling kinetics can be described by a logistic function model in future work; modeling with a logistic function was beyond the scope of the current study, as the awn was far from saturation. As noted earlier, liquid in the capillaries can propagate either rapidly—consistent with the Washburn equation when the capillary walls retain bound liquid—or more slowly, when linear liquid advance is governed by the hydrophilic–hydrophobic front. In both regimes, the uptake kinetics can be described by a logistic function, and comparing the logistic parameters for a completely dry versus a retaining bound water (except when the hygromorph is saturated with bound water) hygromorph constitutes a powerful tool for quantifying the conductivity of the hygromorph's capillary network. Swelling of the hygromorph encompasses three distinct phases: (i) an initial exponential increase driven by efficient capillary transport, (ii) a deceleration phase as the supply of available binding sites diminishes, and (iii) saturation, where further water uptake ceases. The logistic function captures both the early rapid liquid imbibition and the asymptotic approach to a limiting value. Employing this model in future analyses will yield a realistic depiction of the interplay between capillary transport efficiency and the finite water-binding capacity of the system. The logistic function has already been used to describe similar phenomena in materials, e.g., the phase transformation of shape memory alloys [134–135] and hydrogels swelling [136]

Capillary-depletion time ($t_D$), defined in this work as the kinetics of free-water evaporation and its local conversion to bound water at the observation site after hydration stop, serves as a key parameter of the hygromorphic system, setting the lower bound on the hygroactuation-cycle duration.

### 6.2.3 Inter– / Intra– Exchange Influence

The influence of transient versus constant liquid content can lead to markedly different design implications. In liquid-mediated systems with transient liquid content (e.g., *Erodium* awn), the rate of imbibition decreases (due to a balance between capillary driving forces and viscous resistance) as the total liquid volume increases; consequently, the system exhibits its highest efficiency during the initial phase of absorption. In turn, the efficiency of liquid displacement in systems with constant liquid content is markedly affected by the average pore fill ratio. As PFR decreases from full saturation, liquid transport efficiency increases due to the availability of empty pores that can accommodate displaced liquid. However, in electrohydrodynamic liquid-mediated systems, a substantial decrease in PFR can result in discontinuities between liquid-filled regions and a corresponding decline in ionic conductivity.

Thus, in hygromorphic systems with constant liquid content, the efficiency of liquid displacement and the extent of swelling represent two mutually limiting parameters. The impedance-based laminate study shows that when the average PFR is held in the 30–75% window, the dynamic swing per cycle reaches a maximum of approximately 6% PFR in 80 seconds (20 $mVs^{-1}$ scan), whereas outside this window either void connectivity (PFR is below 30%) or the lack of acceptor volume (PFR is approximately 100%) throttles the flow (when the liquid is not leaving the system). While the extent of bulk swelling increases with the total liquid volume, the rate at which a swelling gradient is established depends on the efficiency of free liquid redistribution, optimal at intermediate PFR values; if the pores are already fully saturated (PFR is 100%), the pumping electrodes can still push liquid away from the source side, but the target region has no empty pores to receive it; the bulk displacement therefore produces little or no spatial contrast and the swelling gradient builds slowly. Moreover, in electrohydrodynamic liquid-mediated systems, lowering the average pore-fill ratio (PFR) enhances the dynamic PFR modulation and enables fast, reversible deswelling: partially emptied pores provide acceptor volume while the liquid network remains percolated; even if local voids are not initially available, spontaneous capillary backflow rapidly creates them. Conversely, as depletion proceeds and PFR drops below the connectivity range, the percolating pathway fragments, ionic conductivity collapses, and EHD pumping becomes self-limiting: net liquid displacement halts and only capacitive charging currents persist. Once the field is reversed, free liquid is evacuated from previously swollen zones and the structure contracts on a time-scale comparable to the preceding swelling cycle. This combination maximises the amplitude of PFR change per cycle, with experiments revealing a broad optimum at approximately 30–75% PFR and a charge-normalised peak efficiency near 32% PFR (Figure 21E). Consequently, constant-volume liquid-mediated systems offer two distinct optimisation pathways: maximizing the extent of swelling through increased displaced volume or enhancing the rate of swelling via faster liquid redistribution.

In systems with transient liquid content (e.g., the *Erodium* awn), free liquid imbibition is most rapid at the onset, due to the balance between capillary pressure and viscous drag [130, 137]. According to this model, the rate of liquid propagation decreases over time and follows a square-root dependence on time. The Washburn equation assumes constant values for capillary radius, liquid surface tension, contact angle between the liquid and pore walls, and liquid viscosity. This assumption holds for non-swellable capillaries, where the material does not absorb liquid and thus retains its original wettability. For a pre-wetted capillary wall whose contact angle has already dropped, propagation follows classic Lucas–Washburn scaling (square-root dependence on time); this regime is also observed in the electrohydrodynamic liquid-mediated systems, where the wall chemistry is fixed and the initial segment of the PFR–time curve indeed scales with the square root of time (Figures 20C and 20D). When the awn is dry, the first hydration pulse must create that hydrophilic surface, so the front advances almost linearly with time; optical reflectometry of *Erodium* awns captures this constant-rate stage in the growth of the FWHM scattering peak (Figure 15A and 15B). The juxtaposition of the two regimes explains why the theory is relevant: it predicts which time law governs propagation depending on the instantaneous wetting history, a variable that can be controlled via PFR in synthetic systems. As discussed in the previous section, in hygromorphic systems, the material's hydrophilicity increases progressively with bound liquid content [16]. As a result, two distinct modes of liquid imbibition can occur in such systems:

(1) Pre-wetted / constant-angle mode—when the hygroscopic material is pre-wetted, the contact angle can be treated as approximately constant, and the propagation rate follows the Washburn model, with the highest velocity at the beginning.

(2) Front-limited (dry-start) mode—when the contact angle between the liquid and the hydrophobic cellulose is initially high, and liquid advances at a relatively constant rate as the wetting front propagates through the material and locally increases hydrophilicity.

### 6.2.4 Control Influence

In an actively controlled liquid-mediated system, the displacement rate and direction of liquid can also be modulated by adjusting the pumping rate and direction. Liquid displacement reflects the superposition of induced bulk liquid transport and spontaneous diffusive redistribution. At high pumping rates, large liquid volumes are moved rapidly because the forced flow overwhelms diffusion; when the voltage sweep is slowed, diffusive backflow competes with the imposed flow, allowing the system to approach quasi-equilibrium. Because the device operates at constant total liquid volume in a closed, percolated network, sustained throughflow is not possible: any imposed flux relaxes as concentration and PFR gradients dissipate, so transport proceeds as a sequence of redistribution phases separated by quasi-equilibria. The system can approach a quasi-equilibrium state during

each half of the pumping cycle. This is evidenced by the nearly identical slopes of the pore fill ratio variation for positive and negative polarisation and the smaller hysteresis window compared to that observed at higher sweep voltage rates (Figure 20C). Conversely, at high pumping rates, the imposed flow drives a net solvent flux that outpaces diffusive backflow; the resulting PFR gradient gives rise to a strongly asymmetric PFR response. In practical applications, combining low and high pumping rates can enhance the overall rate of liquid displacement even further. Operationally, pre-polarising the laminate in one direction first loads the electrical double layers and builds opposing PFR gradients; when the field is immediately reversed, that stored charge and the pre-existing gradients assist the imposed drift. As a result, the effective charge available for transport in the next half-cycle increases (approximately doubling relative to an unpolarised start), producing a brief surge in net liquid displacement—consistent with the matched slopes and narrower hysteresis at low scan rates in Figure 20C.

## 6.3 Practical Implications for Robotics

### 6.3.1 Case Study: Multidirectional Actively Controlled Stiffness

This work introduces an approach for material-level stiffness modulation. In contrast to typical engineering solutions for stiffness modulation (frictional jamming, thermal phase-change modulation, electromechanical systems, etc.), this approach manages liquid displacement to form a swelling gradient profile (at 200 μm spatial resolution) throughout the thickness of the structure.

One advantage is versatility in achieving a spatially distributed stiffness variation profile; traditional methods like jamming or thermal modulation tend to affect an entire segment uniformly, whereas the liquid approach can create compliance gradients. A key drawback of jamming is scalability; jamming works best in volumes above a few millimeters in size (e.g., 4 mm and more) [138–139] because a sufficient size of particles or thickness layers is needed to obtain a higher stiffness change. By contrast, the swelling-gradient strategy demonstrated here achieves controllable stiffness changes in films only 400 μm thick, giving sub-millimetre spatial resolution. Thus, a liquid-mediated mechanism can outperform classic jamming in terms of resolution, offering a route for fine-grained compliance patterning. Owing to material-level control, the thermal stiffness modulation method can be implemented at any scale (micro-scale SMP fibers or films); yet, creating high-resolution spatial stiffness patterns is challenging because heat diffuses. Although the primary advantage of thermal methods lies in their wide range of stiffness variation (e.g., from 3 MPa in the soft state to 3 GPa in the rigid state) [140], their use in applications involving human interaction—a major constraint for wearable devices—or delicate environments is limited not only by safety concerns associated with elevated operating temperatures but also by the need for active cooling, which introduces additional energy demands, bulk, and maintenance challenges. Additionally, due to the modulation of intrinsic material properties, the introduced liquid-based approach is reliable under conditions

involving relatively high external strains; in the case of PVDF-HFP polymer, it can reach strains of up to 12% [141].

In terms of limitations, the current liquid-based technology provides a more limited stiffness modulation range than alternatives (jamming and thermally stiffness modulation). Jamming as an "assembly-level" solution incurs penalties in bulk, external hardware, and limited miniaturisation, whereas the liquid-swell method is intrinsic to the material. Thus, the EHD liquid approach, conversely, sacrifices some range in exchange for safer (non-thermal) operation, smaller scales (structure thickness can be below 400 μm), fine-grained control, aligning with the needs of robots in contact with delicate environments.

### 6.3.2 Design Trade–Offs and Limitations

The design and operation of the charge-controlled swelling system involve several trade-offs and limitations that need to be considered for practical applications. One trade-off arises from integrating the pumping and stiffness-modulating functions within the same composite structure. This approach simplifies fabrication, provides volume efficiency, and allows for a high level of integration, which is advantageous for distributed and wearable applications. Yet, this integration means that the same volume is shared between the pumping apparatus and the stiffness-modulating layers. As a result, the mechanical properties of the electrode, particularly its elastic modulus, are higher than those of a softer, standalone swelling layer, further limiting the achievable range of stiffness modulation.

There are also inherent limitations related to the material selection and processing. The choice of a moderately hydrophobic polymer (PVDF-HFP) combined with a hydrophilic electrolyte ([EMIM][OTf]) results in only moderate swelling effects. To achieve a more pronounced stiffness response, the interaction between the polymer matrix and the electrolytic solution must be carefully balanced; it should be strong enough to promote significant swelling but weak enough to ensure reversibility. In addition, the control over the pore size, shape, and distribution during the spray-deposition process remains a challenge and can affect the consistency and efficiency of liquid redistribution. Furthermore, the operation of the system is constrained by the diffusive redistribution, which restricts its overall efficiency in scenarios requiring prolonged stiffness modulation.

## 6.4 The Role of Liquids in Embodied Intelligence

### 6.4.1 Liquids as Part of the Embodiment

When liquids become confined within a solid matrix—whether by adsorption onto macromolecules or nanoconfinement in pores—they behave mechanically more like solids than fluids, yet never lose all molecular flexibility. In cellulose-based materials, for example, water molecules form hydrogen bonds with polymer chains and occupy nanometer-scale cavities, yielding a viscoelastic composite

whose stiffness and yield behavior depend on the amount of bound water [142]. Likewise, nanoconfined fluids exhibit altered phase transitions: the glass-transition temperature of water in pores can rise by tens of degrees, reflecting strong coupling with the host matrix [143]. Even so, bound water retains residual mobility, diffusing under thermal or mechanical perturbations—a characteristic absent in true solids [144]. These observations support a continuum view of phase behavior in which liquids shift toward a solid-like regime upon binding yet remain partly fluid, blurring the conventional solid–liquid boundary.

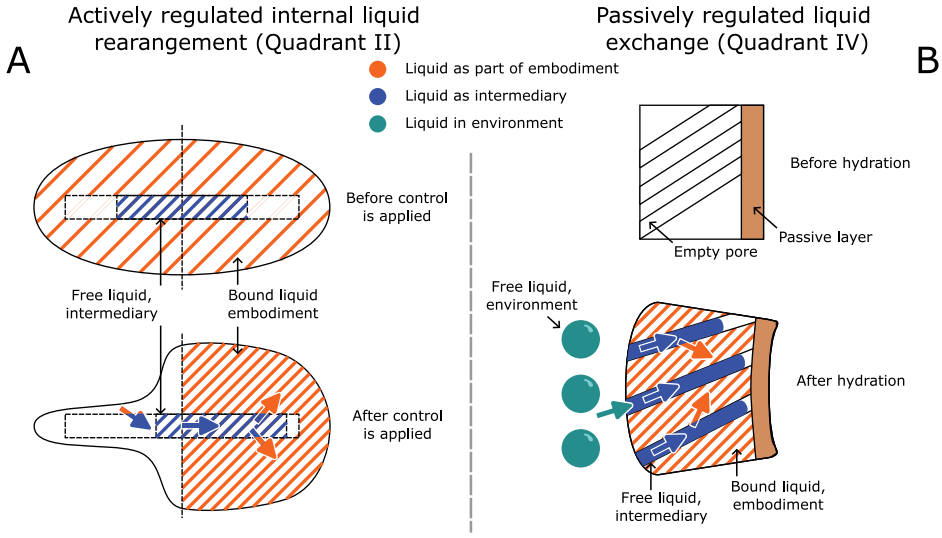


Figure 23. General concepts of actively regulated internal liquid rearrangement (A) and passively regulated liquid exchange (B) systems, and the roles of liquid in the emergence of Embodied Intelligence.

Free-to-bound conversion cycles endow the material with transient, embodied functionality. When free water infiltrates a hygromorph's capillaries or an electrokinetic laminate's pores, it temporarily integrates into the solid matrix by binding to cellulose fibers or polymer chains. During the free-to-bound transition, the liquid loses bulk mobility and directly contributes to tissue swelling or stiffness modulation; during the bound-to-free transition, the liquid is removed from contact with the polymer—whether by pumping or evaporation—allowing the polymer to deswell and recover its original mechanical properties. Thus, liquid alternately becomes an integrated component, constituting a form of transient embodiment.

### 6.4.2 Liquids as Intermediaries

To highlight how passive and active liquid control differ in practice, we contrast two representative systems from opposite quadrants of our classification. In a passively controlled hygromorphic system (*Erodium cicutarium* awns, Quadrant IV), environmental humidity drives liquid into anisotropic microchannels via capillary action; the narrow, helically arranged pores (tens of μm in diameter) generate strong suction, drawing moisture into the structure [145]. Inside, water binds to cellulose, producing swelling that uncoils the awn [146]—a response that relies on a transient internal liquid pool. In contrast to passive capillarity, actively controlled synthetic systems (Quadrant II) that employ active electrokinetic flows to displace free ionic solution within a porous polymer matrix maintain constant total liquid content with varying proportions between free and bound liquids. In both cases, the redistribution of liquid sets up transient PFR gradients; however, the active laminate does so without exchanging fluid with the environment, whereas the awn's total water content rises and falls with ambient humidity.

Whether driven by ambient humidity or by pumping, free liquids in both natural and synthetic systems mediate mass transport. In hygromorphs, free water conveys ambient humidity into swelling, then returns to vapor during deswelling—a transient transport intermediary. In electrokinetically liquid-mediated systems, free liquid cyclically transitions between mobile and bound states, carrying control signals into mechanical states and back, without altering the system's total liquid inventory. In both cases, free liquid functions as a transport medium that bridges stimuli and response.

### 6.4.3 Liquids as Environmental Elements

In systems that represent Quadrant III, liquids are actively exchanged with the environment under internal control, yet they never remain permanently within the body (e.g., jet-propelled soft robots [147]). In this system, free liquid serves neither as a permanent structural element nor as a fixed internal fluid reservoir but as a working medium exchanged on demand. For jet-propelled robots, thrust and efficiency scale with the density and viscosity of the surrounding water: accelerating a more viscous fluid demands extra power, yet this very sensitivity offers an additional control channel. By sensing local temperature, salinity, or viscosity, the robot can adapt its pulse timing and nozzle stroke to maintain constant thrust or even exploit stratified layers for manoeuvring [147–148]. In such systems, exchange with the environment dominates, and the liquid role becomes inherently context-dependent: liquids do not belong to the embodiment, but are the environment in which the body operates.

Although the free liquid exchange mechanism is different (passive and active) across both quadrants, the free liquid, when it is not inside the body, defines the behaviour of the body, and is considered an environmental medium until it becomes associated with the body or performs any transport function with the body.

# 7. CONCLUSIONS

## 7.1 Answers to Research Questions

In this thesis, the overall aim was to elucidate how liquid displacement kinetics and oriented transport within porous actively and passively controlled morphing structures can be harnessed. With this work, the following research questions have been answered:

*1.1 What is the role of liquids in embodied intelligence, and how does this role differ based on whether the liquid is in a bound or free state?*

During the free-to-bound transition, liquid loses its bulk mobility and becomes mechanically coupled to the surrounding material, contributing to swelling and stiffness modulation; in *Erodium* awn and synthetic laminate studies, this coupling manifests as swelling and stiffness change, i.e., bound liquid becomes part of the embodiment (Publication I). When free liquid is confined within the body, whether liquid content is constant or transient, and mediates mass transport, it functions as an intermediary that links environmental stimuli to system response. In the synthetic laminate, free liquid functions as an internal transport medium: conductance–charge traces at different scan rates/voltage windows resolve the superposition of fast electrokinetic pumping and slower diffusive backflow, i.e., how imposed control signals are transmitted through the body by mobile liquid. In contrast, free liquid in systems that actively exchange fluid with the environment under internal and external control, without retaining it permanently, can be considered part of the environment, as in the case of hydration with aerosol. Within the framework of embodied intelligence, the role of liquid can thus be interpreted as twofold: (i) modulating the system's physical properties, eventually contributing to embodiment, or (ii) transmitting stimuli from the environment.

*1.2 What practical design guidelines follow from choosing (i) active versus passive control and (ii) internal liquid confinement versus environmental liquid exchange, when using liquids as functional elements in intelligent systems?*

In passive humidity-driven systems (Publication II), the liquid is drawn in solely by capillary forces; no internal power is needed. In *Erodium* awn experiments, the capillary bundle held mobile free water for about 30 seconds after each humidification pulse. That residual bound water lowers the contact angle, so the next pulse enters faster—a behaviour that functions as a moisture-based "memory," much like a shape-memory alloy remembers its last thermal state. Passive control is therefore attractive wherever zero power consumption and environment-coupled sensing are the main goals—for example, moisture-responsive building vents or seed-inspired self-burying devices. In active pump-driven liquid-mediated (electrohydrodynamic liquid-mediated, in this case) systems (Publication III), the liquid rate can be amplified to a desired extent. When the liquid is

pumped quickly, electro-osmotic flow dominates, and a large volume moves in one burst. When the liquid is pumped slowly, diffusion cancels most of the imposed flow and the system approaches equilibrium—a useful "reset" step that restores the ion and PFR gradients, yet alternating a slow reset with a fast burst and pumping direction essentially increases flow rate. A practical guideline for hybrid systems is to design the liquid-mediated structure with limited sorptivity, allowing it to passively absorb fluid—without external energy—until the pore-fill ratio reaches roughly 30%, and then use the internal pump to actively redistribute that stored water.

When the liquid is confined inside the body, intelligence comes from how well that fixed volume can be shuffled between pores. We found that the systems with confined liquid perform best at an intermediate pore-fill ratio (approximately 30–75%): below 30% the conductive pathway breaks (in case of electrohydrodynamic medium); above 75% there is no spare space to accept fluid. Staying in that window gives a fast, reversible shape change that is independent of the environment. When the liquid is taken from the environment, as in an *Erodium* awn, the first imbibition pulse is the fastest; afterward, the rate falls with the square root of time. The bound water left behind lowers the contact angle, so the next pulse comes in more easily. Thus, the structure "remembers" recent humidity and passively couples to ambient conditions.

### *2.1 How to access liquid content variation (separately free and bound) locally in porous structures?*

Four complementary, non-invasive methods quantify free- and bound-water dynamics:

Free liquid:

- Optical reflectometry: variation in transmitted and scattered light intensity due to refractive index mismatch between empty and liquid-filled pores (Publication II).
- Electrical conductance: volume conductance of porous structure filled with conductive medium (Publication III).

Bound liquid:

- Hygroactuation extent: swelling-induced strain (Publication II).
- Mechanical bending: swelling-induced variation of elastic modulus and geometry (Publication IV).

### *2.2 What are the kinetic parameters associated with liquid redistribution in swellable porous structures and the interplay between free and bound states?*

To characterise the temporal behaviour of free and bound water in both natural and synthetic porous systems, two complementary sets of kinetic parameters were defined and measured, in addition to basic descriptors (i.e., sorptivity).

- Free liquid retention kinetics:
  - Full Width at Half Maximum (*FWHM*) of the scattering light intensity peak: quantifies the duration over which free water is present within the awn (Publication II).
  - Capillary depletion times ($t_D$): mark the interval from peak free water content to its transition into bound water or evaporation, capturing the persistence of mobile water within anisotropic capillaries (Publication II).
  - Coiling onset time ($t_{coil}$): indicates the delay between the end of hydration and the onset of coiling, linking free-to-bound liquid conversion and bound liquid depletion kinetics (Publication II).
- Fast pump-driven and slow diffusive liquid transfer time constant: observed from the asymmetry of conductance variation profiles versus different scan rates (Publication III).
- Dynamic PFR range: identifies the pore fill ratio variation window (Publication III).

*3.1 How can ion electrosorption be effectively used to modulate stiffness?*

Ion electrosorption enables charge-controlled routing of a fixed electrolyte to form through-thickness swelling gradients that modulate bending stiffness *EI* (Publications III and IV). In practice, the same imposed charge that accumulates at the electrodes drives bulk liquid displacement (via electrokinetic flow), so pumping and stiffness tuning occur simultaneously. This coupling is observable as a reproducible hysteresis of *EI* versus charge under cyclic drive, evidencing controllable, reversible stiffness changes with sub-millimetre spatial resolution (through ~200 μm layers) in the presented prototypes. Design rules are as follows:

- Operate at an intermediate pore-fill ratio (PFR) where transport remains percolated yet void space exists—this maximises charge-normalised displacement and thus stiffness tunability (broad optimum 30–75% PFR; charge-normalised peak near 32% PFR).
- Use drive parameters to set time scales: higher scan rates emphasise electrokinetic transfer and enlarge the EI swing per cycle; slower scans allow diffusive backflow to reduce gradients, which can be exploited as a quasi-reset. The conductance–charge asymmetry vs. scan rate directly reveals these two time constants and informs control.
- Orient porosity with the target flow direction: combining the natural anisotropic case (awn studies: oriented capillaries set retention/depletion kinetics) with the synthetic constant-volume case suggests that introducing or aligning anisotropy in synthetic matrices will further increase routing efficiency and stiffness response for a given charge budget.

*3.2 How to experimentally characterise the stiffness modulation due to bound liquid redistribution?*

To experimentally characterise stiffness modulation arising from bound-liquid redistribution, a liquid-mediated laminate that embeds the routing architecture was designed (Publication IV); this laminate is then tested in a cantilever configuration under cyclic bending to quantify the bending stiffness *EI*. The measured *EI* variation directly reflects the through-thickness swelling gradient induced by charge-controlled liquid transfer.

## 7.2 Limitations

Despite the advances demonstrated in this work, several important limitations warrant discussion:

1. Limited penetration depth of optical methods.

Reflectometry and transmission light intensity variation track free-water uptake quickly and non-invasively, but probe only the top few tens of micrometers. It therefore misses hydration in deeper layers of thick or highly scattering samples, confining the method to thin or surface-level studies.

2. Elastic modulus and second moment of inertia are measured together

The bending test for measuring flexural rigidity does not allow for the separate determination of the elastic modulus *E* and the second moment of inertia *I*, nor does it enable the independent analysis of how these properties change in individual layers within the composite.

3. Global bound liquid detection

In contrast to free liquid detection methods, the methods presented in this study for assessing bound liquid content capture only the global volumetric changes, without the ability to resolve the bound liquid gradient profile: visual observation reflects overall volume variation due to swelling, while the mechanical bending test can detect the presence of swelling gradients across the sample's thickness.

4. Diffusive backflow and temporal stiffness variation

The electrokinetic transport leads to a localised decrease in ion concentration within the electrolyte near the electrode surfaces. The resulting concentration gradient creates an osmotic pressure difference, which drives solvent molecules to diffuse back into the ion-depleted region in an attempt to restore equilibrium. This diffusive back-equilibration limits this approach to short or dynamic applications.

5. Trade-off between pumping performance and stiffness modulation.

In the three-electrode laminate, increasing carbon loading enhances pumping performance by enlarging the effective electrode surface area; however, it simultaneously increases the composite's stiffness, thereby reducing the achievable range of bending stiffness modulation. The modest 7% reversible change in stiffness highlights an inherent trade-off between pumping efficiency and mechanical compliance variation.

## 7.3 Future Research Directions

Reflectometry, which precisely detects free liquid displacement kinetics (rate of accumulation and depletion) and overall content variation, within lumens and other internal plant structures, can be extended to time-of-flight measurements (by mapping multi-point optical sensing) used as a non-invasive method for plant health monitoring by analysing thin (below 200 um thick) plant structures and surfaces. By tracking changes in light reflection associated with liquid movement or depletion, reflectometry enables the assessment of water transport efficiency (early signs of dehydration) and transpiration kinetics.

For larger woody structures, the mechanical bending test, based on Euler–Bernoulli beam theory for assessing structural rigidity, can be effectively used to study the degree of hydration. By applying mechanical stress and measuring the resulting flexural response, this method provides insight into changes in the overall elastic modulus as a function of water content, not due to transversal swelling profile variation. Since variations in trunk thickness are negligible, trunk volume can be considered constant, allowing the observed stiffness changes to be attributed primarily to hydration-induced modulation of the material's elastic properties.

While changes in electronic impedance allow for the quantification of free liquid displacement (via pore filling), this technique complements the bending test particularly well, as it enables the study of liquid movement within natural systems (plat liquids are inherently conductive) that are subjected to mechanical deformation, crucial in the case of reflectometry. The integration of these methods in future studies will enable the development of a powerful instrumentation platform for analyzing the kinetics of free and bound liquid in plants.

# SUMMARY IN ESTONIAN

## Passiiv- ja aktiivvedelikuvahetus looduslikes ja sünteetilistes kujumuutvates süsteemides

Taimed kohandavad oma mehaanilisi ja struktuurseid omadusi, jaotades vedelikku ümber oma valendikes (torukujulistes struktuurides), pakkudes inspiratsiooni vedelikul põhinevale inseneriteadusele. Nii looduslikud kui ka sünteetilised niiskuse toimel vormi, kuju või suurust muutvad objektid ehk hügromorfid näitavad, et sisemine vedeliku liikumine suudab muuta nende kuju ja muganevust. Käesolev väitekiri uurib vabalt liikuvate vedelike (poorides liikuvad) ja seotud vedelike (absorbeerunud ja paisumist põhjustavad) koostoimet poorsetes materjalides. Seejärel näidatakse, kuidas see vastastikmõju võimaldab vedelikul põhinevates kehalistes süsteemides kuju ja painduvuse sihipärast muutmist.

Võrreldakse kahte süsteemi, mis erinevad vedeliku juhtimise (aktiivne või passiivne) ja säilitamise viisi poolest: looduslik *Erodium*'i seemneohe, mis passiivselt neelab ja vahetab vedelikku keskkonnaga, ning sünteetiline elektrokinetiline laminaat (selle töö raames loodud), mis aktiivselt jaotab ümber endas sisalduvat vedelikku. Võrdlus toob esile ka taimede anisotroopse mikrostruktuuri ja sünteetiliste maatriksite isotroopse olemuse erinevused, samuti vabade ja seotud vedelike erinevad rollid.

Võrdlev analüüs näitab, kuidas juhtimisviis, vahetusviis (avatud vs suletud), struktuursed omadused ja vedeliku olek ühiselt määravad vedeliku ümberjaotuse ning sellest tuleneva lokaalse paisumise ja painduvuse. Arendati neli meetodit, et eraldi kvantifitseerida:

1. Vabade vedelike transpordi tuvastamine optilise reflektomeetria abil ja elektrolüüdilahuse elektrijuhtivuse kaudu.
2. Maatriksi paisumist vabade vedelike muutumisel seotud vedelikeks, mõõdetuna lahtikeerdumise ulatuse ja paindetestide kaudu.

Uuringu tulemused näitavad, et jääkvedelik looduslikus hügroskoopses struktuuris toimib kui „süsteemi mälu", mis pärast niisutamist kiirendab vedeliku omastamist järgnevate niisutustsüklite ajal. Sünteetilises hügromorfis, kus vedeliku maht on konstantne, saavutati parim tulemus – dünaamilise poori täituvuse muutus – keskmise täituvuse juures (umbes 30–75%). Juhtsignaali (skaneerimiskiiruse) ja lokaalse poori täituvuse muutuse vahel ilmnes mittelineaarne seos; difuusne tagasivool toimis kiirusest sõltuva lõdvestusmehhanismina, mis tasandas ja vastustas kehtestatud gradiendid.

Vedelikul põhinev sünteetiline süsteem, mis reguleerib jäikust mittemonotoonse paisumisgradiendi kaudu (kahepoolne vedeliku ümberjaotus), näitas 7% struktuurset jäikuse muutust. Väitekiri näitab, kuidas vedelikud poorsetes süsteemides võivad toimida hajutatud ja pöörduvate „mehaaniliste protsessoritena", mis toimivad nii paralleelselt (nagu sünteetilises süsteemis) kui ka järjestikku (nagu ohtes, kus üksused on virnastatud). Samuti esitatakse disainipõhimõtted vedelikul põhinevate paisuvate süsteemide loomiseks.

Töö toob esile neli peamist panust:

1. See arendab vedelikul põhineva kehalise tarkuse teooriat.
2. See tutvustab mitmerežiimilisi jälgimistehnikaid vabade ja seotud vedelike jaoks, kõrge ajalise ja ruumilise eraldusvõimega, rakendatuna poorsetele struktuuridele.
3. See kehtestab disainireeglid mitmesuunaliseks vedeliku ümberjaotuseks, et võimaldada lokaliseeritud paisumist hügromorfsetes süsteemides.
4. See esitab kontseptsiooni muutuva jäikusega vedelikul põhinevast süsteemist, mille tulevikuperspektiiv on pehme robootikas, näiteks kantavates haptika-seadmetes.

# LIST OF FIGURES

# LIST OF TABLES

# REFERENCES


[1] Rus, D., & Tolley, M. T. (2015). Design, fabrication and control of soft robots. Nature, 521(7553), 467–475.

[2] Pfeifer, R., & Bongard, J. (2006). How the body shapes the way we think: a new view of intelligence. MIT press.

[3] Team, G. R., Abeyruwan, S., Ainslie, J., Alayrac, J. B., Arenas, M. G., Armstrong, T., ... & Zhou, Y. (2025). Gemini robotics: Bringing AI into the physical world. arXiv preprint arXiv:2503.20020.

[4] Noreils, F. R. (2024). Humanoid Robots at work: where are we?. arXiv preprint arXiv:2404.04249.

[5] Xiang, J., Tao, T., Gu, Y., Shu, T., Wang, Z., Yang, Z., & Hu, Z. (2023). Language models meet world models: Embodied experiences enhance language models. Advances in neural information processing systems, 36, 75392–75412.

[6] "Reflecting On 2024's 'Year Of Embodied AI': Hype And Reality" https://www.forbes.com/councils/forbestechcouncil/2024/12/23/reflecting-on-2024s-year-of-embodied-ai-hype-and-reality/ (accessed Apr. 20, 2025).

[7] "Embodied Ai Market Is Expected To Reach Revenue Of USD 4,067.3 Mn By 2033, At 5.4% CAGR: Dimension Market Research." https://www.globenewswire.com/news-release/2024/12/09/2993811/0/en/Embodied-Ai-Market-Is-Expected-To-Reach-Revenue-Of-USD-4-067-3-Mn-By-2033-At-5-4-CAGR-Dimension-Market-Research.html (accessed Apr. 20, 2025).

[8] Zhou, S., Li, Y., Wang, Q., & Lyu, Z. (2024). Integrated actuation and sensing: Toward intelligent soft robots. Cyborg and Bionic Systems, 5, 0105.

[9] Lin, B., Song, S., & Wang, J. (2024). Variable stiffness methods of flexible robots for minimally invasive surgery: A review. Biomimetic Intelligence and Robotics, 4(3), 100168.

[10] Coyle, S., Majidi, C., LeDuc, P., & Hsia, K. J. (2018). Bio-inspired soft robotics: Material selection, actuation, and design. Extreme Mechanics Letters, 22, 51–59.

[11] Bongard, J. (2015). Using robots to investigate the evolution of adaptive behavior. Current opinion in behavioral sciences, 6, 168–173.

[12] Brooks, R. (2003). A robust layered control system for a mobile robot. IEEE journal on robotics and automation, 2(1), 14–23.

[13] Stella, F., & Hughes, J. (2023). The science of soft robot design: A review of motivations, methods and enabling technologies. Frontiers in Robotics and AI, 9, 1059026.

[14] Varela, F. J., Thompson, E., & Rosch, E. (2017). The embodied mind, revised edition: Cognitive science and human experience. MIT press.

[15] Nakagaki, T., Yamada, H., & Tóth, Á. (2000). Maze-solving by an amoeboid organism. Nature, 407(6803), 470–470.

[16] Eger, C. J., Horstmann, M., Poppinga, S., Sachse, R., Thierer, R., Nestle, N., & Rühe, J. (2022). The structural and mechanical basis for passive-hydraulic pine cone actuation. Advanced Science, 9(20), 2200458.

[17] Brooks, R. A. (1991). Intelligence without representation. Artificial intelligence, 47(1–3), 139–159.

[18] Mengaldo, G., Renda, F., Brunton, S. L., Bächer, M., Calisti, M., Duriez, C., & Laschi, C. (2022). A concise guide to modelling the physics of embodied intelligence in soft robotics. Nature Reviews Physics, 4(9), 595–610.

[19] Cianchetti, M. (2021). Embodied intelligence in soft robotics through hardware multifunctionality. Frontiers in Robotics and AI, 8, 724056.
[20] Hsiao, T. C. (1973). Plant responses to water stress. Annual review of plant physiology, 24(1), 519–570.
[21] Shibata, M., & Mogami, J. (2019). Toward a multifaceted understanding of plants' adaptation mechanisms. Journal of Plant Research, 132, 299–299.
[22] Scharwies, J. D., & Dinneny, J. R. (2019). Water transport, perception, and response in plants. Journal of plant research, 132(3), 311–324.
[23] Lambers, H., Oliveira, R. S., Lambers, H., & Oliveira, R. S. (2019). Plant water relations. Plant physiological ecology, 187–263.
[24] Shevela, D., Kern, J. F., Govindjee, G., & Messinger, J. (2023). Solar energy conversion by photosystem II: principles and structures. Photosynthesis Research, 156(3), 279–307.
[25] Zhang, X., Ramakanth, K. K., & Long, Y. (2024). The biomechanics of turgor pressure. Current Biology, 34(20), R986–R991.
[26] Tyree, M. T., & Zimmermann, M. H. (2002). Xylem structure and the ascent of sap. Springer Science & Business Media.
[27] Schroeder, J. I., Allen, G. J., Hugouvieux, V., Kwak, J. M., & Waner, D. (2001). Guard cell signal transduction. Annual review of plant biology, 52(1), 627–658.
[28] Hejnowicz, Z. (1997). Graviresponses in herbs and trees: a major role for the redistribution of tissue and growth stresses. Planta, 203, S136–S146.
[29] Aharon, R., Shahak, Y., Wininger, S., Bendov, R., Kapulnik, Y., & Galili, G. (2003). Overexpression of a plasma membrane aquaporin in transgenic tobacco improves plant vigor under favorable growth conditions but not under drought or salt stress. The Plant Cell, 15(2), 439–447.
[30] Chaumont, F., Barrieu, F., Jung, R., & Chrispeels, M. J. (2000). Plasma membrane intrinsic proteins from maize cluster in two sequence subgroups with differential aquaporin activity. Plant Physiology, 122(4), 1025–1034.
[31] Bassil, E., Tajima, H., Liang, Y. C., Ohto, M. A., Ushijima, K., Nakano, R., & Blumwald, E. (2011). The Arabidopsis Na+/H+ antiporters NHX1 and NHX2 control vacuolar pH and K+ homeostasis to regulate growth, flower development, and reproduction. The Plant Cell, 23(9), 3482–3497.
[32] Delauney, A. J., & Verma, D. P. S. (1993). Proline biosynthesis and osmoregulation in plants. The plant journal, 4(2), 215–223.
[33] Turgeon, R., & Wolf, S. (2009). Phloem transport: cellular pathways and molecular trafficking. Annual review of plant biology, 60(1), 207–221.
[34] Von Caemmerer, S., & Baker, N. (2007). The biology of transpiration. From guard cells to globe. Plant Physiology, 143(1), 3–3.
[35] Dawson, C., Vincent, J. F., & Rocca, A. M. (1997). How pine cones open. Nature, 390(6661), 668–668.
[36] Quan, H., Pirosa, A., Yang, W., Ritchie, R. O., & Meyers, M. A. (2021). Hydration-induced reversible deformation of the pine cone. Acta biomaterialia, 128, 370–383
[37] Rüggeberg, M., Burgert, I., & Speck, T. (2010). Structural and mechanical design of tissue interfaces in the giant reed Arundo donax. Journal of the Royal Society Interface, 7(44), 499–506.
[38] Evangelista, D., Hotton, S., & Dumais, J. (2011). The mechanics of explosive dispersal and self-burial in the seeds of the filaree, *Erodium cicutarium* (Geraniaceae). Journal of Experimental Biology, 214(4), 521–529.

[39] Jung, W., Kim, W., & Kim, H. Y. (2014). Self-burial mechanics of hygroscopically responsive awns.
[40] Abraham, Y., & Elbaum, R. (2013). Hygroscopic movements in Geraniaceae: the structural variations that are responsible for coiling or bending. New Phytologist, 199(2), 584–594.
[41] Abraham, Y., Tamburu, C., Klein, E., Dunlop, J. W., Fratzl, P., Raviv, U., & Elbaum, R. (2012). Tilted cellulose arrangement as a novel mechanism for hygroscopic coiling in the stork's bill awn. Journal of the Royal Society Interface, 9(69), 640–647.
[42] Gibsen, L. J. (2012). The hierarchical structure and mechanics of plant materials. JR Soc. Interface, 9, 2749–2766.
[43] Leroux, O. (2012). Collenchyma: a versatile mechanical tissue with dynamic cell walls. Annals of Botany, 110(6), 1083–1098.
[44] Kouhen, M., Dimitrova, A., Scippa, G. S., & Trupiano, D. (2023). The course of mechanical stress: types, perception, and plant response. Biology, 12(2), 217.
[45] Thompson, D. S., & Islam, A. (2021). Plant cell wall hydration and plant physiology: An exploration of the consequences of direct effects of water deficit on the plant cell wall. Plants, 10(7), 1263.
[46] Sarkar, D., Bu, L., Jakes, J. E., Zieba, J. K., Kaufman, I. D., Crowley, M. F., ... & Vermaas, J. V. (2023). Diffusion in intact secondary cell wall models of plants at different equilibrium moisture content. The Cell Surface, 9, 100105.
[47] Isnard, S., Speck, T., & Rowe, N. P. (2003). Mechanical architecture and development in Clematis: implications for canalised evolution of growth forms. New Phytologist, 158(3), 543–559.
[48] Ievinsh, G. (2023). Water content of plant tissues: So simple that almost forgotten?. Plants, 12(6), 1238.
[49] McElrone, A. J., Choat, B., Gambetta, G. A., & Brodersen, C. R. (2013). Water uptake and transport in vascular plants. Nature Education Knowledge, 4(5), 6.
[50] Bel, A. V. (1993). Strategies of phloem loading.
[51] Bowker, B. (2017). Developments in our understanding of water-holding capacity. In Poultry quality evaluation (pp. 77–113). Woodhead Publishing.
[52] Kanahama, T., Tsugawa, S., & Sato, M. (2023). Rigidity control mechanism by turgor pressure in plants. Scientific Reports, 13(1), 2063.
[53] Scoffoni, C., Vuong, C., Diep, S., Cochard, H., & Sack, L. (2014). Leaf shrinkage with dehydration: coordination with hydraulic vulnerability and drought tolerance. Plant Physiology, 164(4), 1772–1788.
[54] Kerch, G. (2020). Role of changes in state of bound water and tissue stiffness in development of age-related diseases. Polymers, 12(6), 1362.
[55] Berry, S. L., & Roderick, M. L. (2005). Plant–water relations and the fibre saturation point. New Phytologist, 168(1), 25–37.
[56] Watson, J. L., Seinkmane, E., Styles, C. T., Mihut, A., Krüger, L. K., McNally, K. E., & Derivery, E. (2023). Macromolecular condensation buffers intracellular water potential. Nature, 623(7988), 842–852.
[57] Mo, X., He, L., Liu, Y., Wang, D., Zhao, B., & Chen, J. (2022). The genetic control of the compound leaf patterning in Medicago truncatula. Frontiers in Plant Science, 12, 749989.
[58] Volkov, A. G., Foster, J. C., Baker, K. D., & Markin, V. S. (2010). Mechanical and electrical anisotropy in Mimosa pudica pulvini. Plant signaling & behavior, 5(10), 1211–1221.

[59] Zhang, S. B., Wen, G. J., Qu, Y. Y., Yang, L. Y., & Song, Y. (2022). Trade-offs between xylem hydraulic efficiency and mechanical strength in Chinese evergreen and deciduous savanna species. Tree Physiology, 42(7), 1337–1349.
[60] Knoblauch, M., & Peters, W. S. (2017). What actually is the Münch hypothesis? A short history of assimilate transport by mass flow. Journal of Integrative Plant Biology, 59(5), 292–310.
[61] dos Santos, L. M., Amaral, E. A., Nieri, E. M., Costa, E. V. S., Trugilho, P. F., Calegário, N., & Hein, P. R. G. (2021). Estimating wood moisture by near infrared spectroscopy: Testing acquisition methods and wood surfaces qualities. Wood Material Science & Engineering, 16(5), 336–343.
[62] Kang, W., & Chung, W. Y. (2009). Liquid water diffusivity of wood from the capillary pressure-moisture relation. Journal of wood science, 55, 91–99.
[63] Goyeneche, M., Lasseux, D., & Bruneau, D. (2002). A film-flow model to describe free water transport during drying of a hygroscopic capillary porous medium. Transport in porous media, 48(2), 125–158.
[64] Autengruber, M., Lukacevic, M., & Füssl, J. (2020). Finite-element-based moisture transport model for wood including free water above the fiber saturation point. International Journal of Heat and Mass Transfer, 161, 120228.
[65] Zakaria, Z., Mansor, M. S. B., Rahim, R. A., Balkhis, I., Rahiman, M. H. F., Rahim, H. A., & Yaacob, S. (2013). Magnetic induction tomography: A review on the potential application in agricultural industry of Malaysia. J. Agric. Sci, 5(9), 78.
[66] Capitani, D., Di Tullio, V., & Proietti, N. (2012). Nuclear magnetic resonance to characterize and monitor cultural heritage. Progress in Nuclear Magnetic Resonance Spectroscopy, 64, 29–69.
[67] Koptyug, I. V. (2012). MRI of mass transport in porous media: Drying and sorption processes. Progress in Nuclear Magnetic Resonance Spectroscopy, 65, 1–65.
[68] Sedighi-Gilani, M., Griffa, M., Mannes, D., Lehmann, E., Carmeliet, J., & Derome, D. (2012). Visualization and quantification of liquid water transport in softwood by means of neutron radiography. International Journal of Heat and Mass Transfer, 55(21–22), 6211–6221.
[69] Gilani, M. S., Abbasion, S., Lehmann, E., Carmeliet, J., & Derome, D. (2014). Neutron imaging of moisture displacement due to steep temperature gradients in hardwood. International journal of thermal sciences, 81, 1–12.
[70] Couceiro, J., Lindgren, O., Hansson, L., Söderström, O., & Sandberg, D. (2019). Real-time wood moisture-content determination using dual-energy X-ray computed tomography scanning. Wood Material Science & Engineering, 14(6), 437–444.
[71] Ge, Z., Chen, L., Luo, R., Wang, Y., & Zhou, Y. (2018). The detection of structure in wood by X-ray CT imaging technique. BioResources, 13(2), 3674–3685.
[72] Lindgren, O., Seifert, T., & Du Plessis, A. (2016). Moisture content measurements in wood using dual-energy CT scanning–a feasibility study. Wood Material Science & Engineering, 11(5), 312–317.
[73] Saarela, J. M. S., Heikkinen, S. M., Fabritius, T. E. J., Haapala, A. T., & Myllylä, R. A. (2008). Refractive index matching improves optical object detection in paper. Measurement Science and Technology, 19(5), 055710.
[74] Forughi, A. F., Green, S. I., & Stoeber, B. (2016). Optical transparency of paper as a function of moisture content with applications to moisture measurement. Review of Scientific Instruments, 87(2).

[75] Brodribb, T. J., Carriqui, M., Delzon, S., & Lucani, C. (2017). Optical measurement of stem xylem vulnerability. Plant Physiology, 174(4), 2054–2061.
[76] Fabritius, T., & Myllylä, R. (2006). Liquid sorption investigation of porous media by optical coherence tomography. Journal of Physics D: Applied Physics, 39(21), 4668.
[77] Karppinen, T., Kassamakov, I., Hæggström, E., & Stor-Pellinen, J. (2004). Measuring paper wetting processes with laser transmission. Measurement Science and Technology, 15(7), 1223.
[78] Leblon, B., Adedipe, O., Hans, G., Haddadi, A., Tsuchikawa, S., Burger, J., & LaRocque, A. (2013). A review of near-infrared spectroscopy for monitoring moisture content and density of solid wood. The forestry chronicle, 89(5), 595–606.
[79] Pettorelli, N. (2013). The normalized difference vegetation index. Oxford University Press, USA.
[80] Adamatzky, A. (2019). A brief history of liquid computers. Philosophical Transactions of the Royal Society B, 374(1774), 20180372.
[81] Chen, S., Wang, H. Z., Liu, T. Y., & Liu, J. (2023). Liquid metal smart materials toward soft robotics. Advanced Intelligent Systems, 5(8), 2200375.
[82] Feng, W., He, Q., & Zhang, L. (2025). Embedded physical intelligence in liquid crystalline polymer actuators and robots. Advanced Materials, 37(2), 2312313.
[83] Chiolerio, A., & Quadrelli, M. B. (2017). Smart fluid systems: the advent of autonomous liquid robotics. Advanced Science, 4(7), 1700036.
[84] Dong, Y. Z., Seo, Y., & Choi, H. J. (2019). Recent development of electro-responsive smart electrorheological fluids. Soft Matter, 15(17), 3473–3486.
[85] Chen, G., Ma, B., Chen, Y., Chen, Y., Zhang, J., & Liu, H. (2024). Soft robots with plant-inspired gravitropism based on fluidic liquid metal. Advanced Science, 11(18), 2306129.
[86] Li, M., Pal, A., Aghakhani, A., Pena-Francesch, A., & Sitti, M. (2022). Soft actuators for real-world applications. Nature Reviews Materials, 7(3), 235–249.
[87] Sinibaldi, E., Argiolas, A., Puleo, G. L., & Mazzolai, B. (2014). Another lesson from plants: the forward osmosis-based actuator. PloS one, 9(7), e102461.
[88] Must, I., Sinibaldi, E., & Mazzolai, B. (2019). A variable stiffness tendril like soft robot based on reversible osmotic actuation. Nature Communications, 10(1), 344.
[89] Marchese, A. D., Onal, C. D., & Rus, D. (2014). Autonomous soft robotic fish capable of escape maneuvers using fluidic elastomer actuators. Soft robotics, 1(1), 75–87.
[90] Katzschmann, R. K., Marchese, A. D., & Rus, D. (2015). Hydraulic autonomous soft robotic fish for 3D swimming. In Experimental Robotics: The 14th International Symposium on Experimental Robotics (pp. 405–420). Cham: Springer International Publishing.
[91] Acome, E., Mitchell, S. K., Morrissey, T. G., Emmett, M. B., Benjamin, C., King, M., & Keplinger, C. (2018). Hydraulically amplified self-healing electrostatic actuators with muscle-like performance. Science, 359(6371), 61–65.
[92] Christianson, C., Cui, Y., Ishida, M., Bi, X., Zhu, Q., Pawlak, G., & Tolley, M. T. (2020). Cephalopod-inspired robot capable of cyclic jet propulsion through shape change. Bioinspiration & biomimetics, 16(1), 016014.
[93] Marut, K., Stewart, C., Michael, T., Villanueva, A., & Priya, S. (2013). A jellyfish-inspired jet propulsion robot actuated by an iris mechanism. Smart materials and structures, 22(9), 094021.

[94] Cecchini, L., Mariani, S., Ronzan, M., Mondini, A., Pugno, N. M., & Mazzolai, B. (2023). 4D printing of humidity-driven seed inspired soft robots. Advanced Science, 10(9), 2205146.
[95] Eyegheleme, N. L., Shi, W., De Koninck, L. H., O'Brien, J. L., & Boreyko, J. B. (2021). Synthetic trees for enhanced solar evaporation and water harvesting. Applied Physics Letters, 118(25)
[96] Wei, S., & Ghosh, T. K. (2024). Moisture-Driven Cellulose Actuators with Directional Motion and Programmable Shapes. Advanced Intelligent Systems, 6(5), 2300638.
[97] Choi, M., Shin, B., & Kim, H. Y. (2023). Hygromachines: Humidity-powered wheels, seesaws, and vehicles. Soft Robotics, 10(6), 1171–1180.
[98] Sadeghi, A., Mondini, A., & Mazzolai, B. (2017). Toward self-growing soft robots inspired by plant roots and based on additive manufacturing technologies. Soft robotics, 4(3), 211–223.
[99] Kataruka, A., & Hutchens, S. B. (2021). Swelling of a non-vascular-plant-inspired soft composite. Matter, 4(12), 3991–4005.
[100] Na, H., Kang, Y. W., Park, C. S., Jung, S., Kim, H. Y., & Sun, J. Y. (2022). Hydrogel-based strong and fast actuators by electroosmotic turgor pressure. Science, 376(6590), 301–307.
[101] Wang, Y., Lee, J., Werber, J. R., & Elimelech, M. (2020). Capillary-driven desalination in a synthetic mangrove. Science advances, 6(8), eaax5253.
[102] Mei, T., Zhang, H., & Xiao, K. (2022). Bioinspired artificial ion pumps. ACS nano, 16(9), 13323–13338.
[103] Yun, T. G., Bae, J., Rothschild, A., & Kim, I. D. (2019). Transpiration driven electrokinetic power generator. ACS nano, 13(11), 12703–12709.
[104] Zhang, S., Wei, X., Cao, X., Peng, M., Wang, M., Jiang, L., & Jin, J. (2024). Solar-driven membrane separation for direct lithium extraction from artificial salt-lake brine. Nature Communications, 15(1), 238.
[105] Wang, R., & Lin, S. (2024). Membrane design principles for ion-selective electrodialysis: an analysis for Li/Mg separation. Environmental Science & Technology, 58(7), 3552–3563.
[106] Dradrach, K., Zmyślony, M., Deng, Z., Priimagi, A., Biggins, J., & Wasylczyk, P. (2023). Light-driven peristaltic pumping by an actuating splay-bend strip. Nature Communications, 14(1), 1877.
[107] Wang, X., Cheng, C., Wang, S., & Liu, S. (2009). Electroosmotic pumps and their applications in microfluidic systems. Microfluidics and nanofluidics, 6, 145–162.
[108] Mazzolai, B., Tramacere, F., Fiorello, I., & Margheri, L. (2020). The bio-engineering approach for plant investigations and growing robots. A mini-review. Frontiers in Robotics and AI, 7, 573014.
[109] Kim, K., Kim, H., Lim, J. H., & Lee, S. J. (2016). Development of a desalination membrane bioinspired by mangrove roots for spontaneous filtration of sodium ions. ACS nano, 10(12), 11428–11433.
[110] Xiao, K., Chen, L., Chen, R., Heil, T., Lemus, S. D. C., Fan, F., & Antonietti, M. (2019). Artificial light-driven ion pump for photoelectric energy conversion. Nature communications, 10(1), 74.
[111] Reid, L., & Hamad, W. Y. (2021). Electro-osmotic actuators from cellulose nanocrystals and nanocomposite hydrogels. ACS Applied Polymer Materials, 4(1), 598–606.

[112] Ko, J., Kim, D., Song, Y., Lee, S., Kwon, M., Han, S., & Cho, J. (2020). Electro-osmosis-driven hydrogel actuators using hydrophobic/hydrophilic layer-by-layer assembly-induced crack electrodes. ACS nano, 14(9), 11906–11918.
[113] Scorza, L. C. T., & Dornelas, M. C. (2011). Plants on the move: towards common mechanisms governing mechanically-induced plant movements. Plant signaling & behavior, 6(12), 1979–1986.
[114] Gere, J. M., & Goodno, B. J. (2001). Mechanics of Materials 5th. Brooks Cole, 780.
[115] Saunier, J., Alloin, F., Sanchez, J. Y., & Barriere, B. (2004). Plasticized micro-porous poly (vinylidene fluoride) separators for lithium-ion batteries. I. Swelling behavior of dense membranes with respect to a liquid electrolyte—Characterization of the swelling equilibrium. Journal of Polymer Science Part B: Polymer Physics, 42(3), 532–543.
[116] Shimizu, H., Arioka, Y., Ogawa, M., Wada, R., & Okabe, M. (2011). Sol-gel transitions of poly (vinylidene fluoride) in organic solvents containing LiBF4. Polymer journal, 43(6), 540–544.
[117] Uduste, I., Kaasik, F., Johanson, U., Aabloo, A., & Must, I. (2020). An all-textile non-muscular biomimetic actuator based on electrohydrodynamic swelling. Frontiers in Bioengineering and Biotechnology, 8, 408.
[118] Zeng, S., Chen, C. H., Mikkelsen Jr, J. C., & Santiago, J. G. (2001). Fabrication and characterization of electroosmotic micropumps. Sensors and Actuators B: Chemical, 79(2–3), 107–114.
[119] Otero-Mato, J. M., Lesch, V., Montes-Campos, H., Smiatek, J., Diddens, D., Cabeza, O., & Varela, L. M. (2019). Solvation in ionic liquid-water mixtures: A computational study. Journal of Molecular Liquids, 292, 111273.
[120] Delgado, P. A., Brutman, J. P., Masica, K., Molde, J., Wood, B., & Hillmyer, M. A. (2016). High surface area carbon black (BP-2000) as a reinforcing agent for poly [(−)-lactide]. Journal of Applied Polymer Science, 133(45).
[121] Pabst, O., Martinsen, Ø. G., & Chua, L. (2019). Information can be stored in the human skin memristor which has non-volatile memory. Scientific reports, 9(1), 19260.
[122] Chen, H., Montanari, C., Yan, M., Popov, S., Li, Y., Sychugov, I., & Berglund, L. A. (2020). Refractive index of delignified wood for transparent biocomposites. RSC advances, 10(67), 40719–40724.
[123] Wang, Z., Sun, G., Lewis, N. H., Mandal, M., Sharma, A., Kim, M., & de Pablo, J. J. (2025). Water-mediated ion transport in an anion exchange membrane. Nature Communications, 16(1), 1099
[124] Frioui, N., Bezazi, A., Remillat, C., Scarpa, F., & Gomez, J. P. (2010). Viscoelastic and compression fatigue properties of closed cell PVDF foam. Mechanics of materials, 42(2), 189–195.
[125] Kandil, H., & El Desouky, F. G. (2025). Plasticizer modulation of dynamic mechanical properties and dielectric performance in sodium alginate-based biopolymer films. Journal of Inorganic and Organometallic Polymers and Materials, 1–15.
[126] Zhang, C., Chen, M., Keten, S., Coasne, B., Derome, D., & Carmeliet, J. (2021). Hygromechanical mechanisms of wood cell wall revealed by molecular modeling and mixture rule analysis. Science Advances, 7(37), eabi8919.

[127] Kulasinski, K., Guyer, R., Keten, S., Derome, D., & Carmeliet, J. (2015). Impact of moisture adsorption on structure and physical properties of amorphous biopolymers. Macromolecules, 48(8), 2793–2800.
[128] Henriksson, M., Berglund, L. A., Isaksson, P., Lindström, T., & Nishino, T. (2008). Cellulose nanopaper structures of high toughness. Biomacromolecules, 9(6), 1579–1585.
[129] Merindol, R., Diabang, S., Mujica, R., Le Houerou, V., Roland, T., Gauthier, C., ... & Felix, O. (2020). Assembly of anisotropic nanocellulose films stronger than the original tree. ACS nano, 14(12), 16525–16534.
[130] Jiang, G. (2018). Gas wettability of reservoir rock surfaces with porous media. Gulf Professional Publishing.
[131] Hesse, L., Bunk, K., Leupold, J., Speck, T., & Masselter, T. (2019). Structural and functional imaging of large and opaque plant specimens. Journal of experimental botany, 70(14), 3659–3678.
[132] Geer, R., Iannucci, S., & Li, S. (2020). Pneumatic coiling actuator inspired by the awns of erodium cicutarium. Frontiers in Robotics and AI, 7, 17.
[133] Mancuso, S., Mazzolai, B., Comparini, D., Popova, L., Azzarello, E., & Masi, E. (2014). Subsurface investigation and interaction by self-burying biooinspired probes. Pontedera, Italy: European Space Agency, the Advanced Concepts Team. Ariadna Final Report, 12–6402.
[134] He, J., & Toi, Y. (2013). Improved constitutive modeling for phase transformation of shape memory alloys. Journal of Solid Mechanics and Materials Engineering, 7(1), 11–26.
[135] Guan, J. H., Pei, Y. C., & Wu, J. T. (2021). A driving strategy of shape memory alloy wires with electric resistance modeled by a logistic function for power consumption reduction. Mechanical Systems and Signal Processing, 160, 107839.
[136] Mahali, S. M., Setapa, A., & Zolkamal, N. N. (2018). Mathematical model for drug release from a logistically swelling hydrogel. In AIP Conference Proceedings (Vol. 1974, No. 1). AIP Publishing.
[137] Cai, J., Jin, T., Kou, J., Zou, S., Xiao, J., & Meng, Q. (2021). Lucas–Washburn equation-based modeling of capillary-driven flow in porous systems. Langmuir, 37(5), 1623–1636.
[138] Jiang, A., Xynogalas, G., Dasgupta, P., Althoefer, K., & Nanayakkara, T. (2012). Design of a variable stiffness flexible manipulator with composite granular jamming and membrane coupling. In 2012 IEEE/RSJ International Conference on Intelligent Robots and Systems (pp. 2922–2927). IEEE.
[139] Fitzgerald, S. G., Delaney, G. W., & Howard, D. (2020). A review of jamming actuation in soft robotics. In Actuators (Vol. 9, No. 4, p. 104). MDPI.
[140] Mattmann, M., De Marco, C., Briatico, F., Tagliabue, S., Colusso, A., Chen, X. Z., & Nelson, B. (2022). Thermoset shape memory polymer variable stiffness 4D robotic catheters. Advanced Science, 9(1), 2103277.
[141] Vicente, J., Costa, P., Lanceros-Mendez, S., Abete, J. M., & Iturrospe, A. (2019). Electromechanical properties of PVDF-based polymers reinforced with nanocarbonaceous fillers for pressure sensing applications. Materials, 12(21), 3545.
[142] Etale, A., Onyianta, A. J., Turner, S. R., & Eichhorn, S. J. (2023). Cellulose: a review of water interactions, applications in composites, and water treatment. Chemical reviews, 123(5), 2016–2048.
[143] Schoen, M., & Günther, G. (2010). Phase transitions in nanoconfined fluids: Synergistic coupling between soft and hard matter. Soft Matter, 6(23), 5832–5838.

[144] O'Neill, H., Pingali, S. V., Petridis, L., He, J., Mamontov, E., Hong, L., & Davison, B. H. (2017). Dynamics of water bound to crystalline cellulose. Scientific reports, 7(1), 11840.
[145] Reyssat, E., & Mahadevan, L. (2009). Hygromorphs: from pine cones to biomimetic bilayers. Journal of the Royal Society Interface, 6(39), 951–957.
[146] Ha, J., Choi, S. M., Shin, B., Lee, M., Jung, W., & Kim, H. Y. (2020). Hygroresponsive coiling of seed awns and soft actuators. Extreme Mechanics Letters, 38, 100746.
[147] Renda, F., Serchi, F. G., Boyer, F., & Laschi, C. (2015). Structural dynamics of a pulsed-jet propulsion system for underwater soft robots. International Journal of Advanced Robotic Systems, 12(6), 68.
[148] Giorgio Serchi, F., Lidtke, A. K., & Weymouth, G. D. (2018). A soft aquatic actuator for unsteady peak power amplification. IEEE/ASME Transactions on Mechatronics, 23(6), 2968–2973.

# ACKNOWLEDGEMENTS

I would like to sincerely thank my supervisors, Assoc. Prof. Indrek Must and Prof. Alvo Aabloo, for their steady support, trust, and valuable guidance that helped me reach this important milestone on the challenging path of academia.

I am very grateful for the warm and friendly atmosphere in the IMS Lab. I especially appreciate the countless inspiring conversations that I shared with Urmas Johanson, Tarmo Tamm, Ingrid Rebane, Veiko Vunder, Heiki Kasemägi, Hans Priks, Anna-Liisa Peikolainen, Karl Kruusamäe, Karl Jakob Levin, Siim Koor, Oleksandr Syzoniuk, Kadri-Ann Pankratov, and Leonid Zinatullin.

My heartfelt thanks also go to Andres Punning, Hannes Kollist, and Egon Meigas, whose encouragement has been an important part of my growth as a young researcher.

Finally, I am profoundly thankful for the unwavering support of my mother, Ina, my grandmother, Josephine, my best friend, Amedeo Pagliotto, and my Estonian Language teacher, Aleksandr Petrov, whose encouragement has sustained me throughout this demanding journey toward the doctoral degree.

This work was financially supported by the Estonian Research Council grants PRG1498 and PRG1084.

# PUBLICATIONS

# CURRICULUM VITAE


| | |
|---|---|
| Name: | Yauheni Sarokin |
| Date of birth: | 03.03.1994 |
| Phone | +372 57131327 |
| E-mail: | yauheni@ut.ee |


**Education:**

| | |
|---|---|
| 2020 onwards | University of Tartu, Faculty of Science and Technology, doctoral studies in Engineering and Technology |
| 2016–2019 | University of Trento, Department of Industrial Engineering, MSc in Material Science |
| 2011–2016 | Belarusian National Technical University, Faculty of Energy Construction, BSc in Civil Engineering |

**Employment:**

| | |
|---|---|
| 2025 onwards | Plantinvent OÜ, Engineer |
| 2020–2025 | University of Tartu, Junior Research Fellow in Materials Technology |

**Teaching:**

| | |
|---|---|
| 2025 | Tutoring of one bachelor student to completion |
| 2022–2024 | Instructor in the course ‘Data Acquisition and signal processing’, University of Tartu |

# ELULOOKIRJELDUS


| | |
|---|---|
| Nimi: | Yauheni Sarokin |
| Sünniaeg: | 03.03.1994 |
| Telefon | +372 57131327 |
| E-mail: | yauheni@ut.ee |


**Haridustee:**

| | |
|---|---|
| alates 2020 | Tartu Ülikool, Loodus- ja Tehnoloogiateaduskond, doktoriõpe erialal ‘Tehnika ja tehnoloogia’ |
| 2016–2019 | Trento Ülikool, Department of Industrial Engineering, materjaliteaduse magistrantuuriõpe |
| 2011–2016 | Valgevene Riiklik Tehnikaülikool, Ehitusinseneri osakond, ehitusinseneri bakalaureuseõpe |

**Teenistuskäik:**

| | |
|---|---|
| alates 2025 | Plantinvent OÜ, insener |
| 2020–2025 | Tartu Ülikool, materjalitehnoloogia nooremteadur |

**Õppetöö läbiviimine:**

| | |
|---|---|
| 2025 | Juhendaja ühele bakalaureusetööle |
| 2022–2024 | Juhendaja õppeaines ‘Data Acquisition and Signal Processing’, Tartu Ülikool |

# DISSERTATIONES TECHNOLOGIAE UNIVERSITATIS TARTUENSIS

1. **Imre Mäger**. Characterization of cell-penetrating peptides: Assessment of cellular internalization kinetics, mechanisms and bioactivity. Tartu 2011, 132 p.
2. **Taavi Lehto**. Delivery of nucleic acids by cell-penetrating peptides: application in modulation of gene expression. Tartu 2011, 155 p.
3. **Hannes Luidalepp**. Studies on the antibiotic susceptibility of *Escherichia coli*. Tartu 2012, 111 p.
4. **Vahur Zadin**. Modelling the 3D-microbattery. Tartu 2012, 149 p.
5. **Janno Torop**. Carbide-derived carbon-based electromechanical actuators. Tartu 2012, 113 p.
6. **Julia Suhorutšenko**. Cell-penetrating peptides: cytotoxicity, immunogenicity and application for tumor targeting. Tartu 2012, 139 p.
7. **Viktoryia Shyp**. G nucleotide regulation of translational GTPases and the stringent response factor RelA. Tartu 2012, 105 p.
8. **Mardo Kõivomägi**. Studies on the substrate specificity and multisite phosphorylation mechanisms of cyclin-dependent kinase Cdk1 in *Saccharomyces cerevisiae*. Tartu, 2013, 157 p.
9. **Liis Karo-Astover**. Studies on the Semliki Forest virus replicase protein nsP1. Tartu, 2013, 113 p.
10. **Piret Arukuusk**. NickFects–novel cell-penetrating peptides. Design and uptake mechanism. Tartu, 2013, 124 p.
11. **Piret Villo**. Synthesis of acetogenin analogues. Asymmetric transfer hydrogenation coupled with dynamic kinetic resolution of α-amido-β-keto esters. Tartu, 2013, 151 p.
12. **Villu Kasari**. Bacterial toxin-antitoxin systems: transcriptional cross-activation and characterization of a novel *mqsRA* system. Tartu, 2013, 108 p.
13. **Margus Varjak**. Functional analysis of viral and host components of alphavirus replicase complexes. Tartu, 2013, 151 p.
14. **Liane Viru**. Development and analysis of novel alphavirus-based multifunctional gene therapy and expression systems. Tartu, 2013, 113 p.
15. **Kent Langel**. Cell-penetrating peptide mechanism studies: from peptides to cargo delivery. Tartu, 2014, 115 p.
16. **Rauno Temmer**. Electrochemistry and novel applications of chemically synthesized conductive polymer electrodes. Tartu, 2014, 206 p.
17. **Indrek Must**. Ionic and capacitive electroactive laminates with carbonaceous electrodes as sensors and energy harvesters. Tartu, 2014, 133 p.
18. **Veiko Voolaid**. Aquatic environment: primary reservoir, link, or sink of antibiotic resistance? Tartu, 2014, 79 p.
19. **Kristiina Laanemets**. The role of SLAC1 anion channel and its upstream regulators in stomatal opening and closure of *Arabidopsis thaliana.* Tartu, 2015, 115 p.

20. **Kalle Pärn**. Studies on inducible alphavirus-based antitumour strategy mediated by site-specific delivery with activatable cell-penetrating peptides. Tartu, 2015, 139 p.
21. **Anastasia Selyutina**. When biologist meets chemist: a search for HIV-1 inhibitors. Tartu, 2015, 172 p.
22. **Sirle Saul**. Towards understanding the neurovirulence of Semliki Forest virus. Tartu, 2015, 136 p.
23. **Marit Orav**. Study of the initial amplification of the human papillomavirus genome. Tartu, 2015, 132 p.
24. **Tormi Reinson**. Studies on the Genome Replication of Human Papillomaviruses. Tartu, 2016, 110 p.
25. **Mart Ustav Jr**. Molecular Studies of HPV-18 Genome Segregation and Stable Replication. Tartu, 2016, 152 p.
26. **Margit Mutso**. Different Approaches to Counteracting Hepatitis C Virus and Chikungunya Virus Infections. Tartu, 2016, 184 p.
27. **Jelizaveta Geimanen**. Study of the Papillomavirus Genome Replication and Segregation. Tartu, 2016, 168 p.
28. **Mart Toots**. Novel Means to Target Human Papillomavirus Infection. Tartu, 2016, 173 p.
29. **Kadi-Liis Veiman**. Development of cell-penetrating peptides for gene delivery: from transfection in cell cultures to induction of gene expression *in vivo*. Tartu, 2016, 136 p.
30. **Ly Pärnaste**. How, why, what and where: Mechanisms behind CPP/cargo nanocomplexes. Tartu, 2016, 147 p.
31. **Age Utt**. Role of alphavirus replicase in viral RNA synthesis, virus-induced cytotoxicity and recognition of viral infections in host cells. Tartu, 2016, 183 p.
32. **Veiko Vunder**. Modeling and characterization of back-relaxation of ionic electroactive polymer actuators. Tartu, 2016, 154 p.
33. **Piia Kivipõld**. Studies on the Role of Papillomavirus E2 Proteins in Virus DNA Replication. Tartu, 2016, 118 p.
34. **Liina Jakobson**. The roles of abscisic acid, $CO_2$, and the cuticle in the regulation of plant transpiration. Tartu, 2017, 162 p.
35. **Helen Isok-Paas**. Viral-host interactions in the life cycle of human papillomaviruses. Tartu, 2017, 158 p.
36. **Hanna Hõrak**. Identification of key regulators of stomatal $CO_2$ signalling via $O_3$-sensitivity. Tartu, 2017, 260 p.
37. **Jekaterina Jevtuševskaja**. Application of isothermal amplification methods for detection of *Chlamydia trachomatis* directly from biological samples. Tartu, 2017, 96 p.
38. **Ülar Allas**. Ribosome-targeting antibiotics and mechanisms of antibiotic resistance. Tartu, 2017, 152 p.
39. **Anton Paier**. Ribosome Degradation in Living Bacteria. Tartu, 2017, 108 p.
40. **Vallo Varik**. Stringent Response in Bacterial Growth and Survival. Tartu, 2017, 101 p.

41. **Pavel Kudrin**. In search for the inhibitors of *Escherichia coli* stringent response factor RelA. Tartu, 2017, 138 p.
42. **Liisi Henno**. Study of the human papillomavirus genome replication and oligomer generation. Tartu, 2017, 144 p.
43. **Katrin Krõlov**. Nucleic acid amplification from crude clinical samples exemplified by *Chlamydia trachomatis* detection in urine. Tartu, 2018, 118 p.
44. **Eve Sankovski**. Studies on papillomavirus transcription and regulatory protein E2. Tartu, 2018, 113 p.
45. **Morteza Daneshmand**. Realistic 3D Virtual Fitting Room. Tartu, 2018, 233 p.
46. **Fatemeh Noroozi**. Multimodal Emotion Recognition Based Human-Robot Interaction Enhancement. Tartu, 2018, 113 p.
47. **Krista Freimann**. Design of peptide-based vector for nucleic acid delivery in vivo. Tartu, 2018, 103 p.
48. **Rainis Venta**. Studies on signal processing by multisite phosphorylation pathways of the *S. cerevisiae* cyclin-dependent kinase inhibitor Sic1. Tartu, 2018, 155 p.
49. **Inga Põldsalu**. Soft actuators with ink-jet printed electrodes. Tartu, 2018, 85 p.
50. **Kadri Künnapuu**. Modification of the cell-penetrating peptide PepFect14 for targeted tumor gene delivery and reduced toxicity. Tartu, 2018, 114 p.
51. **Toomas Mets**. RNA fragmentation by MazF and MqsR toxins of *Escherichia coli.* Tartu, 2019, 119 p.
52. **Kadri Tõldsepp**. The role of mitogen-activated protein kinases MPK4 and MPK12 in $CO_2$-induced stomatal movements. Tartu, 2019, 259 p.
53. **Pirko Jalakas**. Unravelling signalling pathways contributing to stomatal conductance and responsiveness. Tartu, 2019, 120 p.
54. **S. Sunjai Nakshatharan**. Electromechanical modelling and control of ionic electroactive polymer actuators. Tartu, 2019, 165 p.
55. **Eva-Maria Tombak**. Molecular studies of the initial amplification of the oncogenic human papillomavirus and closely related nonhuman primate papillomavirus genomes. Tartu, 2019, 150 p.
56. **Meeri Visnapuu**. Design and physico-chemical characterization of metal-containing nanoparticles for antimicrobial coatings. Tartu, 2019, 138 p.
57. **Jelena Beljantseva**. Small fine-tuners of the bacterial stringent response – a glimpse into the working principles of Small Alarmone Synthetases. Tartu, 2020, 104 p.
58. **Egon Urgard**. Potential therapeutic approaches for modulation of inflammatory response pathways. Tartu, 2020, 120 p.
59. **Sofia Raquel Alves Oliveira**. HPLC analysis of bacterial alarmone nucleotide (p)ppGpp and its toxic analogue ppApp. Tartu, 2020, 122 p.
60. **Mihkel Örd**. Ordering the phosphorylation of cyclin-dependent kinase Cdk1 substrates in the cell cycle. Tartu, 2021, 228 p.
61. **Fred Elhi**. Biocompatible ionic electromechanically active polymer actuator based on biopolymers and non-toxic ionic liquids. Tartu, 2021, 140 p.

62. **Liisi Talas**. Reconstructing paleo-diversity, dynamics and response of eukaryotes to environmental change over the Late-Glacial and Holocene period in lake Lielais Svētiņu using sedaDNA. Tartu, 2021, 118 p.
63. **Livia Matt**. Novel isosorbide-based polymers. Tartu, 2021, 118 p.
64. **Koit Aasumets**. The dynamics of human mitochondrial nucleoids within the mitochondrial network. Tartu, 2021, 104 p.
65. **Faiza Summer**. Development and optimization of flow electrode capacitor technology. Tartu, 2022, 109 p.
66. **Olavi Reinsalu**. Cancer-testis antigen MAGE-A4 is incorporated into extracellular vesiclesand is exposed to the surface. Tartu, 2022, 130 p.
67. **Tetiana Brodiazhenko**. RelA-SpoT Homolog enzymes as effectors of Toxin-Antitoxin systems. Tartu, 2022, 132 p.
68. **Georg-Marten Lanno**. Development of novel antibacterial drug delivery systems as wound scaffolds using electrospinning technology. Tartu, 2022, 175 p.
69. **Liubov Cherkashchenko**. New insights into alphaviral nsP2 functions. Tartu, 2023, 171 p.
70. **Kristina Kiisholts**. Peptide-based drug carriers and preclinical nanomedicine applications for endometriosis treatment. Tartu, 2023, 138 p.
71. **Kai Rausalu**. Alphaviral nsP2 protease: From requirements for functionality to inhibition. Tartu, 2023, 175 p.
72. **Laura Sandra Lello**. Unraveling the intricate nature of the alphavirus RNA replicase. Tartu, 2023, 219 p.
73. **Houman Masnavi**. Visibility Aware Navigation. Tartu, 2023, 180 p.
74. **Kadir Aktas**. Cosmic Ray Tomography based Object Reconstruction and Recognition. Tartu, 2023, 104 p.
75. **Egils Avots**. Brain abnormality detection using statistical analysis of individual structural connectivity networks and EEG signals. Tartu, 2023, 223 p.
76. **Sainan Wang**. Structure-guided insights into the functions of CHIKV nsP2. Tartu, 2024, 154 p.
77. **Anneli Samel**. Unveiling the characteristics of cancer-testis antigen MAGEA10. Tartu, 2024, 136 p.
78. **Ikechukwu Ofodile**. Fault tolerant attitude control for nanosatellites: ESTCube-2 case. Tartu, 2024, 130 p.
79. **Olena Zamora**. Impacts of plant hormones on controlling stomatal conductance. Tartu, 2024, 166 p.
80. **Mariliis Hinnu**. *In vitro* methods for studying the mechanisms of ribosome-targeting antibiotics. Tartu, 2024, 143 p.
81. **Chung-Yueh Yeh**. Characterization of MPK and HT1 kinases in $CO_2$-induced stomatal movements. Tartu, 2024, 118 p.
82. **Iman Dadras**. Low power neural network-based control and actuation solutions for insect-scale robots. Tartu, 2024, 149 p.
83. **Fatemeh Rastgar**. Towards reliable real-time trajectory optimization. Tartu, 2024, 158 p.

84. **Maria Maloverjan**. Optimizing cell-penetrating peptide-based nanoparticles for delivery of nucleic acid therapeutics. Tartu, 2024, 172 p.
85. **Joonas Merisalu**. Resistive switching in memristor structures with multilayer dielectrics. Tartu, 2024, 149 p.
86. **Siim Laanesoo**. Novel high-performance biomass-based polymers. Tartu, 2024, 117 p.
87. **Henri Ingelman**. Systems-level characterisation and improvement of *Clostridium autoethanogenum* metabolism. Tartu, 2024, 164 p.
88. **Mailis Laht**. Using the One Health approach for mapping the spread of antibiotic resistant bacteria in Estonia. Tartu, 2024, 188 p.
89. **Ingrid Rebane**. Structure-property relationships of moldable silicone foams. Tartu, 2024, 164 p.
90. **Robert Valner**. Design of TeMoto, a software framework for dependable, adaptive, and collaborative autonomous robots. Tartu, 2024, 182 p.
91. **Kristiina Kurg**. Exploring the potential of a liquid biopsy approach for melanoma diagnostics and the role of extracellular vesicles in atherosclerosis development. Tartu, 2025, 201 p.
92. **Rauno Sedrik**. Synthesis and investigation of polymers from different cyclic bio-based monomers. Tartu, 2025, 155 p.
93. **Alina Ismagilova**. Safety assessment of novel bio-based polymers and compounds used in low carbon technologies. Tartu, 2025, 156 p.
94. **Baiba Brūmele**. Uncovering the TRMT112 methyltransferase network and characterising the cellular functions of TRMT112-network member N6AMT1. Tartu, 2025, 135 p.
95. **Ingmar Tulva**. Causes and consequences of stomatal density in relation to atmospheric humidity. Tartu, 2025, 142 p.